034643-1-T

Annual Report
ARL Federated Laboratory - Advanced Sensors Project, Fiscal Year 1997

Linda P.B. Katehi
Rob Robertson

1997

34643-1-T = RL-2472

ARL Report

Linda P.B. Katehi and Rob Robertson

Radiation Laboratory, Department of Electrical Engineering and Computer Science
University of Michigan, Ann Arbor, MI 48109-2122

1 Project Objectives

The main objective of this project is to develop three–dimensional time domain techniques to analyze antenna structures. A full-wave analysis of the antenna is performed using the Finite Difference Time Domain (FDTD) and Multiresolution Time–Domain(MRTD) methods. MRTD is a new method, developed in cooperation with ARL, that uses wavelets for the numerical simulation of electromagnetic phenomena. This method has been applied with great success to several different microwave structures. Overall MRTD exhibits one to two orders of magnitude improvement in memory requirements over conventional time–domain methods such as FDTD[1–4]. Preliminary work has been performed on patch antennas, with MRTD showing a factor of 33 memory improvement over conventional FDTD [3].

2 Accomplishments in Fiscal Year 1997

This section will cover four main topics. First, the design and modelling of a slot antenna which is added to an already completed dipole to make a dual–polarized antenna. Second, the generation of a MRTD code to simulate patch antenna goeometries. Third the characterization and modelling of a microstrip-to-CPW transition with FDTD and HFSS. Finally, the generation of FDTD codes to model the dual–polarized antenna briefly mentioned above.

2.1 Dual–Polarized Antenna Design

Lockheed–Sanders commissioned the University of Michigan to design a dual polarized antenna based on a previously completed design [5]. This design uses a CPW fed slot antenna which is printed on the top of the dipole to add an additional polarization perpindicular to that of the dipole. The initial design is shown in Figure 1.

Simulation runs are carried out using Hewlett–Packard's High Frequency Structure Simulator (HFSS). The slot was found to have a very low initial input impedance (on the order of 10 Ω). A stub matching network is used to match the input impedance of the slot antenna. Final S_{11} results are shown in Figure 2. Overall, good performance is observed in matching. The bandwidth is of the match is within design specifications. Additionally, it should be pointed out that any type of slot antenna has a large null centered around 0 degrees, which will limit the performance of the antenna. This null was taken care of by placing vertical ground planes on either side of the substrate. A model based on Figure 1 was constructed and tested for both S–parameters

and antenna patterns. Figure 3 shows an E-plane antenna pattern for the 1 GHz model. As seen in Figure 3, the null at 0 degrees disapears with the addition of vertical ground planes to the antenna.

The final design of the antenna will incorporate the CPW-fed slot antenna shown in Figure 1, with a microstrip-to-CPW transition acting as a matching network, rather than the capacitive stub. This transition is discussed in a later section.

2.2 MRTD Analysis of a Patch Antenna

MRTD is a technique which allows large computational and memory savings over conventional techniques such as FDTD. The Multiresolution Time-Domain (MRTD) scheme with perfectly matched layer (PML) absorbing boundaries is applied to the analysis of a membrane patch antenna. Savings in memory of a factor of 33 over conventional FDTD is observed. This study was published as a paper in last years AP conference [3]. The results shown here are preliminary, but MRTD has the potential to simulate more complicated antenna structures, while preserving the same savings in memory over conventional FDTD.

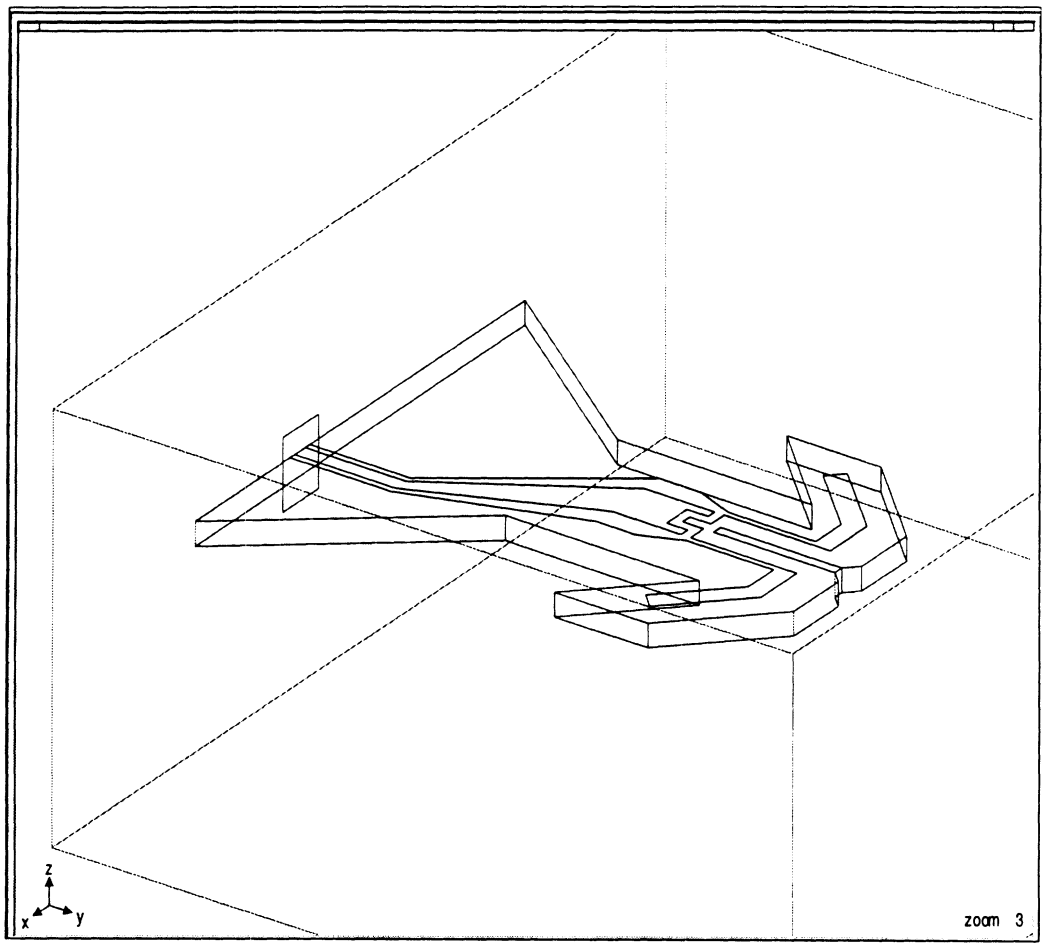

Figure 1: Dual-Polarized Slot-Dipole Antenna.

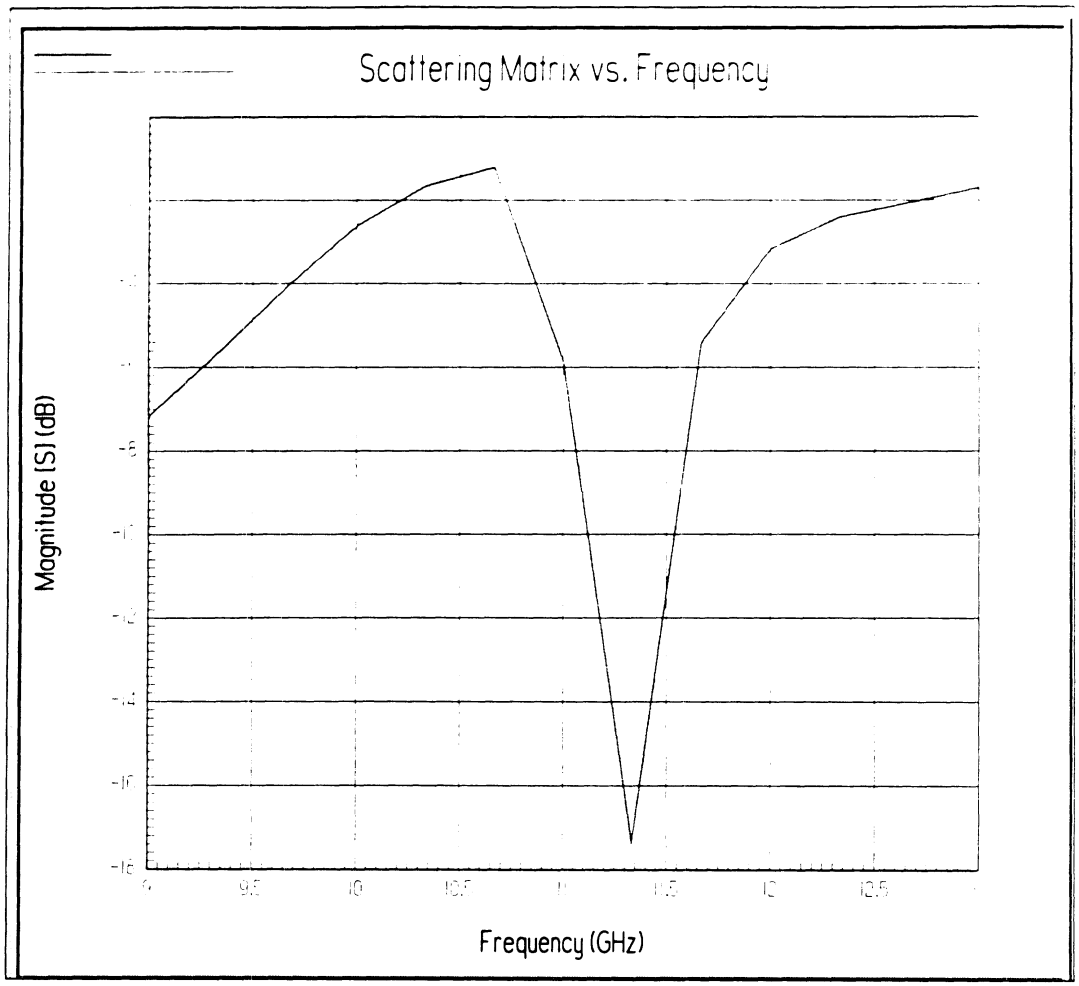

Figure 2: S_{11} Results for the Dual-Polarized Slot-Dipole Antenna.

2.3 Modelling of a Microstrip-to-CPW Transition

The microstrip-to-CPW transition shown in Figure 4 is currently used in the Dual-Polarized Antenna described above. Initial modelling was performed using HFSS, with FDTD code being generated for comparison purposes.

This transition has two advantages. It can be used as an impedance transformer to match the low input impedance of the slot antenna. Additionally it allows feeding on the same side of the substrate, since the dipole is fed with a microstrip. S-parameter results for this transition are shown in Figure 5. Both S_{11} and S_{21} show good performance over a broad frequency range.

FDTD simulations of this transition are underway, with FDTD showing good correlation to the HFSS data in both S-parameters and E-field data. Additionally, this transition will be designed and fully characterized for operations in the 90-100 GHz range.

2.4 FDTD analysis of the Dual-Polarized Antenna

FDTD simulations are performed on the Dual-Polarized Slot Antenna discussed above. During FY-97, preliminary work is performed on the antenna using straight sides. Additional work will be performed in FY-98 to generate an FDTD code to simulate the antenna with a non-orthogonal grid in order to take into account

the angled sides of the final design. Further discussion of goals and the implementation of MRTD in antenna simulations will be carried out in the next section.

3 Goals and Specific Deliverables by Quarter for Fiscal Year 1998

This section will cover goals for FY98. It will include the time frame for the completion of each of the goals listed below The Fiscal Year is divided into quarters and each goal will be listed in terms of the quarter in which it should be completed.

FISCAL YEAR 1998 QUARTERS

Quarter 1 (Q1): October 1, 1997 to December 31, 1997
Quarter 2 (Q2): January 1, 1998 to March 30, 1998
Quarter 3 (Q3): April 1, 1998 to June 30, 1998
Quarter 4 (Q4): July 1, 1998 to September 30, 1998

Each goal is followed by a number or series of numbers which show the quarter in which it will be completed.

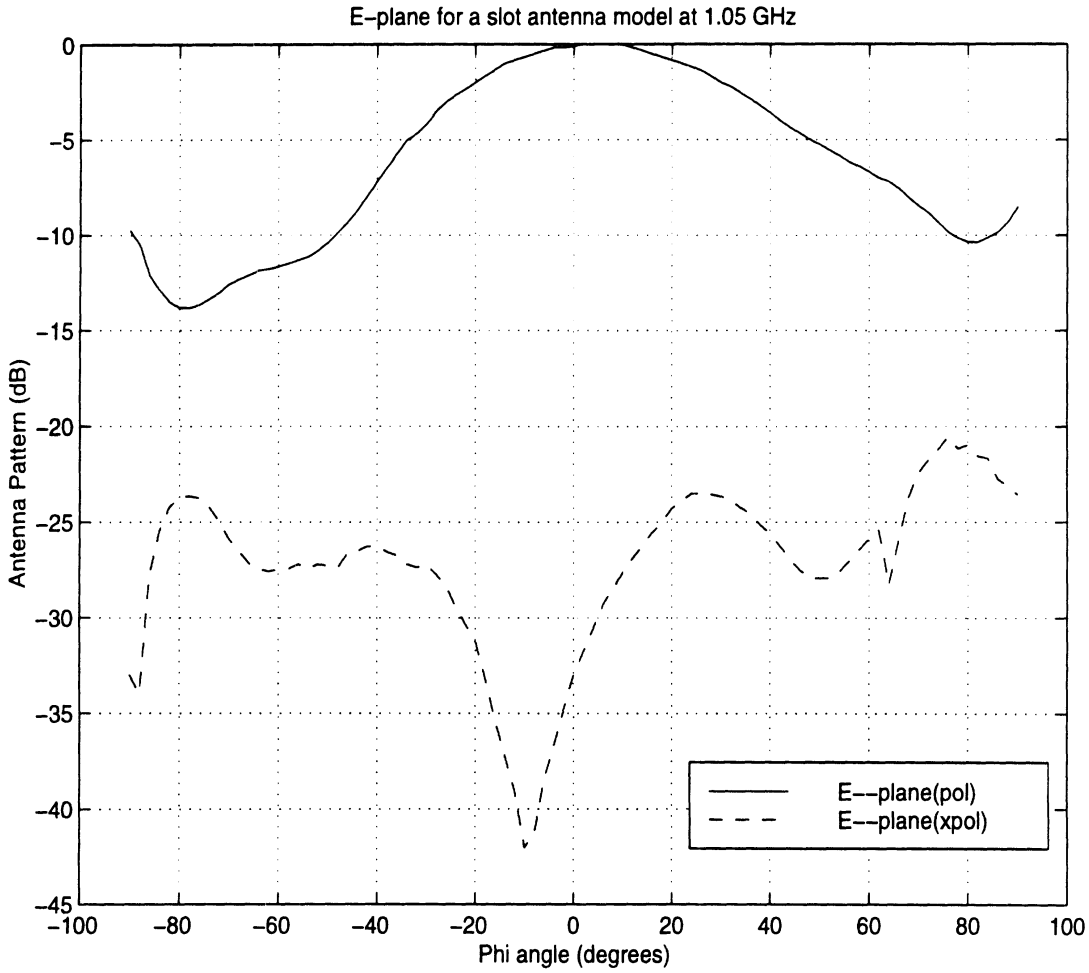

Figure 3: E-plane patterns for the Dual-Polarized Slot-Dipole Antenna.

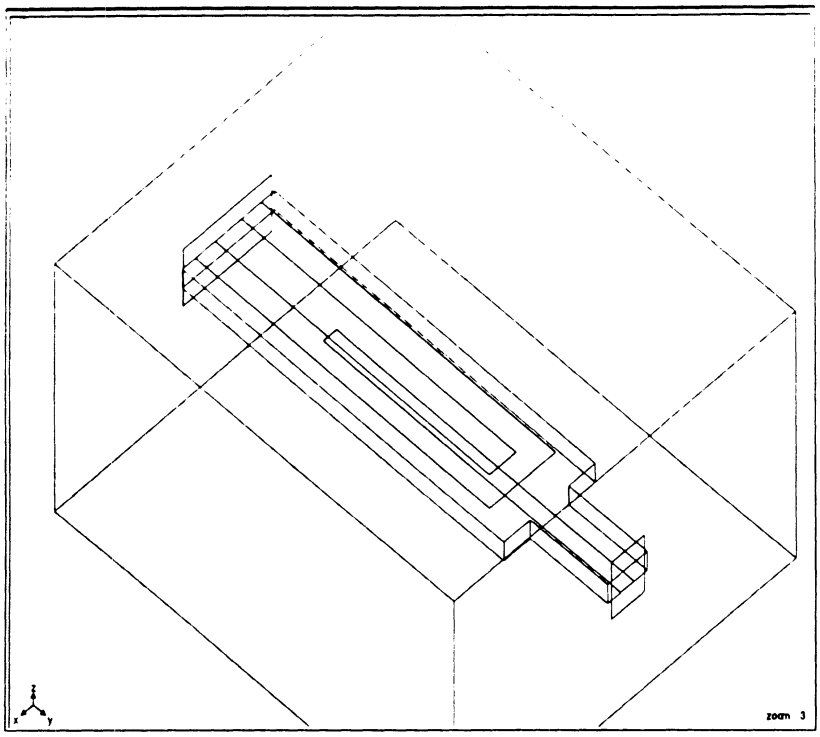

Figure 4: Microstrip-to-CPW Transition.

- 1.) Finish characterization of the Microstrip-to-CPW transition discussed above using FDTD. This work will be published as an AP-98 paper. **(Q1)**

- 2.) Generation of a three-dimensional MRTD code which will allow the quick and efficient modeling of a dielectric substrate. This code will be particularly useful in the simulation of more complex antenna structures. **(Q1-Q2)**

- 3.) Finalize the antenna modeling of the LOCKHEED dipole with only the microstrip to dipole transition. The FDTD code will use the non-orthogonal grid to model the angled sides of the dipole**(Q2-Q3)**.

- 4.) Add in the slot-element in the FDTD code in order to have a full three-dimensional time-domain code to model the complete LOCKHEED dual-polarized antenna**(Q2-Q3)**.

- 5.) For each case 3.) and 4.) described above, check antenna patterns and multi-element (2 to 3) cross-coupling effects**(Q1-Q2-Q3)**.

- 6.) Generation of an MRTD-based code which can model points 3.), 4.) and 5.) discussed above. This will require the design of a non-orthogonal MRTD mesh**(Q2-Q3-Q4)**.

- 7.) Development of time-domain codes which can model more complicated antenna elements, such as active antennas. This will be based on the needs of ARL.**(Q4)**

References

[1] R. Robertson, E. Tentzeris, M. Krumpholz, L.P.B. Katehi, "Modelling of Dielectric Cavity Structures using Multiresolution Time-Domain(MRTD) Analysis", accepted for publication in the January 1998 issue of *International Journal of Numerical Modelling*.

[2] R. Robertson, E. Tentzeris, M. Krumpholz and L.P.B. Katehi, "Application of MRTD Analysis to Dielectric Cavity Structures", *Proc. MTT-S 1996*, pp. 1840-1843.

[3] R. Robertson, E. Tentzeris, and L.P.B. Katehi, "Modelling of Membrane Patch Antennas using MRTD Analysis", *Proc. AP-S 1997*, pp. 126-129.

[4] E.M.Tentzeris, R.Robertson, M.Krumpholz, L.P.B.Katehi, "Application of the PML Absorber to the MRTD Technique", *Proc. AP-S 1996*, pp. 634-637.

[5] B. Edward and D. Rees, "A Broadband Printed Dipole with Integrated Balun", *Microwave Journal*, May, 1987, pp.339-344.

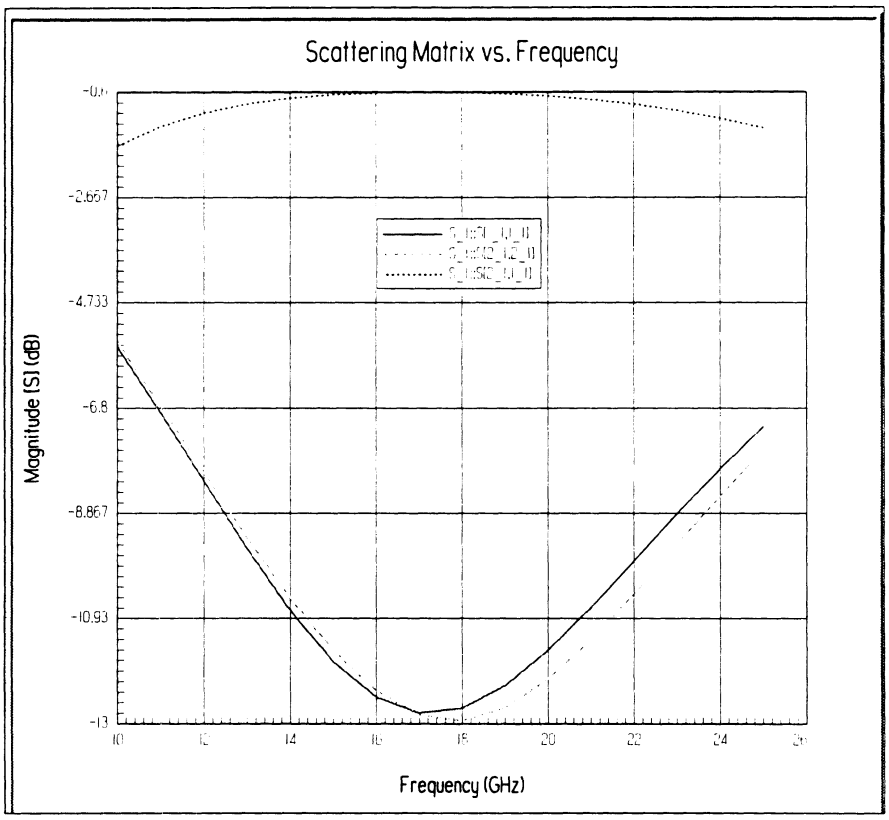

Figure 5: S-parameter results for the Microstrip-to-CPW Transition.

1997 Publication List

Robert L. Robertson

Journal Publications:

1. R. Robertson, E. Tentzeris, M. Krumpholz and L.P.B. Katehi, "Modelling of Dielectric Cavity Structures using Multiresolution Time–Domain(MRTD) Analysis", *International Journal of Numerical Analysis*, Jan-Feb 1998.

2. E. Tentzeris, R. Robertson, J. Harvey, L. Katehi, "Stability and Dispersion Analysis of the Multiresolution Time Domain Method (MRTD)", submitted to *IEEE Transactions on Microwave Theory and Techniques*, January 1998."

3. E. Tentzeris, R. Robertson and L.P.B. Katehi,"A Space- and Time- Adaptive MRTD Gridding Algorithm used for the Analysis of 2D Microwave Geometries", submitted to *IEEE Transactions on Microwave Theory and Techniques*, October 1997.

Conference Publications:

1. R. Robertson, E. Tentzeris, and L.P.B. Katehi, "Modelling of Membrane Patch Antennas using MRTD Analysis", *1997 IEEE AP-S Symposium Proceedings*, pp. 126–129.

2. R. Robertson, E. Tentzeris, T. Ellis and L. Katehi, "Characterization of a CPW-MS Transition for Antenna Applications", submitted to the AP-S98 International Symposium, January 1998.

3. E. Tenteris, R. Robertson and L.P.B. Katehi, "PML Implementation for the Battle–Lemarie Multiresolution Time Domain Scheme", Submitted to the 1998 ACES Conference, Monterey, CA.

4. T.J. Ellis, R.L. Robertson, L.P.B. Katehi and G.M. Rebeiz, "A Dual Polarized Planar Antenna for Phased Array Applications", submitted to the Advanced Sensors Consortium second annual conference, Feb. 2-3, 1997.

5. E. Tentzeris, R. Robertson and L.P.B. Katehi, "Space– and Time–Adaptive Gridding using the MRTD Technique", *1997 IEEE MTT International Microwave Symposium Digest*, pp. 337-340.

Formal Professional Presentations:

1. 1997 IEEE AP-S International Symposium, Interdisciplinary Computational Electromagnetics, APS Special Session.

Modelling of Dielectric Cavity Structures using Multiresolution Time–Domain Analysis

Rob Robertson, Emmanouil Tentzeris, Michael Krumpholz, Linda P.B. Katehi

Radiation Laboratory, Department of Electrical Engineering and Computer Science
University of Michigan, Ann Arbor, MI 48109-2122

Abstract

Multiresolution Time Domain(MRTD) analysis is applied directly to Maxwell's Equations to model inhomogeneous dielectric material. In our approach, scaling and wavelet functions are used as a complete basis for the method of moments. The MRTD scheme is used to analyze different types of resonant cavity structures with varying dielectric perturbations in one, two and three dimensions. The results presented here agree very well with those obtained by FDTD, FEM and Integral Equation methods. MRTD allows for considerable savings in memory and computation time in comparison to FDTD, while maintaining the same accuracy of the results.

1 Introduction

The method of moments [1] is a mathematically correct approach for the discretization of integral and partial differential equations. This technique can be used to derive Yee's FDTD scheme using pulse functions for the expansion of the unknown fields [2, 3]. Since the method of moments allows for the use of a complete set of orthonormal basis functions, the choice of an appropriate set may lead to new discretization schemes. In literature [4, 5], the use of scaling and wavelet functions as a complete set of basis functions is called multiresolution analysis. The MRTD scheme is a fast–growing new method [6, 7, 8] which incorporates the advantages of multiresolution analysis. It has been shown that the MRTD scheme has highly linear dispersion characteristics resulting in a high degree of accuracy in electromagnetic computations for discretizations close to the Nyquist limit. The MRTD scheme presented in this paper is extended for arbitrary resonant cavity structures, with varying dielectrics. Complete formulations for dielectrics in one, two and three dimensions have been developed, using both scaling and wavelet functions.

Battle-Lemarie [9, 10] scaling and wavelet functions are used to represent the electric and magnetic field in several resonant cavity structures. The first is a cavity which is loaded with a quarter–slice dielectric. In this case the ε coefficient varies only along one coordinate direction, which is referred to as a one–dimensional dielectric perturbation. Both the scaling function based MRTD(S–MRTD) and wavelet function based MRTD(Wy–MRTD) scheme achieved excellent correlation with FDTD results and analytic values for discretization close to the Nyquist limit. The second structure is a resonant cavity loaded with a dielectric slice along two coordinate directions, referred to as a two–dimensional dielectric perturbation. As with the previous structure, the S–MRTD method achieved excellent correlation with FDTD results. The final analysis is performed with two different resonant cavities with a dielectric along three coordinate directions, referred to as a three–dimensional dielectric perturbation. In the first case, a cavity has a varying three–dimensional dielectric perturbation in one corner of the structure. It is shown that S–MRTD gives excellent correspondence to FDTD in frequency domain. The second case is a cavity with a varying three–dimensional dielectric perturbation in the center of the bottom side. In this case S–MRTD results are compared to results generated by FEM and Integral Equation (IE) methods. Once again excellent correspondence is achieved between S–MRTD, FEM and IE methods.

2 Modelling Inhomogeneous Dielectric Material

In the S-MRTD scheme, Battle-Lemarie scaling functions [9, 10] are used as a complete set of orthonormal basis functions. This scheme is derived in a homogeneous medium by representing the field components as a series of scaling and pulse functions in space and time domain [11, 12]. For complete multiresolution analysis, first-order wavelet functions are added to produce the Wy-MRTD scheme. The Wy-MRTD scheme in a homogeneous medium is derived by representing the field components as a series of scaling and wavelet functions in space domain and pulse functions in time domain. The situation becomes more complicated for inhomogeneous dielectric media. Since Battle-Lemarie(BL) scaling functions are non-localized in space, they cannot account directly for localized boundary conditions. This section describes how to discretize the appropriate constitutive relations for one-, two- and three-dimensional dielectric perturbations.

2.1 General Derivation

To model the electromagnetic field inside an inhomogeneous dielectric material, Maxwell's first vector equation is separated in:

$$\nabla \times \mathbf{H} = \frac{\partial \mathbf{D}}{\partial t} \tag{1}$$

and

$$\mathbf{D} = \boldsymbol{\epsilon}(\vec{r}, t)\, \mathbf{E} \quad , \tag{2}$$

where $\mathbf{D}$ represents the electric flux vector and $\boldsymbol{\epsilon}(\vec{r}, t)$ the space- and time-dependent permittivity tensor. These equations can be discretized using scaling and pulse functions in space and time domain respectively as expansion factors in the method of moments [11, 12]. The use of non-localized basis functions cannot accomodate localized boundary conditions and cannot allow for a localized modelling of the material properties. To overcome this difficulty, the image principle is used to model perfect electric and magnetic boundary conditions. As for the description of material parameters, the constitutive relations are discretized accordingly so that the relationships between the electric/magnetic flux and the electric/magnetic field are given by matrix equations. In the following, the discretization of eq. (2) using the method of moments is described.

In the principal coordinate system, the permittivity tensor $\boldsymbol{\epsilon}$ for symmetric media is given by

$$\boldsymbol{\epsilon}(\vec{r}, t) = \begin{bmatrix} \varepsilon_x(\vec{r}, t) & 0 & 0 \\ 0 & \varepsilon_y(\vec{r}, t) & 0 \\ 0 & 0 & \varepsilon_z(\vec{r}, t) \end{bmatrix} \quad . \tag{3}$$

In this case, eq. (2) may be written in the form of three scalar cartesian equations as

$$D_x = \varepsilon_x(\vec{r}, t)\, E_x \tag{4}$$

$$D_y = \varepsilon_y(\vec{r}, t)\, E_y \tag{5}$$

$$D_z = \varepsilon_z(\vec{r}, t)\, E_z \quad . \tag{6}$$

For simplicity in the presentation, consider the discretization of eqs. (4), (5) and (6) for field expansions using only scaling functions in space domain. Under this assumption the field expansions of the electric flux and electric field vectors are shown by the following set of equations:

$$\begin{aligned} F_x(\vec{r}, t) &= \sum_{k,l,m,n=-\infty}^{+\infty} {}_kF^{\phi x}_{l+1/2,m,n}\; h_k(t)\; \phi_{l+1/2}(x)\; \phi_m(y)\; \phi_n(z) \\ F_y(\vec{r}, t) &= \sum_{k,l,m,n=-\infty}^{+\infty} {}_kF^{\phi y}_{l,m+1/2,n}\; h_k(t)\; \phi_l(x)\; \phi_{m+1/2}(y)\; \phi_n(z) \\ F_z(\vec{r}, t) &= \sum_{k,l,m,n=-\infty}^{+\infty} {}_kF^{\phi z}_{l,m,n+1/2}\; h_k(t)\; \phi_l(x)\; \phi_m(y)\; \phi_{n+1/2}(z) \end{aligned} \tag{7}$$

where ${}_kF(\vec{r},t) = ({}_kE(\vec{r},t), {}_kD(\vec{r},t))$ with $\kappa = x, y, z$. The coefficients ${}_kI^{\phi\kappa}_{l,m,n}$ represent the field expansion coefficients in terms of scaling functions. The indices l, m, n and k are the discrete space and time indices related to the space and time coordinates via $x = l\Delta x$, $y = m\Delta y$, $z = n\Delta z$ and $t = k\Delta t$, where Δx, Δy, Δz and Δt represent the space and time discretization intervals in x-, y-, z- and t-direction. The function $h_m(x)$ is defined as

$$h_m(x) = h(\frac{x}{\Delta x} - m) \tag{8}$$

where $h(x)$ is a rectangular pulse function given by

$$h(x) = \begin{cases} 1 & \text{for } |x| < 1/2 \\ 1/2 & \text{for } |x| = 1/2 \\ 0 & \text{for } |x| > 1/2 \end{cases} \quad . \tag{9}$$

The function $\phi_m(x)$ is defined as

$$\phi_m(x) = \phi(\frac{x}{\Delta x} - m) \quad , \tag{10}$$

where $\phi(x)$ represents the cubic spline Battle–Lemarie scaling functions [9, 10].

The field equations shown in eq. (7) are inserted into eqs. (4), (5) and (6) and the equations are sampled using pulse functions with respect to time and scaling test functions with respect to space. Assuming

$$\varepsilon_\kappa(\vec{r},t) = \varepsilon_\kappa(x)\ \varepsilon_\kappa(y)\ \varepsilon_\kappa(z)\ \varepsilon_\kappa(t) \tag{11}$$

and sampling eq. (4) with $\phi_{l+1/2}(x)\ \phi_m(y)\ \phi_n(z)\ h_k(t)$ yields

$${}_kD^{\phi x}_{l+1/2,m,n} = \sum_{k',l',m',n'=-\infty}^{+\infty} \varepsilon^{\phi x}_{(x)l+1/2,l+1/2'}\ \varepsilon^{\phi x}_{(y)m,m'}\ \varepsilon^{\phi x}_{(z)n,n'}\ \varepsilon^{x}_{(t)k,k'}\ \ {}_{k'}E^{\phi z}_{l'+1/2,m',n'} \quad , \tag{12}$$

where $\varepsilon^{\phi x}_{(\kappa)m,m'}$ and $\varepsilon^{x}_{(t)k,k'}$ are integrals given by

$$\varepsilon^{\phi x}_{(\kappa)m,m'} = \frac{1}{\Delta\kappa}\int_{-\infty}^{+\infty} \phi_m(\kappa)\ \varepsilon_x(\kappa)\ \phi_{m'}(\kappa)\ d\kappa \tag{13}$$

and

$$\varepsilon^{x}_{(t)k,k'} = \frac{1}{\Delta t}\int_{-\infty}^{+\infty} h_k(t)\ \varepsilon_x(t)\ h_{k'}(t)\ dt \quad . \tag{14}$$

In subsequent sections, the derivation of specific expressions for the dielectrics in one, two and three dimensions are presented.

2.2 Analysis of Resonant Cavities with One–Dimensional Dielectrics

In this section the equations describing a dielectric perturbation that varies only along one direction are derived. Consider for example the structure shown in Figure 1. This structure has a dielectric constant which varies only along the y–axis and is homogeneous along the x– and z–directions, with no time–dependence. Therefore, the non–zero elements of our permittivity tensor are as follows:

$$\varepsilon_x(\vec{r},t) = \varepsilon_x(y) \tag{15}$$

$$\varepsilon_y(\vec{r},t) = \varepsilon_y(y) \tag{16}$$

$$\varepsilon_z(\vec{r},t) = \varepsilon_z(y) \quad . \tag{17}$$

Applying eqs. (15), (16) and (17) to eqs. (4), (5) and (6), and using the field expansions in eq. (7) yields:

$$ {}_kD^{\phi x}_{l+1/2,m,n} = \sum_{m'=-\infty}^{+\infty} \varepsilon^{\phi x}_{(y)m,m'} \; {}_{k'}E^{\phi x}_{l'+1/2,m',n'} \tag{18} $$

$$ {}_kD^{\phi y}_{l,m+1/2,n} = \sum_{m'=-\infty}^{+\infty} \varepsilon^{\phi y}_{(y)m+1/2,m'+1/2} \; {}_{k'}E^{\phi y}_{l',m'+1/2,n'} \tag{19} $$

$$ {}_kD^{\phi z}_{l,m,n+1/2} = \sum_{m'=-\infty}^{+\infty} \varepsilon^{\phi z}_{(y)m,m'} \; {}_{k'}E^{\phi z}_{l',m',n'+1/2} \tag{20} $$

where the integrals $\varepsilon^{\phi x}_{(y)m,m'}$, $\varepsilon^{\phi y}_{(y)m+1/2,m'+1/2}$ and $\varepsilon^{\phi z}_{(y)m,m'}$ are given by:

$$ \varepsilon^{\phi x}_{(y)m,m'} = \frac{1}{\Delta y} \int_{-\infty}^{+\infty} \phi_m(y) \; \varepsilon_x(y) \; \phi_{m'}(y) \; dy \tag{21} $$

$$ \varepsilon^{\phi y}_{(y)m+1/2,m'+1/2} = \frac{1}{\Delta y} \int_{-\infty}^{+\infty} \phi_{m+1/2}(y) \; \varepsilon_y(y) \; \phi_{m'+1/2}(y) \; dy \tag{22} $$

$$ \varepsilon^{\phi z}_{(y)m,m'} = \frac{1}{\Delta y} \int_{-\infty}^{+\infty} \phi_m(y) \; \varepsilon_z(y) \; \phi_{m'}(y) \; dy \tag{23} $$

Note that although the limits of integration are infinite the Battle–Lemarie scaling functions exponentially decay to zero after $\pm 6\Delta l$, which significantly truncates the limits of the integration.

For the evaluation of the integrals, eqs. (21) – (23), a simple representation of the scaling function in terms of cubic spline functions is used [12]. The structure shown in Figure 1 is used to illustrate an evaluation of the integrals. This structure is a resonant cavity that is one–quarter filled with a dielectric material. The cavity has the dimensions $1cm \times 2cm \times 1.5cm$, and the dielectric material has a relative dielectric constant equal to 10. A discretization of $2 \times 6 \times 3$ is applied for the method described below. The electric field components tangential to the dielectric interface, ${}_{k'}E^{\phi x}_{l',m',n'}$ and ${}_{k'}E^{\phi z}_{l',m',n'}$ are related to ${}_kD^{\phi x}_{l,m,n}$ and ${}_kD^{\phi x}_{l,m,n}$ by the tangential epsilon(ε) coefficients $\varepsilon^{\phi x}_{(y)}$ and $\varepsilon^{\phi z}_{(y)}$ respectively. Additionally, the electric field component normal to the dielectric interface ${}_{k'}E^{\phi y}_{l',m',n'}$ is related to ${}_{k'}D^{\phi y}_{l',m',n'}$ by the normal (ε) coefficient $\varepsilon^{\phi y}_{(y)}$. To model the structure in Figure 1 the image principle is applied, thus replacing the structure in Figure 1 by the structures shown in Figures 2 and 3 respectively. The tangential ε coefficients now relate ten ${}_{k'}E^{\phi x}_{l',m',n'}$ components to ten ${}_kD^{\phi x}_{l,m,n}$ components through a 10×10 matrix. The image principle applies odd symmetry of the tangential electric fields. Thus the five tangential electric field components in the image resonator are linearly dependent on the five tangential electric field components in the original resonator. This allows the elimination of the field components in the image resonator, reducing the 10×10 matrix to a 5×5 matrix, which is used in eq. (8). Similarly, the 12×12 matrix of the normal ε coefficient is reduced to a 6×6 matrix using even symmetry for the normal electric field component. Note that a general description of ε coefficients in eq. (9) allows for an arbitrary positioning of the dielectric interface.

The MRTD method for the structure in Figure 1 at a discretization of $2 \times 6 \times 3$ proved to be the closest approximation to analytic values. This is due to the fact that a discretization of $2 \times 4 \times 3$ is exactly at the Nyquist criterion for the variation of ε in the y–direction (one sampling point in the dielectric material).

MRTD results are compared to analytic values and the results obtained by Yee's FDTD scheme in Table 1. The same value for the time discretization interval $\Delta t = 0.9 \cdot 10^{-10} s$ is used for both schemes. This time step interval is chosen to maximize the linear properties of the MRTD dispersion relation [12]. Both cases run for 35,000 time steps. For the analysis using Yee's FDTD scheme, a mesh with $\Delta x = \Delta y = \Delta z = 0.1cm$ is used resulting in a total number of 3000 grid points. In the $2 \times 6 \times 3$ analysis, a total number of 36 grid points is used, resulting in a memory improvement by a factor of 83 for MRTD. Additionally an improvement by a factor of 10 in computation time is found for the MRTD method.

Analytic (GHz)	6.6990	8.7805	9.3007
FDTD ($10 \times 20 \times 15$)	6.686	8.770	9.270
FDTD Relative Error	-0.194%	-0.119%	-0.330%
S-MRTD ($2 \times 6 \times 3$)	6.707	8.800	9.343
MRTD Relative Error	0.119%	0.222%	0.453%

Table 1: Resonant Frequency data for a cavity one-quarter filled with dielectric material

Due to the properties of multiresolution analysis, MRTD has a unique ability to calculate field distributions. While a method such as FDTD results in only one field value per discretization cell, MRTD scaling functions imply field variations within the discretization cell. Deriving MRTD and FDTD using the method of moments, the field components have to be interpreted as field expansion coefficients. From the different field expressions, it is clear that the field expansion coefficients of the FDTD scheme represent the total field value at a specific point, while the field expansion coefficients of the MRTD scheme represent a fraction of the total field. To calculate the total field at a space point, the field expansions are sampled with delta test functions in space and time domain. For example, the total electric field $E_y(x_o, y_o, z_o, t_o)$ with $(k - 1/2)\,\Delta t < t_o < (k + 1/2)\,\Delta t$ is calculated by

$$\begin{aligned} E_x(x_o, y_o, z_o, t_o) &= \int\int\int\int E_y(x, y, z, t)\,\delta(x - x_o)\,\delta(y - y_o)\,\delta(z - z_o)\,\delta(t - t_o)\,dx\,dy\,dz\,dt \\ &= \sum_{l',m',n'=-\infty}^{\infty} {}_kE^{y,\phi\phi\phi}_{l',m'+1/2,n'}\,\phi_{l'}(x_o)\,\phi_{m'+1/2}(y_o)\,\phi_{n'}(z_o) \quad . \end{aligned} \tag{24}$$

Practically, the above summation is truncated to very few terms (6–8 per index), due to the exponentially decaying support of the Battle-Lemarie scaling function.

Figures 4 and 5 show plots of $E^{\phi y}$ calculated using S-MRTD with a discretization of $2 \times 8 \times 3$ for the quarter-slice dielectric. Figure 4 shows the amplitudes of the scaling functions calculated by MRTD. Figure 5 shows field distributions using seven intermediate points along each of the coordinate axis. Figure 6 shows a field plot calculated by FDTD with a discretization of $20 \times 40 \times 30$. It should be noted that execution time for the interpolation was extremely low.

As mentioned above, for true multiresolution analysis, wavelets must be added to discretize Maxwell's equations in space domain. Therefore, consider the discretization of eqs. (4)- (6) for field expansions with scaling and wavelet functions in space domain. The expansions of the field components are now a two-fold expansion in scaling and wavelet functions with respect to the y-axis as shown below:

$$\begin{aligned} F_x(\vec{r}, t) &= \sum_{k,l,m,n=-\infty}^{+\infty} \left({}_kF^{\phi x}_{l+1/2,m,n}\,\phi_m(y) + {}_kF^{\psi x}_{l+1/2,m+1/2,n}\,\psi_{m+1/2}(y) \right) h_k(t)\,\phi_{l+1/2}(x)\,\phi_n(z) \\ F_y(\vec{r}, t) &= \sum_{k,l,m,n=-\infty}^{+\infty} \left({}_kF^{\phi y}_{l,m+1/2,n}\,\phi_{m+1/2}(y) + {}_kF^{\psi y}_{l,m,n}\,\psi_m(y) \right) h_k(t)\,\phi_l(x)\,\phi_n(z) \\ F_z(\vec{r}, t) &= \sum_{k,l,m,n=-\infty}^{+\infty} \left({}_kF^{\phi z}_{l,m,n+1/2}\,\phi_m(y) + {}_kF^{\psi z}_{l,m+1/2,n+1/2}\,\psi_{m+1/2}(y) \right) h_k(t)\,\phi_l(x)\,\phi_{n+1/2}(z) \end{aligned} \tag{25}$$

where ${}_kF(\vec{r}, t) = ({}_kE(\vec{r}, t), {}_kD(\vec{r}, t))$ with $\kappa = x, y, z$. Inserting eqs. (15), (16) and (17) into eqs. (4), (5) and (6) while using the expansions given in eq. (25) and the procedure discussed above yields:

Analytic (GHz)	6.699	8.7805	9.300
Wy-MRTD (6 wavelets)	6.703	8.7825	9.315
Wy-MRTD Relative Error	0.0596%	0.0227%	0.1613%
Wy-MRTD (4 wavelets)	6.705	8.7850	9.325
Wy-MRTD Relative Error	0.0894%	0.05122%	0.268%

Table 2: Resonant Frequency data for a cavity one-quarter filled with dielectric material with the application of wavelets along the y-direction

$$ {}_kD^{\phi x}_{l+1/2,m,n} = \sum_{m'=-\infty}^{+\infty} \left(\varepsilon^{\phi x}_{(y)m,m'} \; {}_kE^{\phi x}_{l+1/2,m',n} + \varepsilon^{Ix}_{(y)m,m'+1/2} \; {}_kE^{\psi x}_{l+1/2,m'+1/2,n} \right) \tag{26} $$

$$ {}_kD^{\psi x}_{l+1/2,m+1/2,n} = \sum_{m'=-\infty}^{+\infty} \left(\varepsilon^{Ix}_{(y)m',m+1/2} \; {}_kE^{\phi x}_{l+1/2,m',n} + \varepsilon^{\psi x}_{(y)m+1/2,m'+1/2} \; {}_kE^{\psi x}_{l+1/2,m'+1/2,n} \right) \tag{27} $$

$$ {}_kD^{\phi y}_{l,m+1/2,n} = \sum_{m'=-\infty}^{+\infty} \left(\varepsilon^{\phi y}_{(y)m+1/2,m'+1/2} \; {}_kE^{\phi y}_{l,m'+1/2,n} + \varepsilon^{Iy}_{(y)m+1/2,m'} \; {}_kE^{\psi y}_{l,m',n} \right) \tag{28} $$

$$ {}_kD^{\psi y}_{l,m,n} = \sum_{m'=-\infty}^{+\infty} \left(\varepsilon^{Iy}_{(y)m'+1/2,m} \; {}_kE^{\phi y}_{l,m'+1/2,n} + \varepsilon^{\psi y}_{(y)m,m'} \; {}_kE^{\psi y}_{l,m',n} \right) \tag{29} $$

$$ {}_kD^{\phi z}_{l,m,n+1/2} = \sum_{m'=-\infty}^{+\infty} \left(\varepsilon^{\phi z}_{(y)m,m'} \; {}_kE^{\phi z}_{l,m',n+1/2} + \varepsilon^{Iz}_{(y)m',m+1/2} \; {}_kE^{\psi z}_{l,m'+1/2,n+1/2} \right) \tag{30} $$

$$ {}_kD^{\psi z}_{l,m+1/2,n+1/2} = \sum_{m'=-\infty}^{+\infty} \left(\varepsilon^{Iz}_{(y)m+1/2,m'} \; {}_kE^{\phi z}_{l,m',n+1/2} + \varepsilon^{\psi z}_{(y)m+1/2,m'+1/2} \; {}_kE^{\psi z}_{l,m'+1/2,n+1/2} \right) \tag{31} $$

The new generalized integral identities are:

$$ \varepsilon^{\psi\kappa}_{(y)m,m'} = \frac{1}{\Delta y} \int_{-\infty}^{+\infty} \psi_m(y) \; \varepsilon_\kappa(y) \; \psi_{m'}(y) \; dy \tag{32} $$

and

$$ \varepsilon^{I\kappa}_{(y)m,m'} = \frac{1}{\Delta y} \int_{-\infty}^{+\infty} \phi_m(y) \; \varepsilon_\kappa(y) \; \psi_{m'}(y) \; dy \quad . \tag{33} $$

The procedure for evaluating the integrals is similar to the procedure discussed for equations eqs. (21) - (23).

Data for the structure shown in Figure 1 is presented in Table 2, with 4 and 6 wavelets added along the y-direction. As can be seen from Table 2, adding wavelets increases the resonant frequency resolution.

2.3 Analysis of Resonant Cavity with 2D Dielectric

This section shows the derivation of the equations describing a dielectric perturbation that varies along two coordinate directions. Consider the structure shown in Figure 7, where the dielectric varies along the x- and y-directions and is constant in the z-direction. In this structure, the non-zero elements of the permittivity tensor are as follows:

$$ \varepsilon_x(\vec{r},t) = \varepsilon_x(x,y) \tag{34} $$

$$ \varepsilon_y(\vec{r},t) = \varepsilon_y(x,y) \tag{35} $$

$$ \varepsilon_z(\vec{r},t) = \varepsilon_z(x,y) \quad . \tag{36} $$

FDTD ($40 \times 40 \times 40$) (GHz)	1.9640
S-MRTD ($6 \times 6 \times 6$)	1.9480
FDTD/MRTD Relative Error	0.814%
S-MRTD ($8 \times 8 \times 8$)	1.9610
FDTD/MRTD Relative Error	0.152%
S-MRTD ($10 \times 10 \times 10$)	1.9610
MRTD Relative Error	0.152%

Table 3: Resonant Frequency data for a cavity one-quarter filled with dielectric material

Following the procedure above, eqs. (34), (35) and (36) are applied to eqs. (4), (5) and (6). Then, using the field expansions given by eq. (7) yields:

$$ {}_kD^{\phi x}_{l+1/2,m,n} = \sum_{l',m'=-\infty}^{+\infty} \varepsilon^{\phi x}_{(x,y)l+1/2,l'+1/2,m,m'} \; {}_{k'}E^{\phi x}_{l'+1/2,m',n'} \tag{37} $$

$$ {}_kD^{\phi y}_{l,m+1/2,n} = \sum_{l',m'=-\infty}^{+\infty} \varepsilon^{\phi y}_{(x,y)l,l',m+1/2,m'+1/2} \; {}_{k'}E^{\phi y}_{l',m'+1/2,n'} \tag{38} $$

$$ {}_kD^{\phi z}_{l,m,n+1/2} = \sum_{n'=-\infty}^{+\infty} \varepsilon^{\phi z}_{(x,y)l,l',m,m'} \; {}_{k'}E^{\phi z}_{l',m',n'+1/2} \tag{39} $$

where the integrals $\varepsilon^{\phi x}_{(x,y)l+1/2,l'+1/2,m,m'}$, $\varepsilon^{\phi y}_{(x,y)l,l',m+1/2,m'+1/2}$ and $\varepsilon^{\phi z}_{(z)l,l',m,m'}$ are given by:

$$ \varepsilon^{\phi x}_{(x,y)l+1/2,l'+1/2,m,m'} = \frac{1}{\Delta x \Delta y} \int_{-\infty}^{+\infty} \int_{-\infty}^{+\infty} \varepsilon_x(x,y) \; \phi_{l+1/2}(x) \; \phi_{l'+1/2}(x) \; \phi_m(y) \; \phi_{m'}(y) \; dx \; dy \tag{40} $$

$$ \varepsilon^{\phi y}_{(x,y)l,l',m+1/2,m'+1/2} = \frac{1}{\Delta x \Delta y} \int_{-\infty}^{+\infty} \int_{-\infty}^{+\infty} \varepsilon_y(x,y) \; \phi_l(x) \; \phi_{l'}(x) \; \phi_{m+1/2}(y) \; \phi_{m'+1/2}(y) \; dx \; dy \tag{41} $$

$$ \varepsilon^{\phi z}_{(x,y)l,l',m,m'} = \frac{1}{\Delta x \Delta y} \int_{-\infty}^{+\infty} \int_{-\infty}^{+\infty} \varepsilon_z(x,y) \; \phi_l(x) \; \phi_{l'}(x) \; \phi_m(y) \; \phi_{m'}(y) \; dx \; dy \tag{42} $$

The evaluation of eqs. (40) and (41) is similar to the procedure described for one-dimensional dielectric perturbations. This procedure is illustrated by applying a discretization of $6 \times 6 \times 6$ to the structure in Figure 7. This structure has the dimensions $6cm \times 6cm \times 6cm$, with a one-third dielectric slice along the x- and y-directions. The dielectric has a relative permittivity equal to 6. Here, the electric field components ${}_{k'}E^{\phi x}_{l',m',n'}$ and ${}_{k'}E^{\phi y}_{l',m',n'}$ are related to ${}_kD^{\phi x}_{l,m,n}$ and ${}_kD^{\phi y}_{l,m,n}$ by a $6 \times 6 \times 6 \times 6$ matrix described by $\varepsilon^{\phi x}_{(x,y)}$ and $\varepsilon^{\phi y}_{(x,y)}$ respectively. To evaluate the integrals, the image theory is applied, thus replacing Figure 7 by a new structure made by imaging Figure 7 about the x and y axis. Now the electric field components ${}_{k'}E^{\phi x}_{l',m',n'}$ and ${}_{k'}E^{\phi y}_{l',m',n'}$ are related to ${}_kD^{\phi x}_{l,m,n}$ and ${}_kD^{\phi y}_{l,m,n}$ by a $6 \times 6 \times 12 \times 12$ matrix. Each of the $\varepsilon^{\phi x}_{(x,y)}$ and $\varepsilon^{\phi y}_{(x,y)}$ matrix components is calculated by applying eqs. (40) and (41) over the new imaged structure. The epsilon components in each of the three image resonators are linearly dependent on the components in the original resonator. Therefore, the the image theory is applied again, reducing the $6 \times 6 \times 12 \times 12$ matrix to a $6 \times 6 \times 6 \times 6$ matrix. Note that this can be repeated for any discretization along the x-, y- or z-directions.

S-MRTD results for the structure in Figure 7 are shown in Table 2 above. A time discretization interval of $\Delta t = 1.0 \cdot 10^{-12} s$ and 80,000 time steps is used for FDTD, which has a discretization of $40 \times 40 \times 40$. The time discretization interval for S-MRTD $6 \times 6 \times 6$, S-MRTD $8 \times 8 \times 8$ and S-MRTD $10 \times 10 \times 10$ is $\Delta t = 3.0 \cdot 10^{-12} s$. In all three cases 60,000 time steps were used to generate frequency data. The S-MRTD discretization of $6 \times 6 \times 6$ provided excellent correlation with the FDTD method, resulting in a memory savings

r	FDTD(40x40x40)	MRTD(6x6x6)	MRTD(8x8x8)
0.15	3.534	3.524	3.529
0.25	3.500	3.489	3.497
0.33	3.136	3.139	3.137

Table 4: Resonant Frequencies for a resonator with a corner dielectric perturbation

of a factor of 125. Additionally execution time for the S-MRTD method was found to be significantly lower. Figures 8,9 and 10 show field distributions for S-MRTD and FDTD. Figure 8 is a plot of the E^{oy} field for the non-interpolated S-MRTD method with a discretization of $8 \times 8 \times 8$. Figure 9 is an interpolated plot of the E^{oy} distribution with seven intermediate points, resulting in a total discretization of $56 \times 56 \times 56$. The FDTD field plot shown in Figure 10 has a discretization of $40 \times 40 \times 40$. Note the high degree of correlation between the S-MRTD and FDTD field plots.

2.4 Analysis of Resonant Cavity with 3D Dielectric

The equations describing a dielectric perturbation that varies along all three coordinate directions is described in this section. Consider the structures shown in Figures 11 and 12, where the dielectric varies along the x-, y- and z- directions. In this structure, the non-zero elements of the permittivity tensor are as follows:

$$\varepsilon_x(\vec{r},t) = \varepsilon_x(x,y,z) \tag{43}$$

$$\varepsilon_y(\vec{r},t) = \varepsilon_y(x,y,z) \tag{44}$$

$$\varepsilon_z(\vec{r},t) = \varepsilon_z(x,y,z) \quad . \tag{45}$$

Applying a similar procedure to eqs. (43), (44) and (45), the following results for ${}_kD^{\phi x}_{l+1/2,m,n}$ are received:

$${}_kD^{\phi x}_{l+1/2,m,n} = \sum_{l',m',n'=-\infty}^{+\infty} \varepsilon^{\phi x}_{(x,y,z)l+1/2,l'+1/2,m,m',n,n'} \; {}_{k'}E^{\phi x}_{l'+1/2,m',n'} \tag{46}$$

The $\varepsilon^{\phi x}_{(x,y,z)l+1/2,l'+1/2,m,m',n,n'}$ integral is given by:

$$\varepsilon^{\phi x}_{(x,y,z)l+1/2,l'+1/2,m,m',n,n'} = \frac{1}{\Delta x \Delta y \Delta z} \int_{-\infty}^{+\infty} \int_{-\infty}^{+\infty} \int_{-\infty}^{+\infty} \varepsilon_x(x,y,z)\; \phi_{l+1/2}(x)\; \phi_{l'+1/2}(x) \times \phi_m(y)\; \phi_{m'}(y)\; \phi_n(z)\; \phi_{n'}(z)\; dx\; dy\; dz \tag{47}$$

The first structure considered is a resonant cavity 6 cm on a side with a varying dielectric of relative permittivity equal to 6. In this case the varying dielectric is located in one corner of the structure, as shown in Figure 11. The S-MRTD simulations ran for 60,000 time steps, with $\Delta t = 3.0 \cdot 10^{-12} s$. FDTD simulations ran for 100,000 time steps with $\Delta t = 2.0 \cdot 10^{-12} s$. Note that FDTD needed to run for a high number of time steps in order to achieve convergence with the S-MRTD results. Results are shown in Table 4. Note that FDTD and S-MRTD have a high degree of convergence in the resonant frequency data.

The second 3D dielectric structure simulated is a varying dielectric cube with a relative permittivity equal to 6. In this case the cube is located in the center of the bottom face of the structure as shown in Figure 12. This structure has previously been simulated with tetrahedral FEM and an integral equation method [13] and is compared to S-MRTD in Table 4. Once again a high degree of convergence is achieved between the methods.

r	IE/MoM(GHz)	FEM	MRTD(6x6x6)	MRTD(8x8x8)
0.10	6.220	6.1875	6.19	6.20
0.15	6.1535	6.1125	6.11	6.12
0.20	6.02	5.9125	5.945	5.975
0.25	5.840	5.740	5.73	5.75

Table 5: Resonant Frequencies for a resonator with a center dielectric perturbation

3 Conclusion

MRTD schemes based on orthonormal wavelet expansions are derived and applied in the numerical analysis of simple resonant cavity structures. It is shown in this paper that a multiresolution expansion using Battle-Lemarie scaling functions has excellent correspondence with the FDTD method. In comparison with Yee's FDTD scheme, the examples suggest computer savings of two orders of magnitude with respect to the memory requirements.

Acknowledgements

This work has been made possible by a scholarship of the NATO science committee through the German Academic Exchange Service and by the U.S. Army Research Office.

References

[1] R.F. Harrington, "Field Computation by Moment Methods", Krieger Publishing Company, Inc., Malabar, Florida, 1982.

[2] M. Krumpholz, P. Russer, "Two-Dimensional FDTD and TLM", Int. Journal of Num. Modelling, vol. 7, no. 2, pp. 141-153, February 1993.

[3] M. Krumpholz, C. Huber, P. Russer, "A Field Theoretical Comparison of FDTD and TLM", IEEE Transactions on Microwave Theory and Techniques, vol. 43, no. 8, pp. 1935-1950, August 1995.

[4] S.G. Mallat, "A Theory for Multiresolution Signal Decomposition: The Wavelet Representation", IEEE Trans. Pattern Anal. Machine Intell., vol. 11, pp. 674-693, July 1989.

[5] B. Jawerth, W. Sweldens, "An Overview of Wavelet Based Multiresolution Analyses", SIAM Review, vol. 36, no. 3, pp. 377-412, September 1994.

[6] R. Robertson, E. Tentzeris, M. Krumpholz, L.P.B. Katehi, "MRTD Analysis of Dielectric Cavity Structures", 1996 IEEE MTT International Microwave Symposium Digest, pp. 1861-1864.

[7] E. Tentzeris, M. Krumpholz, L.P.B. Katehi, "Application of MRTD to Printed Transmission Lines", 1996 IEEE MTT International Microwave Symposium Digest, pp. 573-577.

[8] M.Krumpholz, H.Winful, L.P.B.Katehi, "Nonlinear Time Domain Modelling by MRTD", 1996 IEEE MTT International Microwave Symposium Digest, pp. 597-601.

[9] G. Battle, "A block spin construction of ondelettes", Comm. Math. Phys., vol. 110, pp. 601-615, 1987.

[10] P.G. Lemarie, "Ondelettes a localisation exponentielle", J. Math. Pures Appl., vol. 67, pp. 227-236, 1988.

[11] M. Krumpholz, L.P.B. Katehi, "New Prospects for Time-Domain Analysis", IEEE Microwave Guided Lett., vol. 5, no. 11, pp. 382-384, 1995.

[12] M. Krumpholz, L.P.B. Katehi, "MRTD: New Time Domain Schemes Based on Multiresolution Analysis", IEEE Transactions on Microwave Theory and Techniques, vol. 44, pp. 555-571, May 1995.

[13] J.G. Yook and Kazem Sabet, private communication.

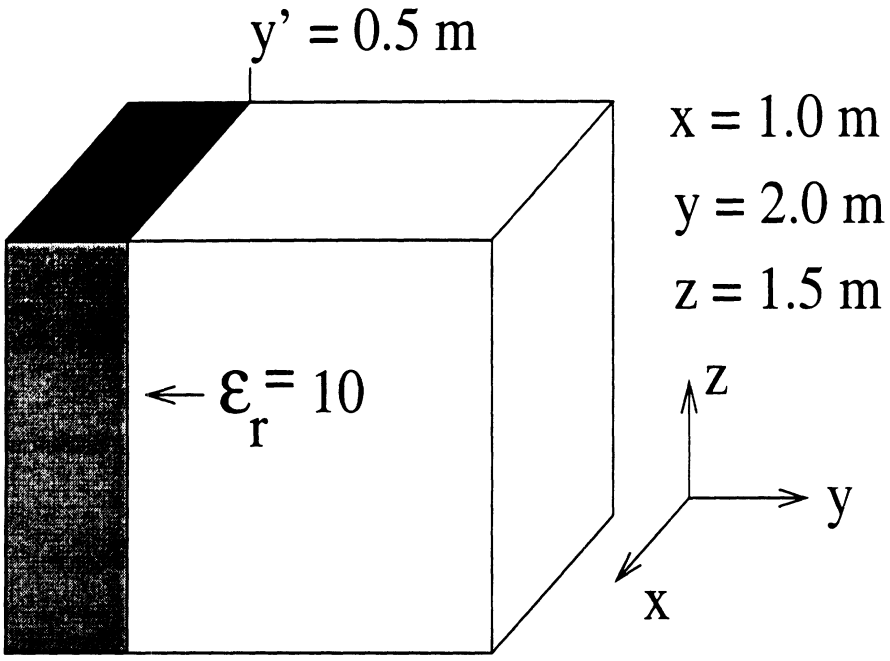

Figure 1: Cavity Resonator one-quarter filled with dielectric

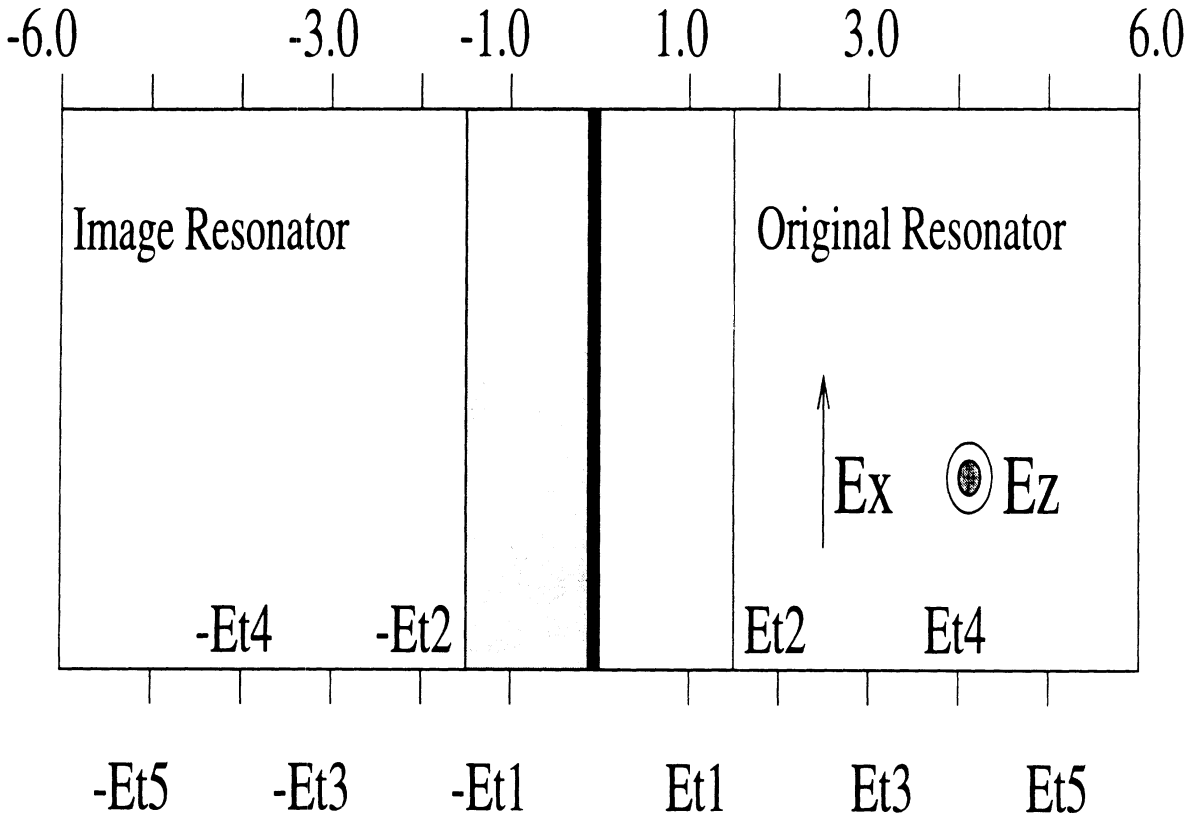

Figure 2: Tangential epsilon components

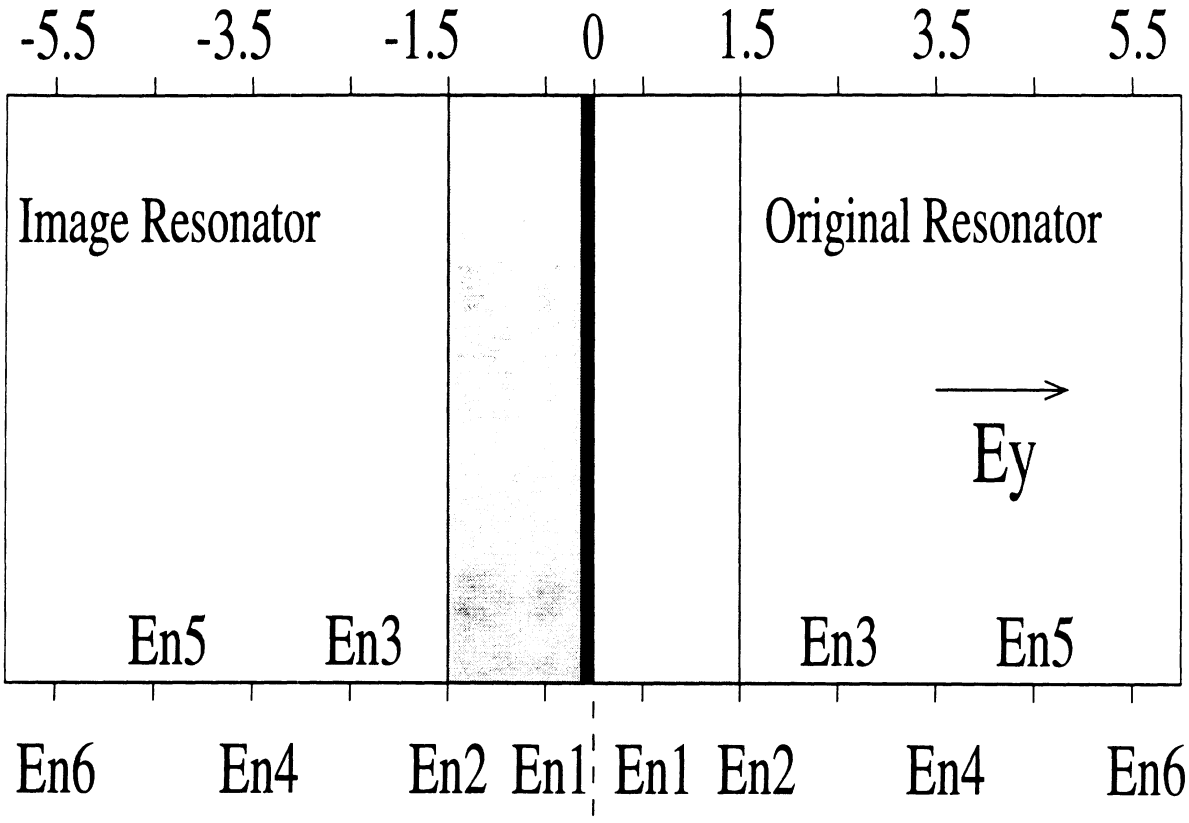

Figure 3: Normal epsilon components

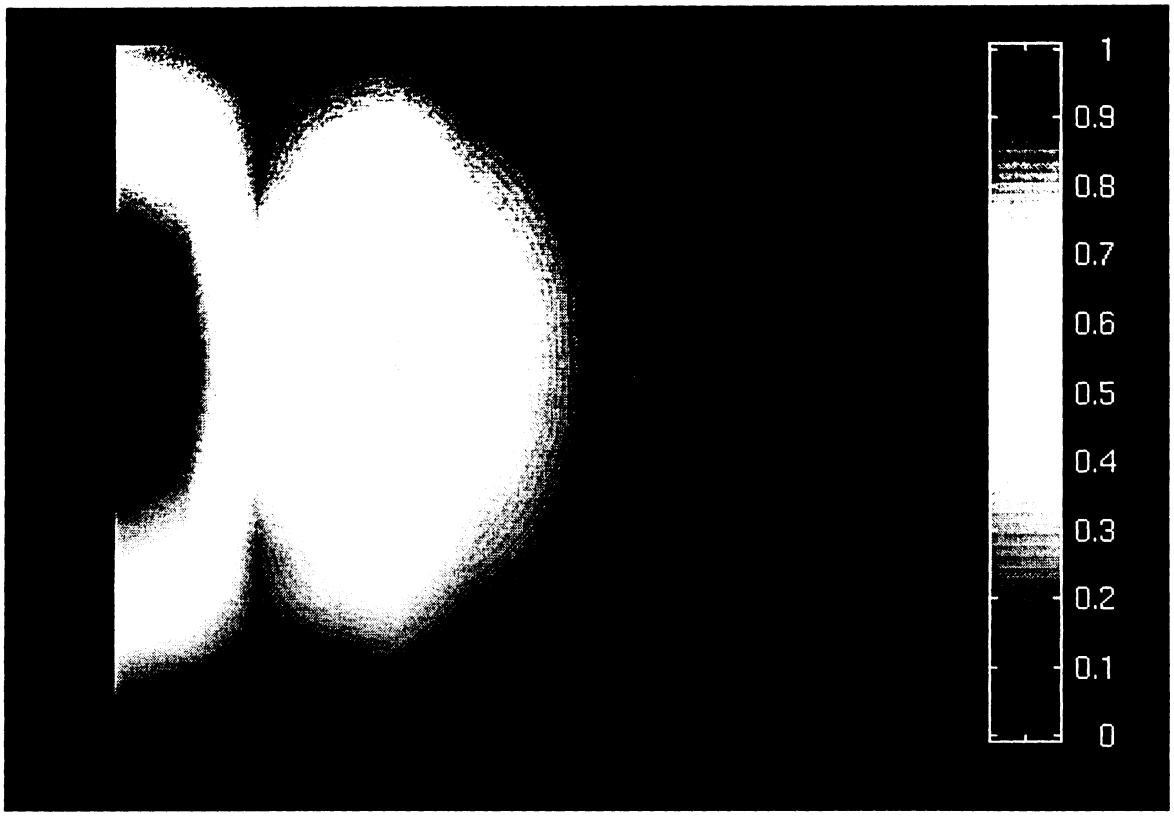

Figure 4: S–MRTD field pattern for quarter dielectric, not interpolated

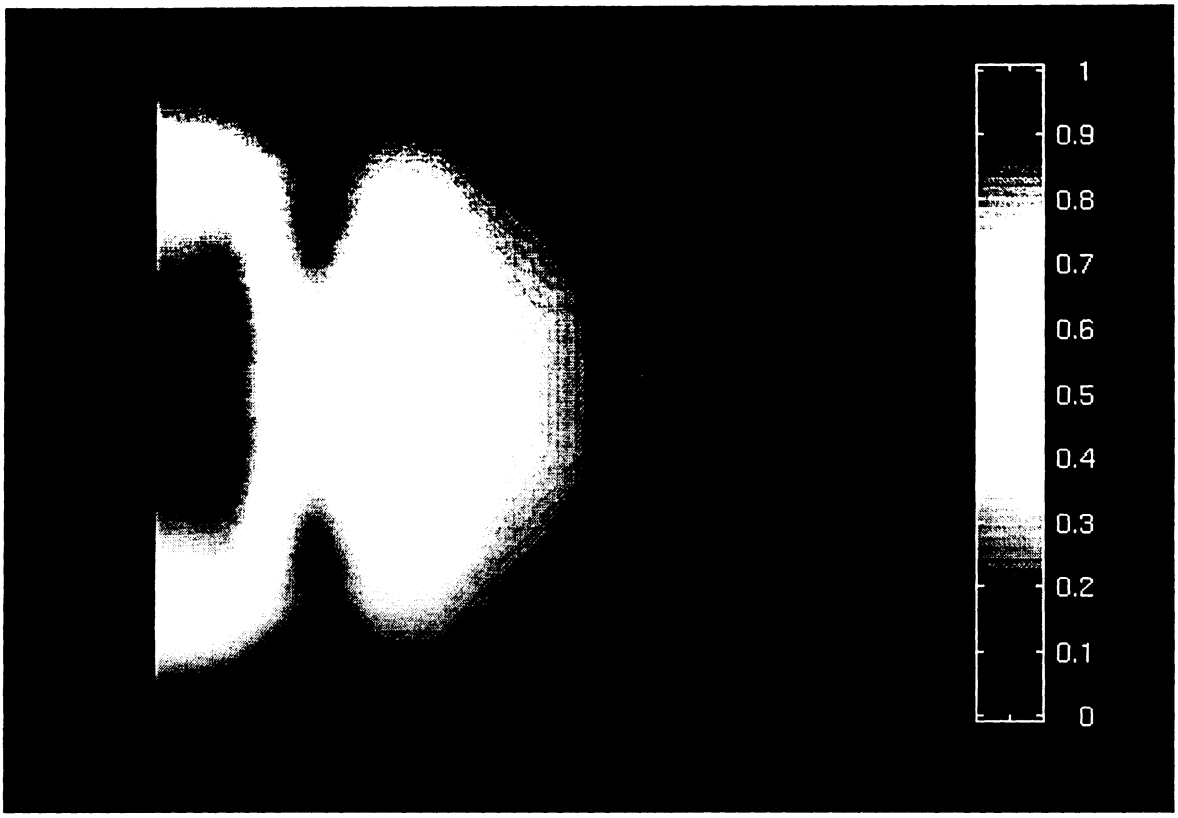

Figure 5: S–MRTD field pattern for quarter dielectric, interpolated

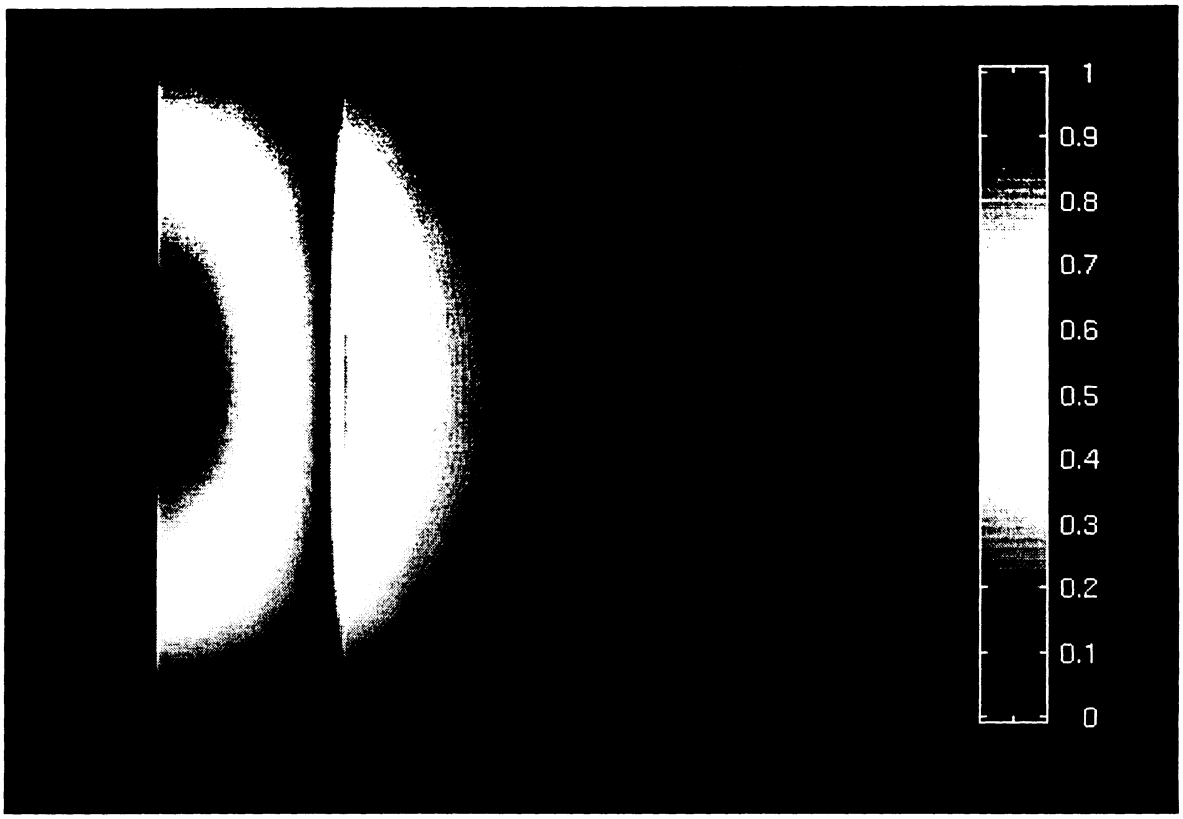

Figure 6: FDTD field pattern for quarter dielectric

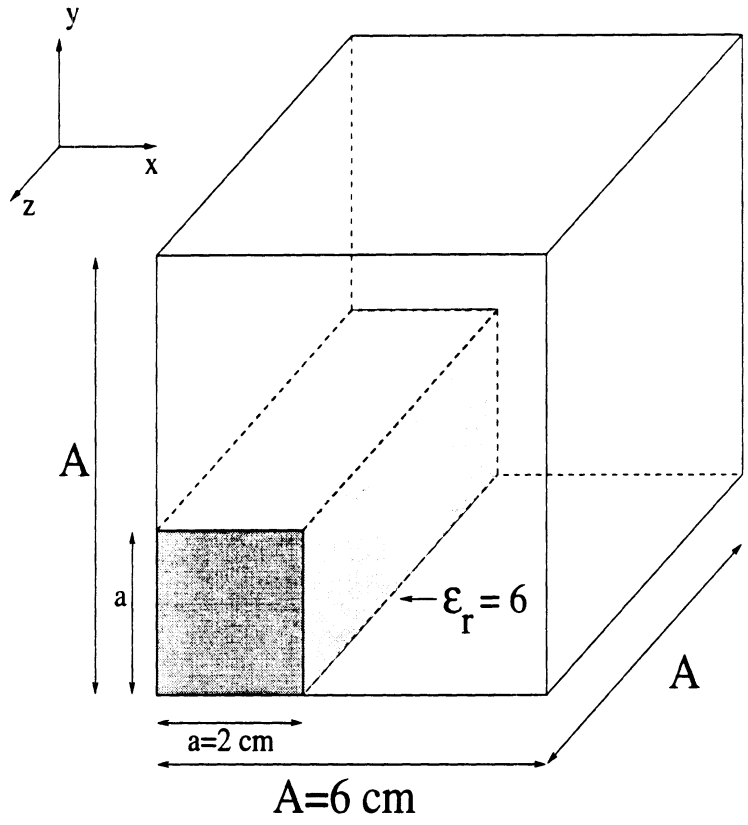

Figure 7: 2d dielectric structure

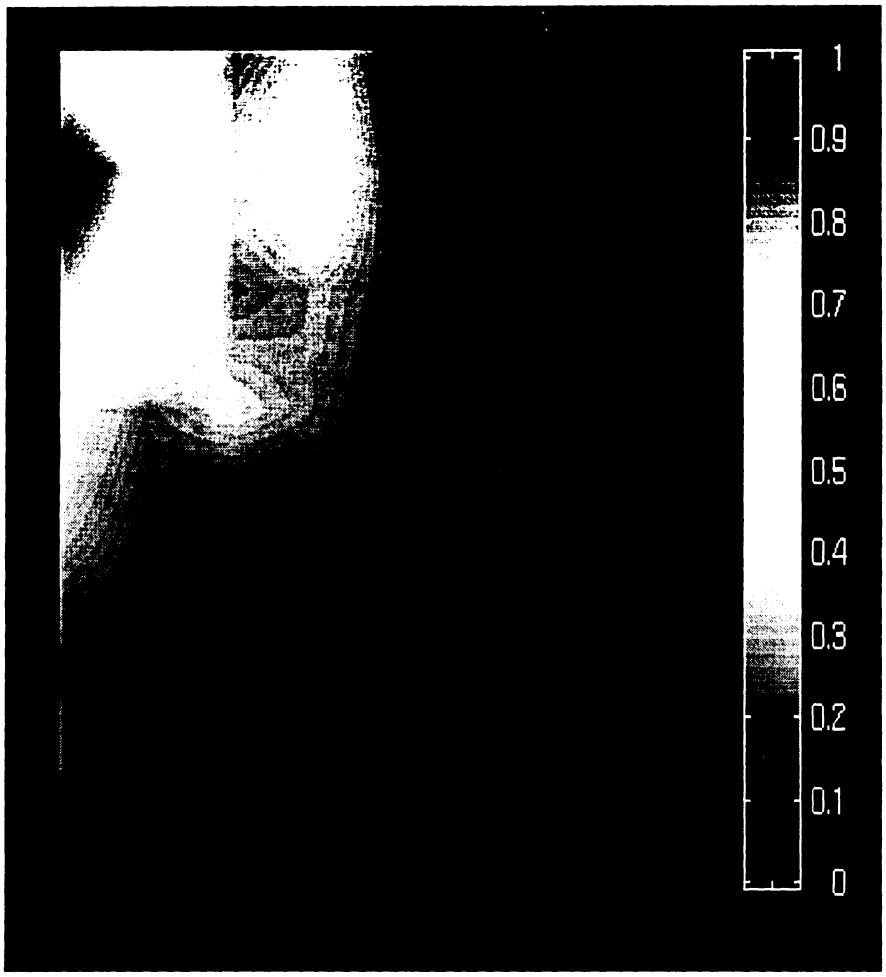

Figure 8: MRTD field pattern for 2D dielectric structure

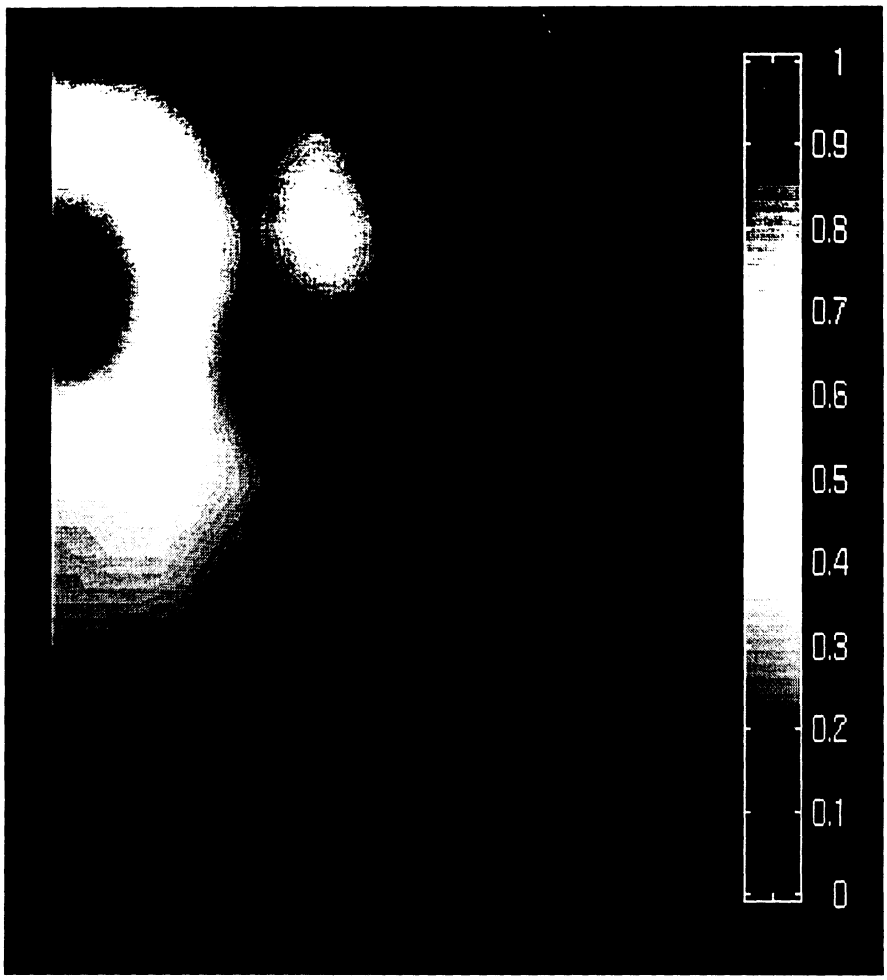

Figure 9: MRTD interpolated field pattern for 2D dielectric structure

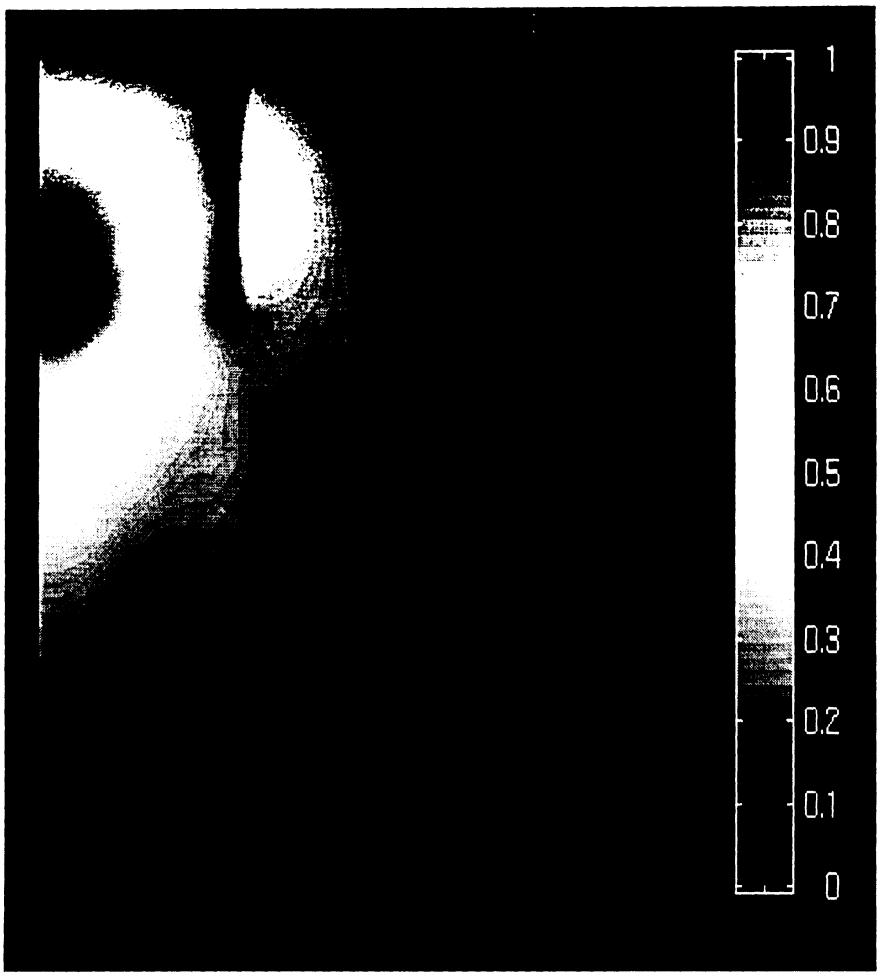

Figure 10: FDTD field pattern for 2D dielectric structure

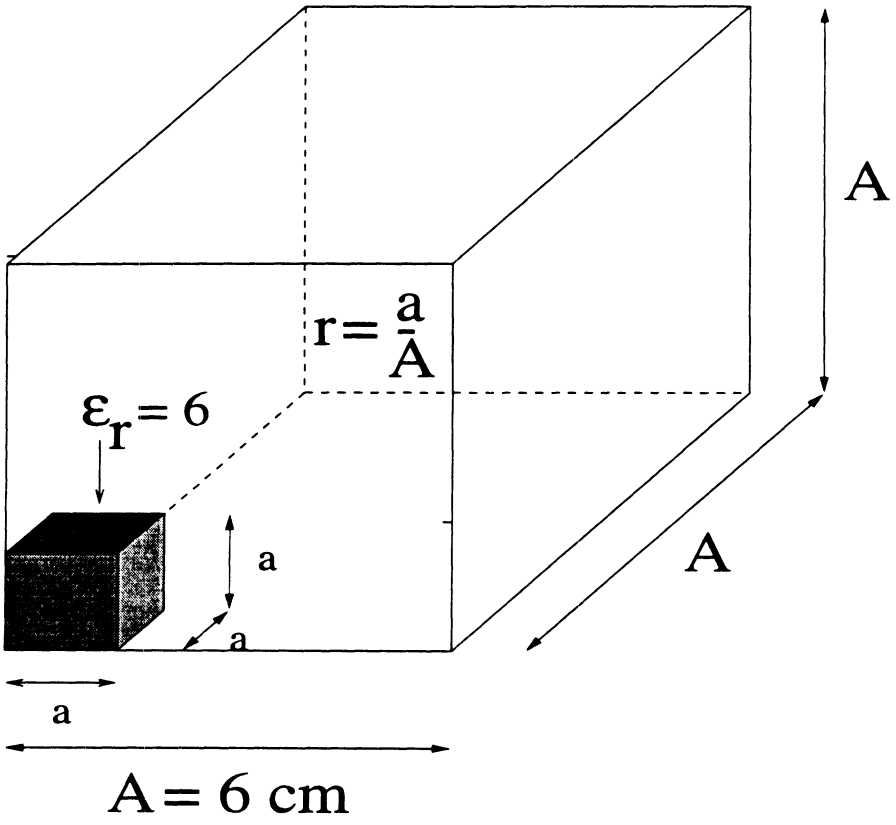

Figure 11: 3d resonator structure with varying dielectric in corner

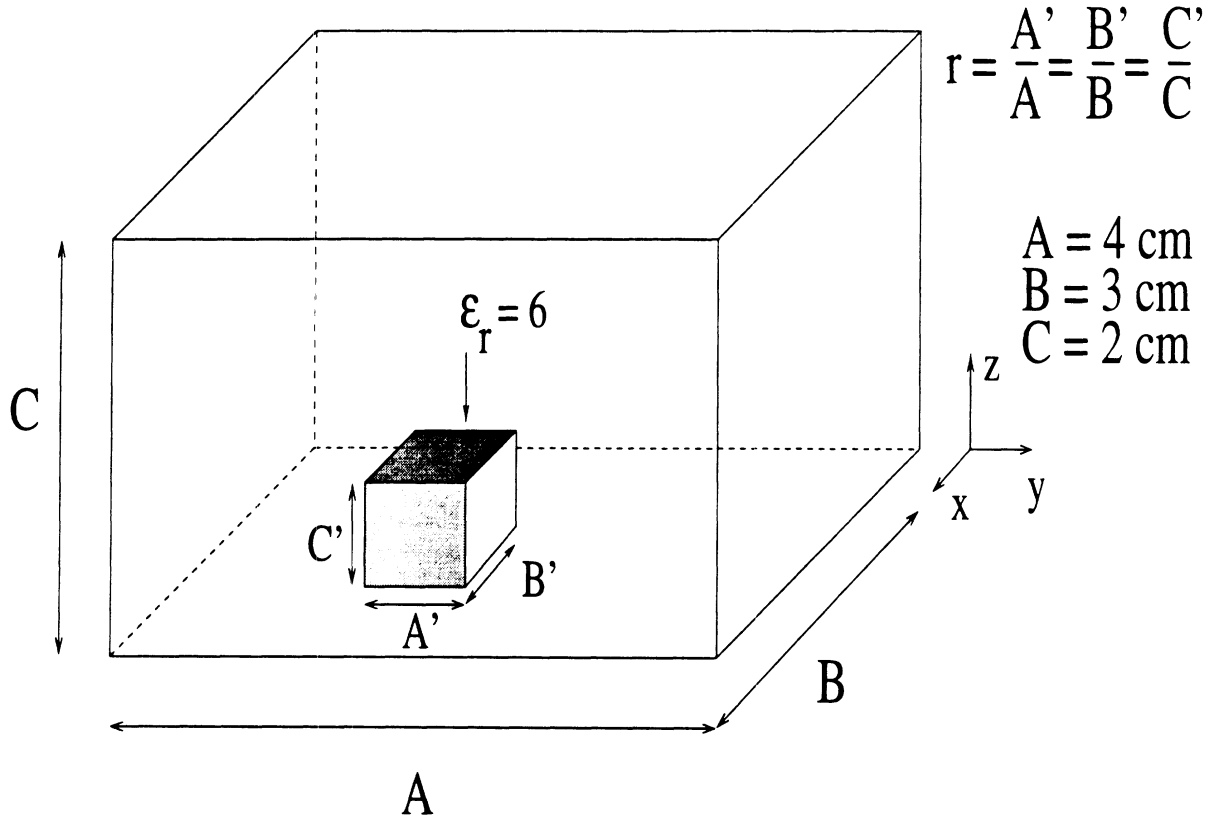

Figure 12: 3d resonator structure with varying dielectric in center

To be submitted to the IEEE Transactions on MTT

STABILITY AND DISPERSION ANALYSIS OF BATTLE-LEMARIE BASED MRTD SCHEMES

Emmanouil M. Tentzeris, Robert L. Robertson, Linda P.B. Katehi
Radiation Laboratory, Department of Electrical Engineering and Computer Science
University of Michigan, Ann Arbor, MI 48109-2122

I Abstract

The stability and the dispersion performance of the recently developed Battle-Lemarie MRTD schemes is investigated for different stencil sizes. The contribution of wavelets is enhanced and analytical expressions for the maximum allowable time step are derived. It is observed that larger stencils decrease the numerical phase error making it significantly lower than FDTD for low and medium discretizations. The addition of wavelets further improves the dispersion performance for discretizations close to the Nyquist limit, though it decreases the value of the maximum time-step guaranteeing the stability of the scheme.

II Introduction

Finite-Difference Time-Domain numerical techniques are widely used now-a-days for the analysis of various microwave geometries and for the modelling of EM wave propagation. Though many of them are very simple to implement and can be easily applied to different topologies with remarkable accuracy, they cause a numerical phase error during the propagation along the discretized grid. For example, the numerical phase velocity in the FDTD can be different than the velocity of light, depending on the cell size as a fraction of the smallest propagating wavelength and the direction of the grid propagation. Thus, a non-physical dispersion is introduced and affects the accuracy limits of FDTD simulations, especially of large structures.

In addition, it is well-known that the finite-difference schemes in time and space domain require that the used time step should take values within an interval that is a function of the cell size. If the time-step takes a value outside the bounds of this interval, the algorithm will be numerically unstable, leading to a spurious increase of the field values without limit as the time increases.

Though the stability and the dispersion analysis for the conventional Yee's FDTD algorithm has been thoroughly investigated, only a few results have been presented concerning MRTD schemes based on cubic spline Battle-Lemarie scaling and wavelet functions [2]. The functions of this family do not have compact support, thus the finite approximations of the derivatives are finite stencil summations instead of finite differences. In this paper, the effect of these stencils' size as well as of the enhancement of wavelets is investigated and comparison with 2nd-order and higher-order FDTD schemes displays difference in their respective behaviors.

III Stability Analysis

Following the stability analysis described in [1], the MRTD [2] equations are decomposed into separate time and space eigenvalue problems. Assuming an expansion only to scaling functions (S-MRTD), the left-hand side

time-differentiation parts can be written as an eigenvalue problem

$$\frac{{}^{k+1/2}H^x_{i,j-1/2} - {}^{k-1/2}H^x_{i,j-1/2}}{\Delta t} = \Lambda\ {}_kH^x_{i,j-1/2} \quad (1)$$

$$\frac{{}^{k+1/2}H^y_{i-1/2,j} - {}^{k-1/2}H^y_{i-1/2,j}}{\Delta t} = \Lambda\ {}_kH^y_{i,j-1/2} \quad (2)$$

$$\frac{{}^{k+1}E^z_{i,j} - {}_kE^z_{i,j}}{\Delta t} = \Lambda\ {}_{k+1/2}E^z_{i,j} \quad . \quad (3)$$

In order to avoid having any spatial mode increasing without limit during normal time-stepping, the imaginary part of Λ, $Imag(\Lambda)$, m ust satisfy the equation

$$-\frac{2}{\Delta t} \leq Imag(\Lambda) \leq \frac{2}{\Delta t} \quad . \quad (4)$$

For each time step k, the instantaneous values of the electric and magnetic fields distributed in space across the grid can be Fourier-transformed with respect to the i- and j- coordinates to provide a spectrum of sinusoidal modes (plane wave eigenmodes of the grid). Assuming an eigenmode of the spatial-frequency domain with k_x and k_y being the x- and y- components of the numerical eigenvector, the field components can be written

$$\begin{aligned} E^z_{I,J} &= E_{z_o}e^{j(k_xI\Delta x + k_yJ\Delta y} \\ H^x_{I,J-1/2} &= H_{x_o}e^{j(k_xI\Delta x + k_y(J-1/2)\Delta y} \\ H^y_{I-1/2,J} &= H_{y_o}e^{j(k_x(I-1/2)\Delta x + k_yJ\Delta y} \quad . \end{aligned}$$

Substituting these expressions to (1)–(3) and applying Euler's identity, we get

$$\Lambda^2 = -\frac{4}{\mu\epsilon}[\frac{1}{(\Delta x)^2}(\sum_{i'=0}^{n_a-1} a(i')sin(k_x(i+1/2)\Delta x))^2 + \frac{1}{(\Delta y)^2}(\sum_{j'=0}^{n_a-1} a(j')sin(k_y(j+1/2)\Delta y))^2] \quad .$$

Thus, Λ is a pure imaginary, which can be bounded for any wavevector $k = (k_x, k_y)$:

$$\begin{aligned} -\ 2c\ &(\sum_{i'=0}^{n_a-1} |a(i')|)\ \sqrt{\frac{1}{(\Delta x)^2} + \frac{1}{(\Delta y)^2}} \leq Imag(\Lambda) \\ \leq\ 2c\ &(\sum_{i'=0}^{n_a-1} |a(i')|)\ \sqrt{\frac{1}{(\Delta x)^2} + \frac{1}{(\Delta y)^2}} \quad , \end{aligned} \quad (5)$$

where $c = \frac{1}{\sqrt{\mu\epsilon}}$ is the velocity of the light in the modeled medium.

Numerical stability is maintained for every spatial mode only when the range of eigenvalues given by (5) is contained entirely within the stable range of time-differentiation eigenvalues given by (4). Since both ranges are symmetrical around zero, it is adequate to set the upper bound of (5) to be smaller or equal to (4), giving:

$$\Delta t \leq \frac{1}{c\ (\sum_{i'=0}^{n_a-1} |a(i')|)\ \sqrt{\frac{1}{(\Delta x)^2} + \frac{1}{(\Delta y)^2}}} \quad . \quad (6)$$

For $\Delta x = \Delta y = \Delta$, the above stability criterion gives

$$\Delta t_{S-MRTD} \leq \frac{\Delta}{c\sqrt{2}\sum_{i'=0}^{n_a-1} |a(i')|} = s_{SS}\frac{\Delta}{c\sqrt{2}} \quad . \quad (7)$$

It is known [3] that

$$\Delta t_{FDTD} \leq \frac{1}{c\sqrt{\frac{1}{(\Delta x)^2} + \frac{1}{(\Delta y)^2}}} \quad , \quad (8)$$

which gives for $\Delta x = \Delta y = \Delta$

$$\Delta t_{FDTD} \leq \frac{\Delta}{c\sqrt{2}} \quad . \tag{9}$$

Equations (7)-(9) show that for same discretization size, the upper bounds of the time-steps of FDTD and S-MRTD are comparable and related through the factor s. The stability analysis can be generalized easily to 3D. The new stability criteria can be derived by the equations (7) and (9) by substituting the term $\sqrt{2}$ with $\sqrt{3}$.

More complicated expressions can be derived for the maximum allowable time-step for schemes containing scaling and wavelet functions. For example, the upper bound of the time-step for the 2D MRTD scheme with 0-resolution wavelets to the one (x-direction) or two directions (x- and y-directions) is given by

$$\Delta t_{W_0S-MRTD} \leq \frac{1}{c\sqrt{\frac{1}{(\Delta x)^2}(\sum_{i'=0}^{n_a-1}|a(i')|\sum_{i'=0}^{n_b-1}|b_0(i')| + 4(\sum_{i'=0}^{n_c-1}|c_0(i')|)^2) + \frac{1}{(\Delta y)^2}(\sum_{j'=0}^{n_a-1}|a(j')|)^2}}$$

and

$$\Delta t_{W_0W_0-MRTD} \leq \frac{1}{c\sqrt{\frac{1}{(\Delta x)^2}+\frac{1}{(\Delta y)^2)}}\sqrt{\sum_{i'=0}^{n_a-1}|a(i')|\sum_{i'=0}^{n_b-1}|b_0(i')| + 4(\sum_{i'=0}^{n_c-1}|c_0(i')|)^2}}$$

For Δx=Δy=Δ, the above equations give

$$\Delta t_{W_0S-MRTD,max} \approx s_{W_0S}\frac{\Delta}{c\sqrt{2}}$$

with

$$s_{W_0S} = \frac{\sqrt{2}}{\sqrt{(\sum_{i'=0}^{n_a-1}|a(i')|\sum_{i'=0}^{n_b-1}|b_0(i')| + 4(\sum_{i'=0}^{n_c-1}|c_0(i')|)^2) + (\sum_{j'=0}^{n_a-1}|a(j')|)^2}}$$

and

$$\Delta t_{W_0W_0-MRTD,max} \approx s_{W_0W_0}\frac{\Delta}{c\sqrt{2}}$$

with

$$s_{W_0W_0} = \sqrt{\sum_{i'=0}^{n_a-1}|a(i')|\sum_{i'=0}^{n_b-1}|b_0(i')| + 4(\sum_{i'=0}^{n_c-1}|c_0(i')|)^2}$$

It can be observed that the upper bound of the time step depends on the stencil size n_a, n_b, n_c. This dependence is expressed through the coefficients $s_{SS}, s_{W_0S}, s_{W_0W_0}$, which decrease as the stencil size increases. Figure 1 shows that s_{SS} practically converges to the value 0.6371 after $n_a \geq 10$ and $s_{W_0S} \approx 0.4872$ and $s_{W_0W_0} \approx 0.4095$ for $n_a = n_b = n_c \geq 10$.

IV Dispersion Analysis

To calculate the numerical dispersion of the S-MRTD scheme, plane monochromatic traveling-wave trial solutions are substituted in the discretized Maxwell's equations. For example, the E_z component for the TM mode has the form

$${}_kE^z_{I,J} = E_{z_o}e^{j(k_xI\Delta x + k_yJ\Delta y - \omega k\Delta t)} \quad ,$$

where k_x and k_y are the x- and y- components of the numerical wavevector and ω is the wave angular frequency. Substituting the above expressions into the Equations (1)-(3), the following numerical dispersion relation is obtained for the TM mode for the S-MRTD Scheme after algebraic manipulation

$$\begin{aligned}[\frac{1}{c\Delta t}sin(\frac{\omega\Delta t}{2})]^2 &= [\frac{1}{\Delta x}(\sum_{i'=0}^{n_a-1} a(i')sin(k_x(i+1/2)\Delta x))]^2 \\ &+ [\frac{1}{\Delta y}(\sum_{j'=0}^{n_a-1} a(j')sin(k_y(j+1/2)\Delta y))]^2 \end{aligned} \quad (10)$$

For square unit cells (Δx=Δy=Δ) and wave propagating at an angle ϕ with respect to x-axis ($k_x = k\ cos\phi$ and $k_y = k\ sin\phi$), the above expression is simplified to

$$\begin{aligned}[\frac{\Delta}{c\Delta t}\ sin(\frac{\omega\ \Delta t}{2})]^2 &= (\sum_{i'=0}^{n_a-1} a(i')\ sin(k\ cos\phi\ (i'+1/2)\ \Delta))^2 \\ &+ (\sum_{j'=0}^{n_a-1} a(j')\ sin(k\ sin\phi\ (j'+1/2)\ \Delta))^2 \end{aligned} \quad (11)$$

This equation relates the numerical wavevector, the wave frequency, the cell size and the time-step. Solving this numerically for different angles, time step sizes and frequencies, the dispersion characteristics can be quantified.

Defining the Courant number $q = (c\Delta t)/\Delta$ and the number of cells per wavelength $n_l = \lambda_{REAL}/\Delta$ and using the definition of the wavevector $k = (2\pi)/\lambda_{NUM}$ the dispersion relationship can be written as

$$\begin{aligned}[\frac{1}{q}\ sin(\pi\ q\ /n_l)]^2 &= [\sum_{i'=0}^{n_a-1} a(i')\ sin(\pi\ u\ (2i'+1)\ cos\phi\ /n_l)]^2 \\ &+ [\sum_{j'=0}^{n_a-1} a(j')\ sin(\pi\ u\ (2j'+1)\ sin\phi\ /n_l)]^2 \end{aligned} \quad (12)$$

where $u = \lambda_{REAL}/\lambda_{NUM}$ is the ratio of the theoretically give n to the numerical value of the propagating wavelength and expresses the phase error introduced by the S-MRTD algorithm. To satisfy the stability requirements, q has to be smaller than 0.45 ($= 0.6371/\sqrt{2}$) for the 2D simu lations.

The above analysis can be extended to cover the expansion in scaling and 0-resolution wavelet functions in x-, y- or both directions.

The general dispersion relationship is

$$\begin{aligned}\frac{\mu}{\epsilon}(C_1C_1 + C_2C_2 + C_4C_4 + C_5C_5) + (\frac{\mu}{\epsilon})^2[\frac{(C_4C_5 + C_5C_6)^2}{A} &+ \frac{(C_1C_2 + C_2C_3)^2}{B}] \\ +(\frac{\mu}{\epsilon})^4(C_1C_2 + C_2C_3)^2(C_4C_5 + C_5C_6)^2(\frac{1}{A} + \frac{1}{B})^2\frac{1}{F} &= 1 \end{aligned} \quad (13)$$

with

$$\begin{aligned}F = 1 &- [\frac{\mu}{\epsilon}(C_1C_2 + C_2C_3)]^2\frac{1}{A} - [\frac{\mu}{\epsilon}(C_4C_5 + C_5C_6)]^2\frac{1}{B} \\ &- [\frac{\mu}{\epsilon}(C_2C_2 + C_3C_3 + C_5C_5 + C_6C_6] \end{aligned} \quad (14)$$

Scheme	C_1	C_2	C_3	C_4	C_5	C_6
SS	$\neq 0$	0	0	$\neq 0$	0	0
W_0S	$\neq 0$	0	0	$\neq 0$	$\neq 0$	$\neq 0$
SW_0	$\neq 0$	$\neq 0$	$\neq 0$	$\neq 0$	0	0
W_0W_0	$\neq 0$	$\neq 0$	$\neq 0$	$\neq 0$	$\neq 0$	$\neq 0$

Table 1: Coefficients C_i for Different MRTD Schemes

$$\begin{aligned} A &= 1 - \frac{\mu}{\epsilon}(C_1C_1 + C_2C_2 + C_5C_5 + C_6C_6) \\ B &= 1 - \frac{\mu}{\epsilon}(C_2C_2 + C_3C_3 + C_4C_4 + C_5C_5) \end{aligned} \tag{15}$$

. The C_i are defined by

$$\begin{aligned} C_1 &= -\frac{\Delta t}{\mu\Delta sin(\omega\Delta t/2)} \sum_{j'=0}^{n_a} a(j')sin(k_y(j'+1/2)\Delta) \\ C_2 &= -\frac{\Delta t}{\mu\Delta sin(\omega\Delta t/2)} \sum_{j'=0}^{n_c} c_0(j')sin(k_y j'\Delta) \\ C_3 &= -\frac{\Delta t}{\mu\Delta sin(\omega\Delta t/2)} \sum_{j'=0}^{n_b} b_0(j')sin(k_y(j'+1/2)\Delta) \\ C_4 &= -\frac{\Delta t}{\mu\Delta sin(\omega\Delta t/2)} \sum_{i'=0}^{n_a} a(i')sin(k_x(i'+1/2)\Delta) \\ C_2 &= -\frac{\Delta t}{\mu\Delta sin(\omega\Delta t/2)} \sum_{i'=0}^{n_c} c_0(i')sin(k_x i'\Delta) \\ C_3 &= -\frac{\Delta t}{\mu\Delta sin(\omega\Delta t/2)} \sum_{i'=0}^{n_b} b_0(i')sin(k_x(i'+1/2)\Delta) \end{aligned} \tag{16}$$

Eq.(13) can be applied to the dispersion analysis of SS (only scaling functions), W_0S (0-resolution wavelets only to x-direction), SW_0 (0-resolution wavelets only to y-direction) and W_0W_0 (0-resolution wavelets to both x- and y- directions) following Table 2. In case the $C_i \neq 0$, it can be calculated by Eq.(16).

The above equation is solved numerically by use of Bisection-Newton-Raphson Hybrid Technique for different values of n_a, n_b, n_c n_l, ϕ and q. Fig.(2)-(5) show the variation of the numerical phase velocity as a function of the inverse of the Courant number 1/s=1/q for stencil sizes $n_a = n_b = n_c = 8, 10, 12, 14$. For each figure, three different discretization sizes are used: 10 cells/wavelength (coarse), 20 cells/wavelength (normal) and 40 cells/wavelength (dense). The results are compared to the respective values of conventional FDTD. It can be observed that the phase error for F.D.T.D. decreases quadratically. The variation of the phase error in M.R.T.D. exhibits some unique features. Though for any stencil size the numerical phase error for M.R.T.D. discretization of $10 cells/\lambda$ is smaller than that of the F.D.T.D. discretization of $40 cells/\lambda$, the M.R.T.D. error doesn't behave monotonically [4]. It decreases up to a certain discretization value and then it starts increasing. This value depends on the stencil size and takes larger values for larger stencils. For example, this value is between 10 and 20 $cells/\lambda$ for stencil equal to 10, between 20 and 40 $cells/\lambda$ for stencil=12 and very close to 40 $cells/\lambda$ for stencil=14 and can be used as a criterion to characterize the discretization range that the M.R.T.D. offers significantly better numerical phase performance than the F.D.T.D.

The phase error caused by the dispersion is cumulative and it represents a limitation of the conventional FDTD Yee algorithm for the simulation of electrically large structures. It can be observed that the error of S-MRTD

is significantly lower, allowing the modeling of larger structures. FDTD is derived be expanding the fields in pulse basis. As it is well known the Fourier transform of the pulse is a highly oscillating Si(x). On the contrary, the Fourier transform of the Battle-Lemarie Cubic spline is similar to a low-pass filter. That "smooth" spectral characteristic offers a much lower phase error even for very coarse (close to 3-4 cells/λ) cells.

By using a larger stencil n_a, the entire-domain oscillating nature of the scaling functions is better represented. Thus, smoother performance for low discretizations (Fig.(6)) and lower phase error for higher discretizations (Fig.(7)) is achieved as n_a increases from 8 to 12. Wavelets contribute to the improvement of the dispersion characteristics for even coarser cells (close to 2.2-2.4 cells/λ) as it is demonstrated in Fig.(8)-(13). For discretizations above 4 cells/λ the effect of the wavelets is negligible. (Fig.(11)) and (Fig.(13)) show clearly that the phase error has a minimum for a specific discretization (17 for $n_a = 10$ and 25 for $n_a = 12$).

Fig.(14)-(17) show that for discretizations smaller than $30 cells/\lambda$ the choice of the Courant number affects significantly the dispersion performance which starts converging to the minimum numerical phase error (0.8 deg/λ for $n_a = n_b = n_c = 10$ and 0.2 deg/λ for $n_a = n_b = n_c = 12$) for 1/q close to 10. On the contrary, the F.D.T.D. dispersion is almost independent of the Courant number (Fig.(18)-(19)).

It has been claimed in [5] that the S-MRTD Scheme is slightly oscillating and its performance is only comparable with the 14^{th} order accuracy Yee's scheme. Though this is true for the S-MRTD schemes with stencil size of 8, the comparison of the dispersion diagrams of Yee's FDTD scheme, Yee's 16th order (H.F.D.-16) and 22th order (H.F.D.-22) and S-MRTD and Wo-MRTD schemes with different stencils leads to interesting results. For comparison purposes, the values of $\Delta t = \Delta t_{max}/5$ and $\Delta t_{max} = 0.368112\Delta l/c$ have been used and all the dispersion curves are substracted by the linear dispersion relation for 1D simulations. Fig.(20) shows that the S-MRTD scheme with stencil 10 has a comparable performance to the 16th order Yee's scheme. The enhancement of the wavelets for the same stencil improves significantly the dispersion characteristics of the MRTD scheme increasing the dynamic range of ω by approximately 90% and comparing favorable even to the 22th order Yee's scheme. This is expected due to the fact that the scaling+wavelet basis spans a larger ("more complete") subspace of R than the scaling functions alone. Both S-MRTD and Wo-MRTD schemes have identical numerical phase errors up to the point that the S-MRTD scheme starts diverging (Fig.(21)). As the stencil size of the Wo-MRTD scheme is increasing from 6 to 12 (Fig.(22)-(23)), the oscillatory variation of the phase error is diminishing to a negligible level generating an almost flat algorithm similar to the higher order Yee's ones.

As a conclusion, due to the poor dispersion performance of the FDTD technique even for 10 cells/wavelength a normal to coarse grid is always required to avoid significant pulse distortions especially for the higher-spatial-frequency components. MRTD offers low dispersion even for sparse grids very close to the Nyquist limit.

V Conlusion

The stability and the dispersion performance of the recently developed Battle-Lemarie MRTD schemes has been investigated for different stencil sizes and for 0-resolution wavelets. Analytical expressions for the maximum stable time-step have been derived. Larger stencils decrease the numerical phase error making it significantly lower than FDTD for low and medium discretizations. Stencil sizes greater than 10 offer a smaller phase error than FDTD even for discretizations close to 50 cells/wavelength. The enhancement of wavelets further improves the dispersion performance for discretizations close to the Nyquist limit (2-3 cells/wavelength) making it

comparable to that of much denser grids, though it decreases the value of the maximum time-step guaranteeing the stability of the scheme.

References

[1] A.Taflove, "Computational Electrodynamics", Artech House, 1995.

[2] M.Krumpholz, L.P.B.Katehi, "MRTD: New Time Domain Schemes Based on Multiresolution Analysis", IEEE Trans. Microwave Theory and Techniques, vol. 44, no. 4, pp. 555-561, Ap ril 1996.

[3] K.S.Yee, "Numerical solution of initial boundary value problems involving Maxwell's equations in isotropic media", IEEE Trans. Antennas Propagation, pp.302-307, May 1966.

[4] K.L.Shlager and J.B.Schneider, "Analysis of the Dispersion Properties of the Multiresolution Time-Domain Method", IEEE AP-S 1997 Proceedings, vol. 4, pp. 2144-2147, 1997.

[5] W.Y.Tam, "Comments on "New Prospects for Time Domain Analysis"", IEEE Microwave and Guided Wave Letters, vol. 6, pp. 422-423, 1996.

LIST OF FIGURE CAPTIONS

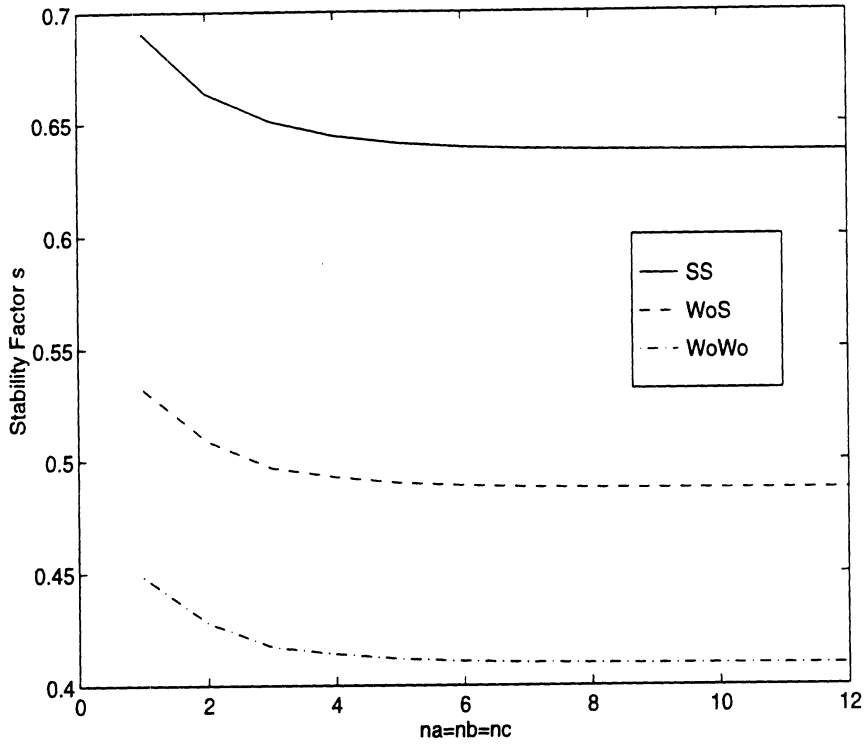

Figure 1: Stability Parameter s for MRTD.

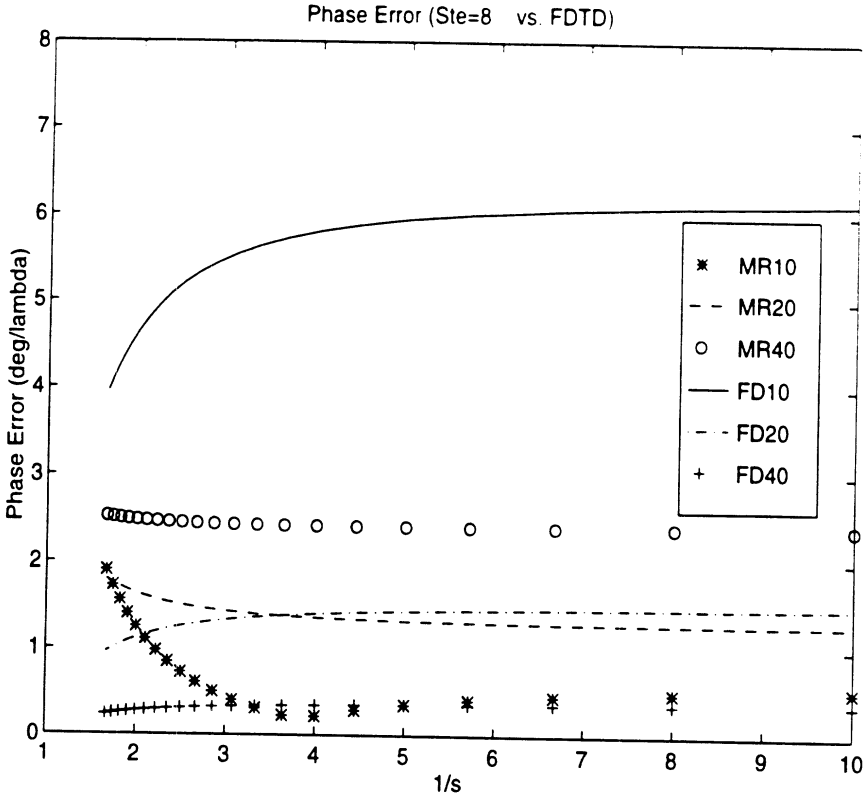

Figure 2: Dispersion Characteristics of S-MRTD for n_a=8.

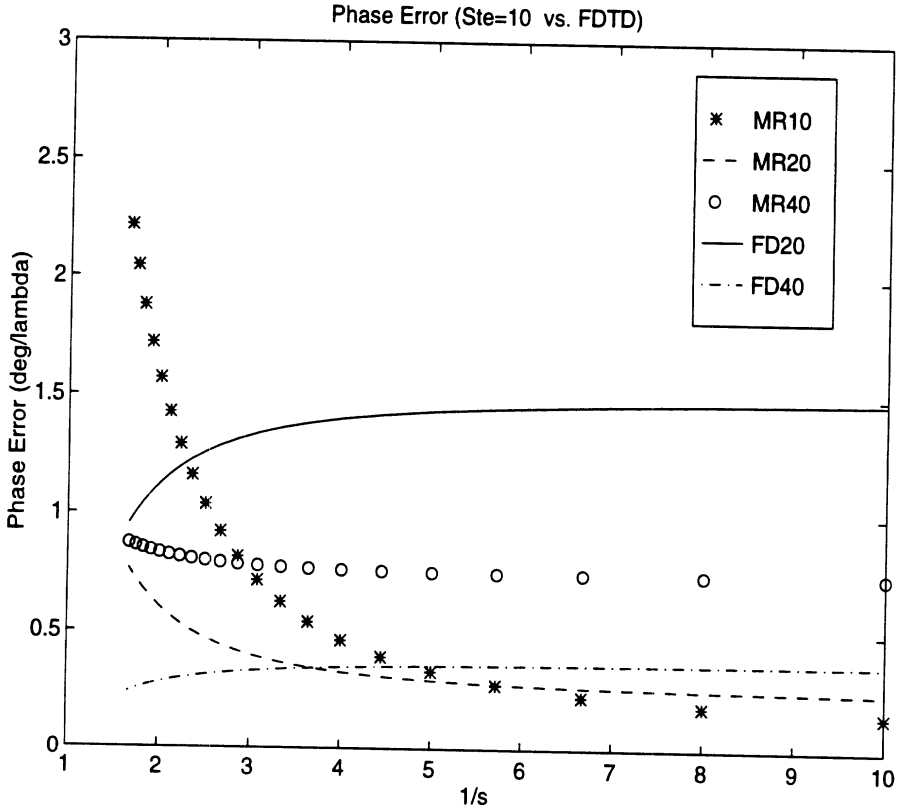

Figure 3: Dispersion Characteristics of S-MRTD for n_a=10.

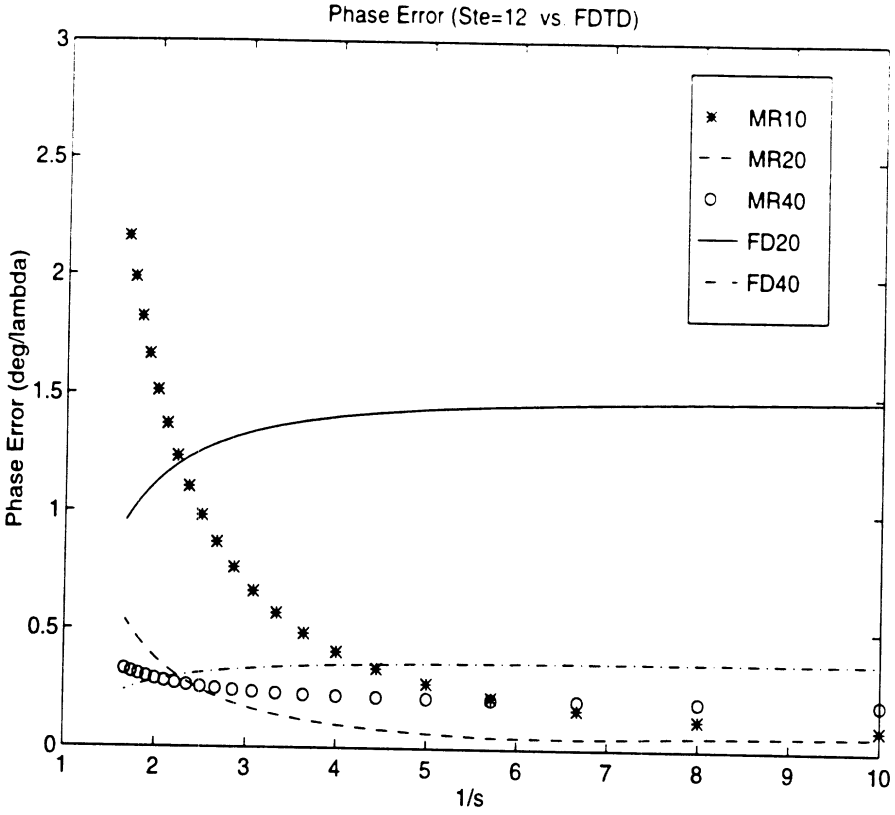

Figure 4: Dispersion Characteristics of S-MRTD for n_a=12.

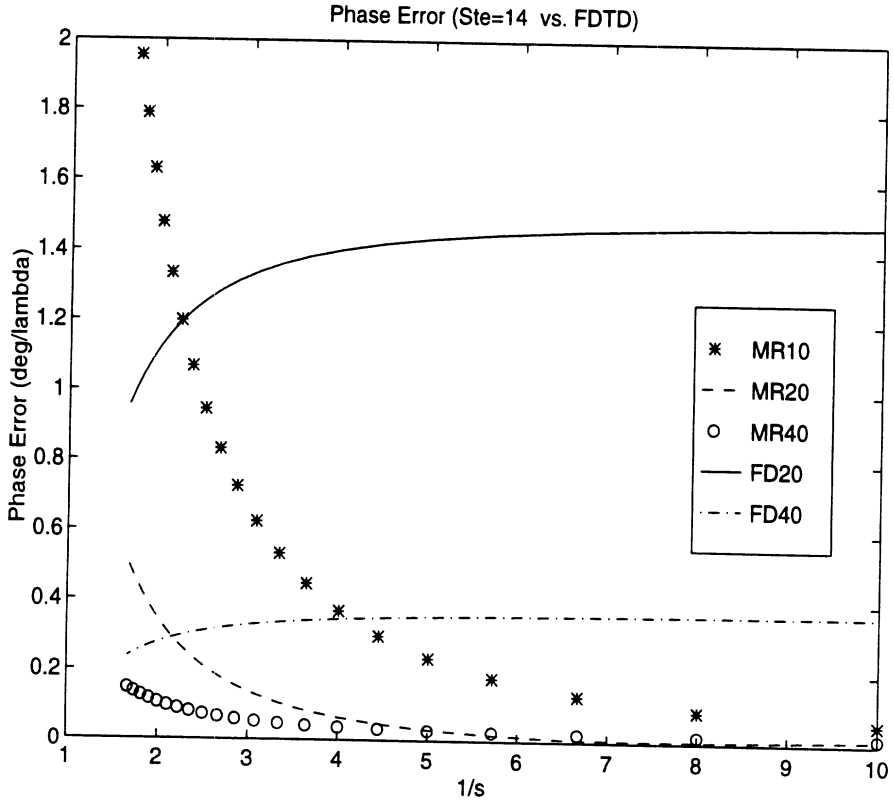

Figure 5: Dispersion Characteristics of S-MRTD for n_a=14.

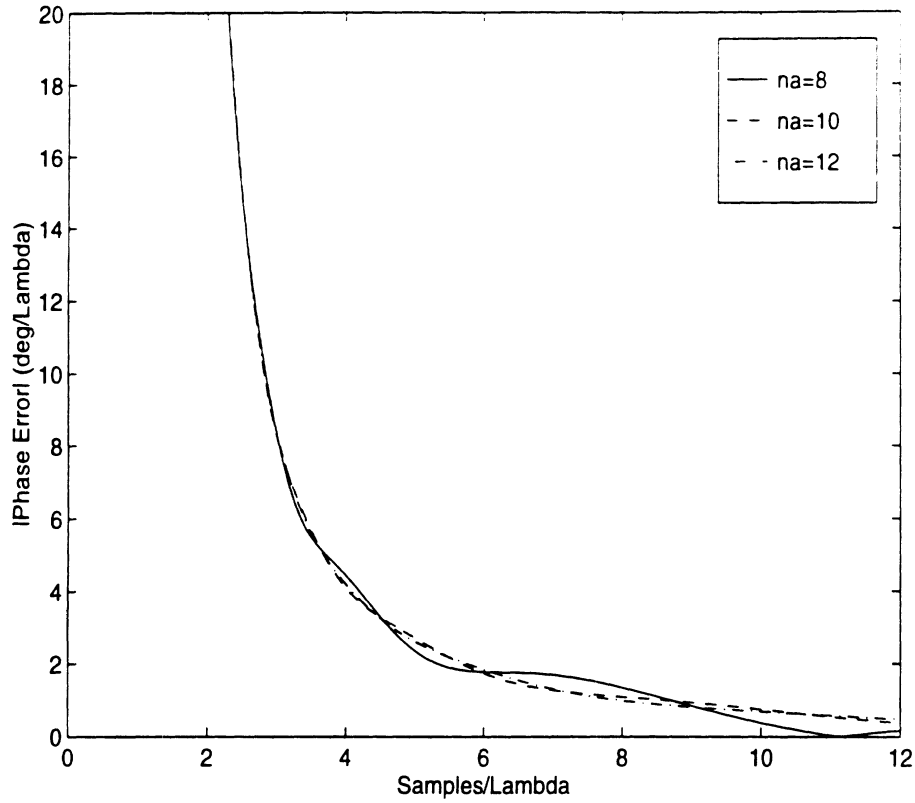

Figure 6: Stencil Effect on the Dispersion Characteristics of S-MRTD (Sparse Grid).

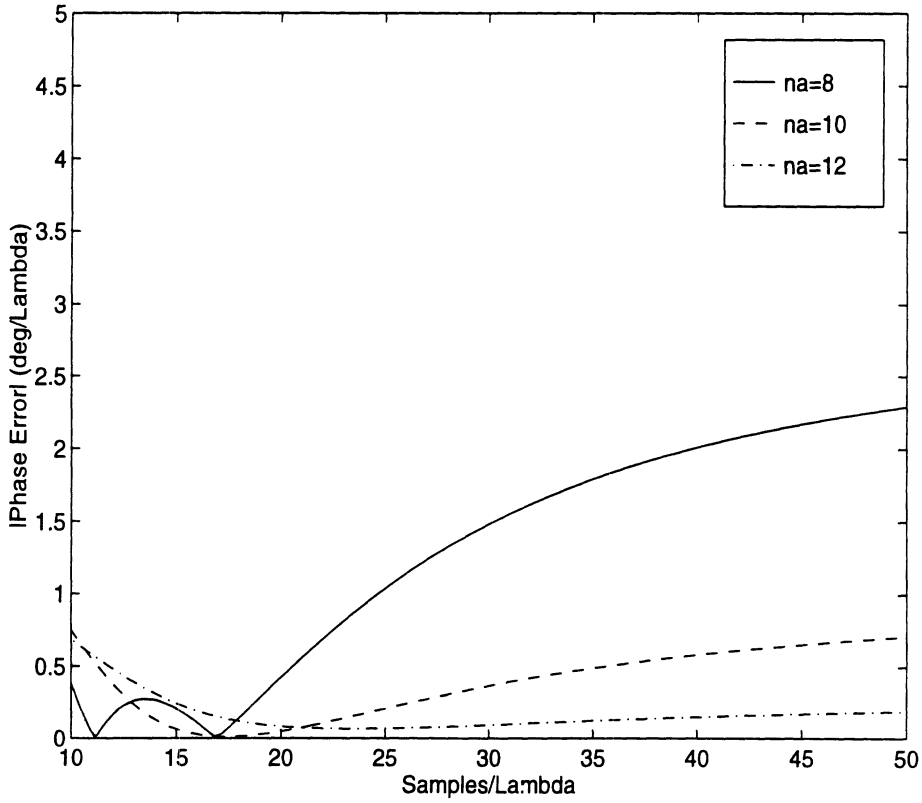

Figure 7: Stencil Effect on the Dispersion Characteristics of S-MRTD (Dense Grid).

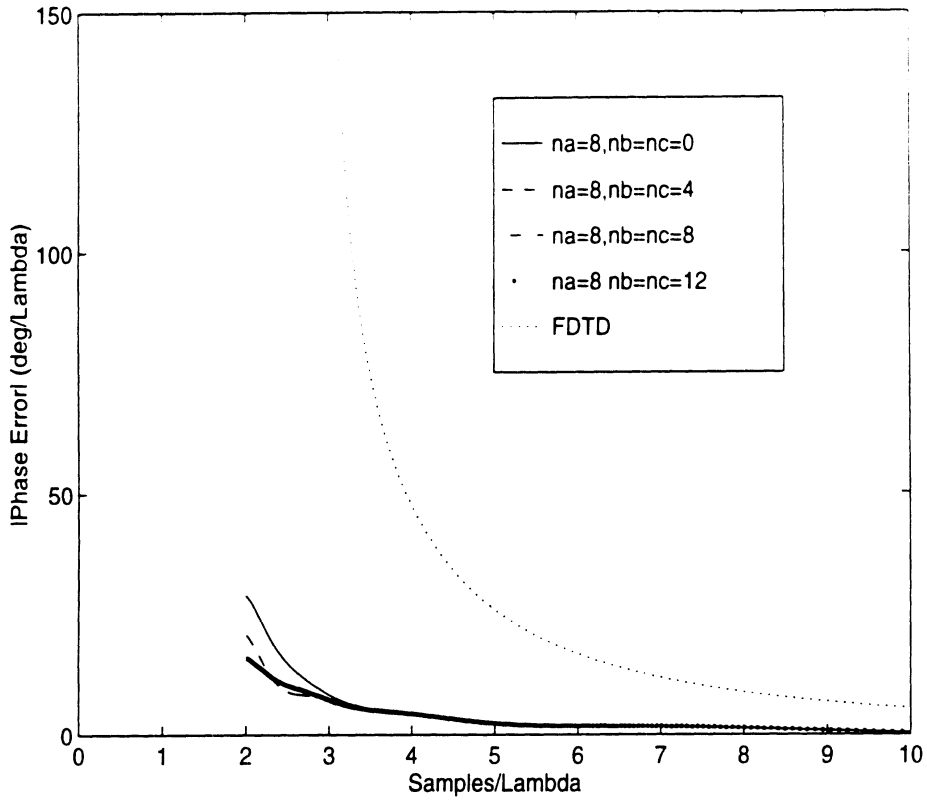

Figure 8: Wavelets Effect on the Dispersion Characteristics of MRTD for n_a=8 (Coarse Grid).

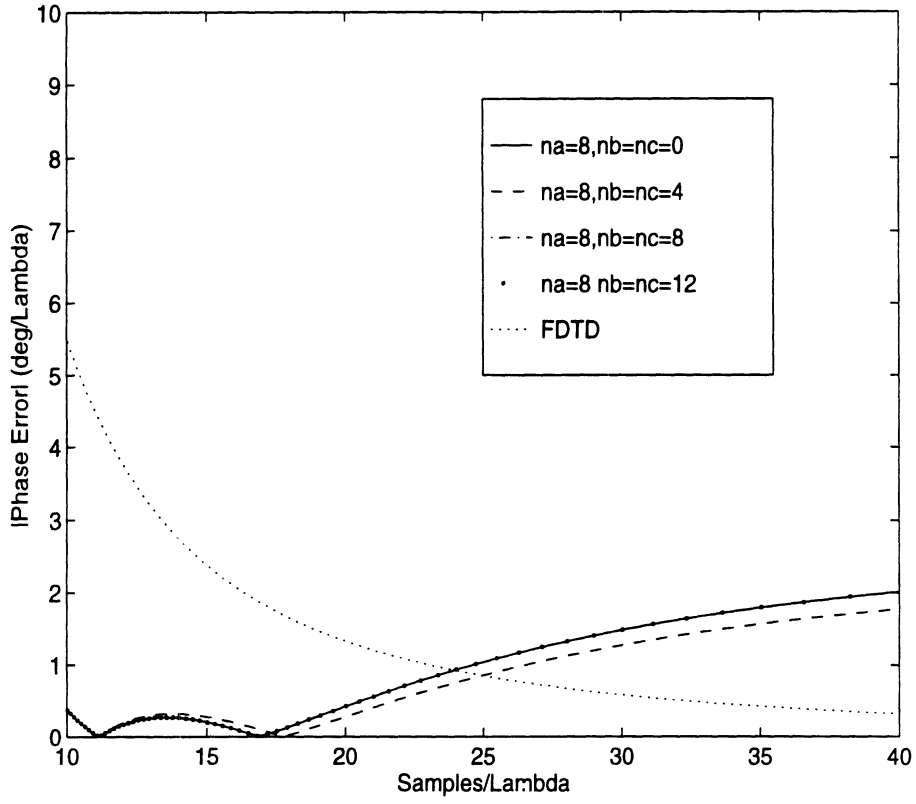

Figure 9: Wavelets Effect on the Dispersion Characteristics of MRTD for n_a=8 (Denser Grid).

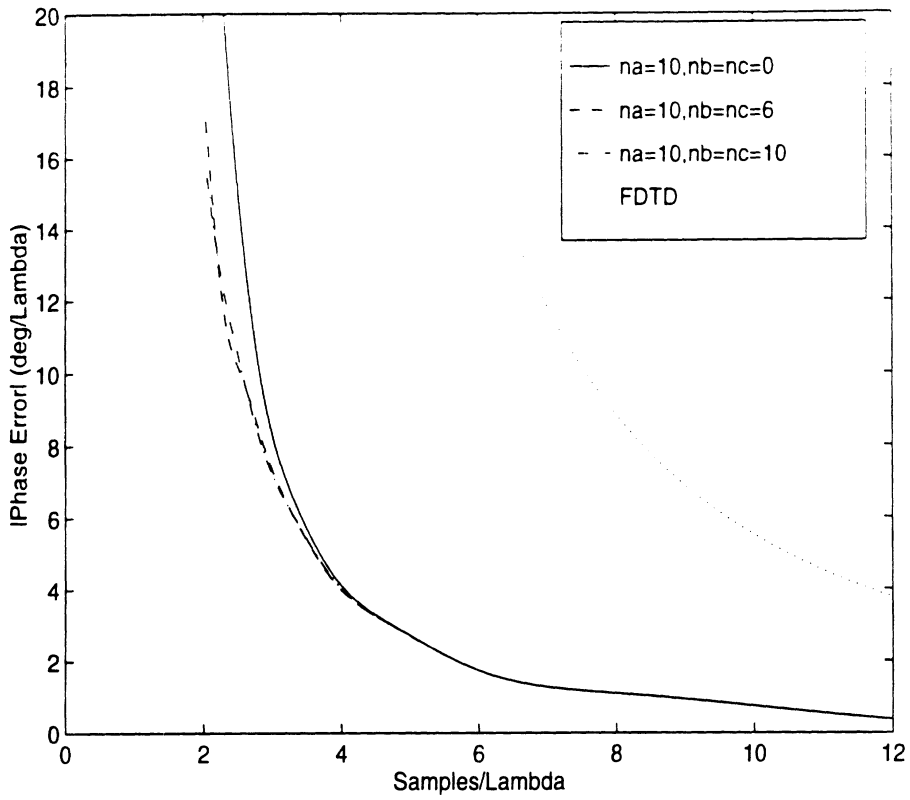

Figure 10: Wavelets Effect on the Dispersion Characteristics of MRTD for n_a=10 (Coarse Grid).

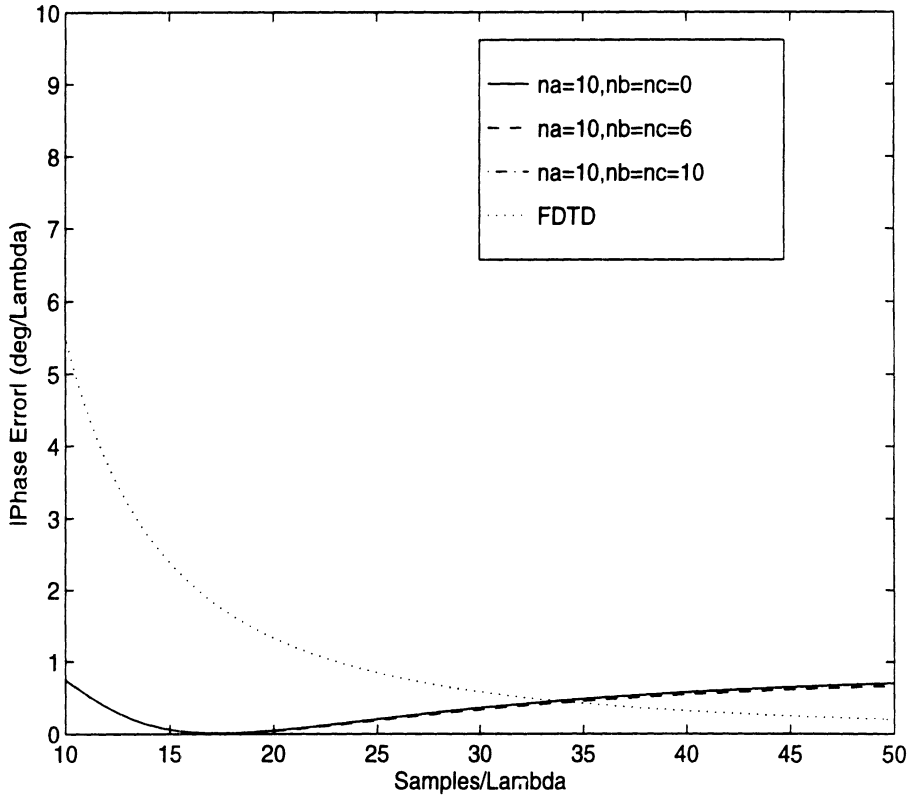

Figure 11: Wavelets Effect on the Dispersion Characteristics of MRTD for n_a=10 (Denser Grid).

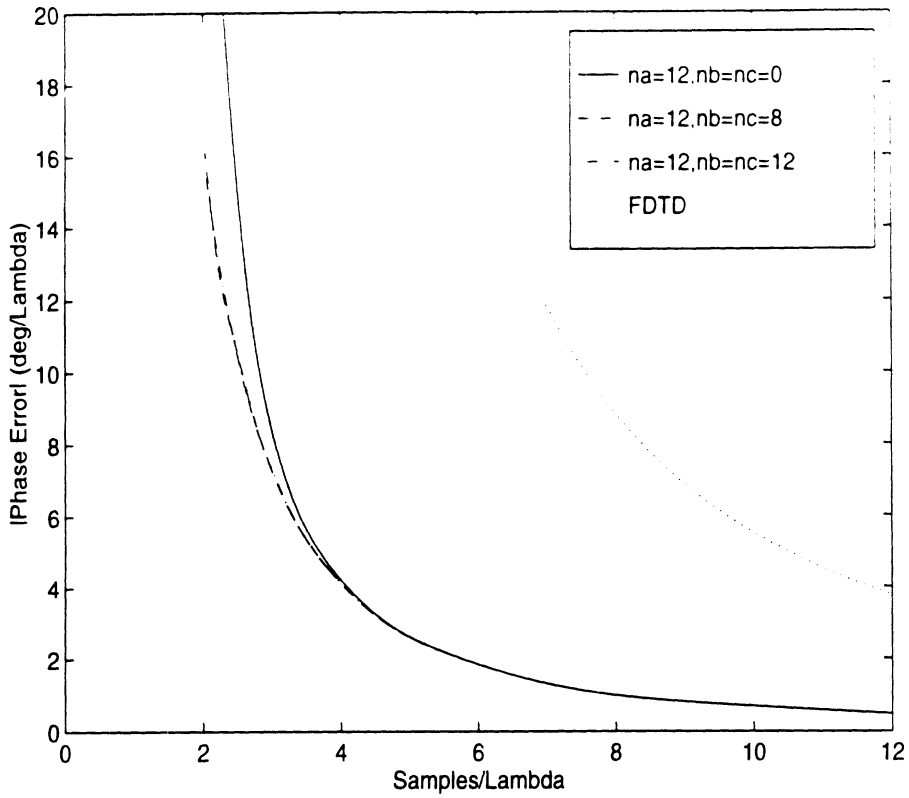

Figure 12: Wavelets Effect on the Dispersion Characteristics of MRTD for n_a=12 (Coarse Grid).

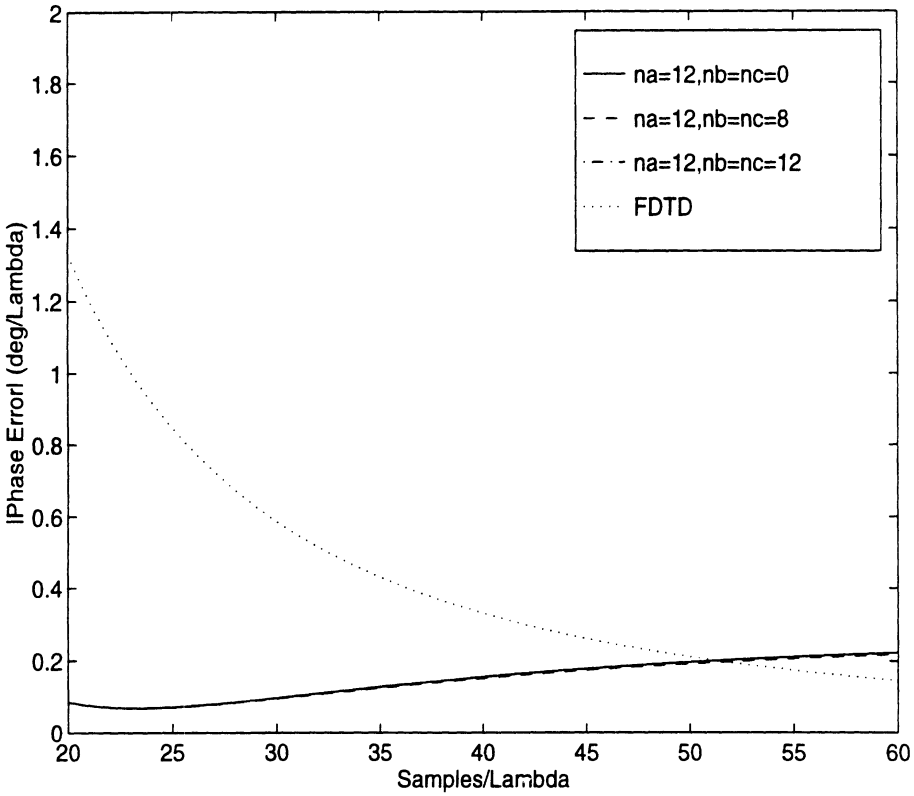

Figure 13: Wavelets Effect on the Dispersion Characteristics of MRTD for n_a=12 (Denser Grid).

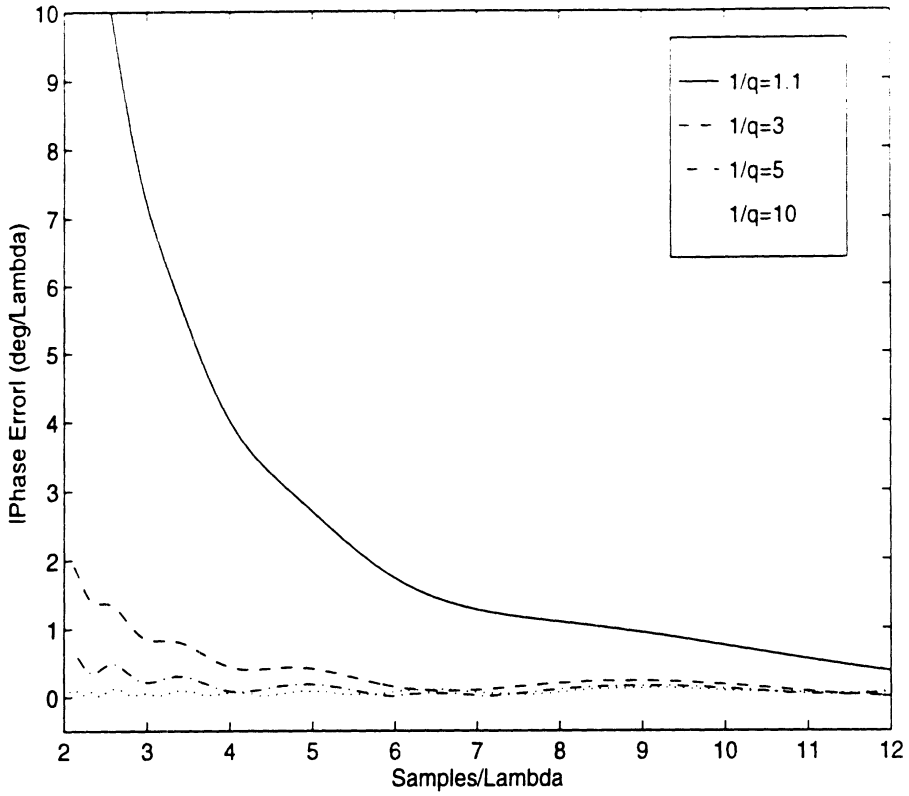

Figure 14: Effect of the Courant Number on the Dispersion Characteristics of $W_0 - MRTD$ for $n_a = n_b = n_c$=10 (Coarse Grid).

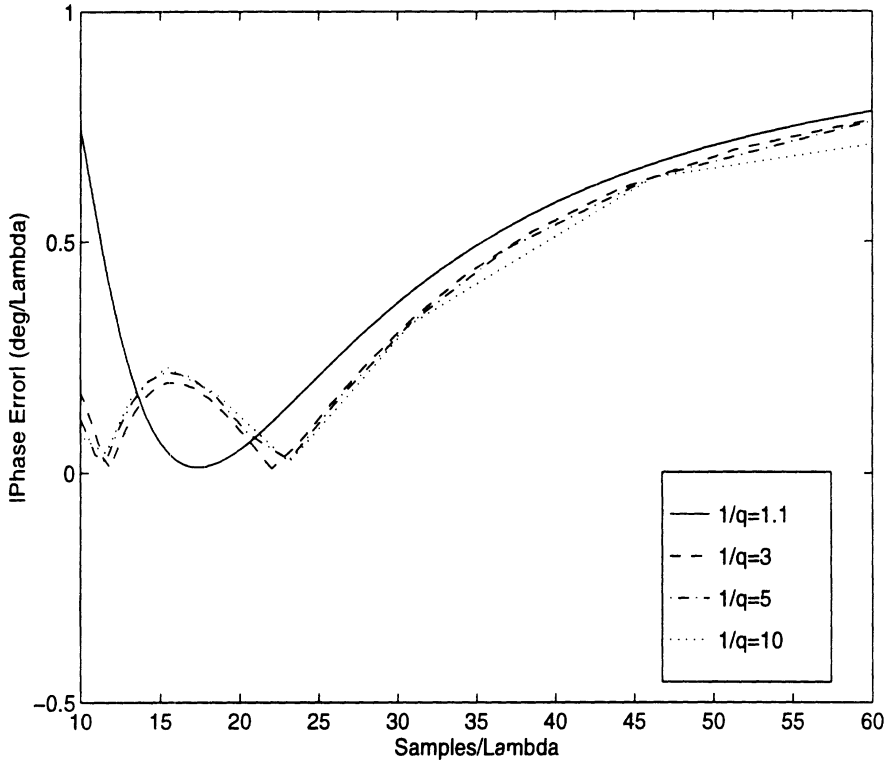

Figure 15: Effect of the Courant Number on the Dispersion Characteristics of $W_0 - MRTD$ for $n_a = n_b = n_c$=10 (Denser Grid).

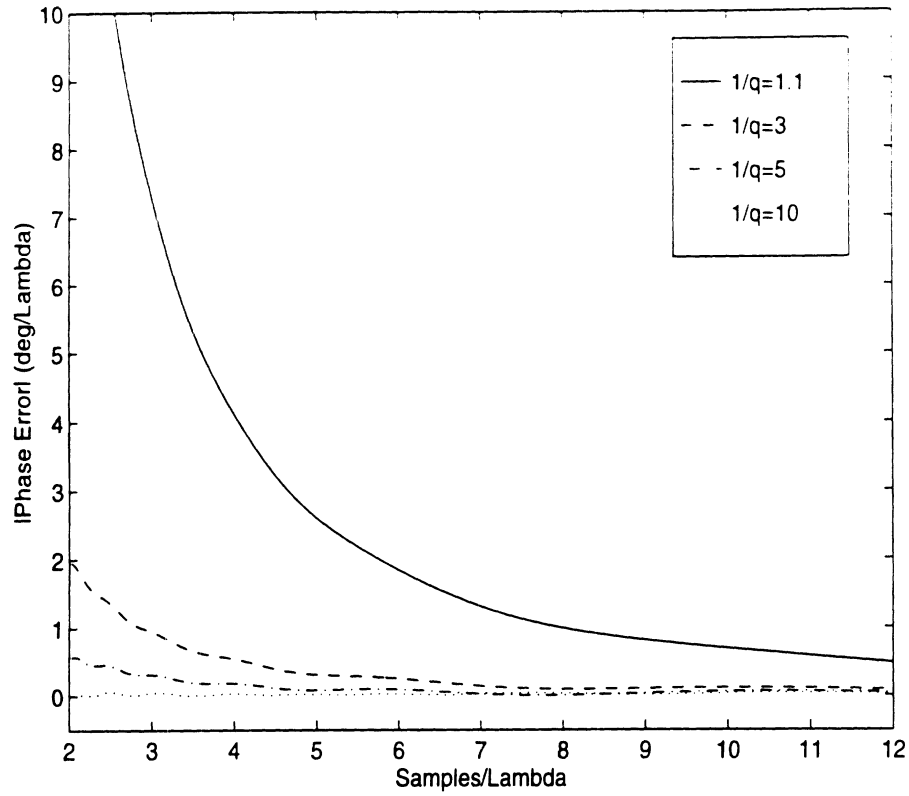

Figure 16: Effect of the Courant Number on the Dispersion Characteristics of $W_0 - MRTD$ for $n_a = n_b = n_c$=12 (Coarse Grid).

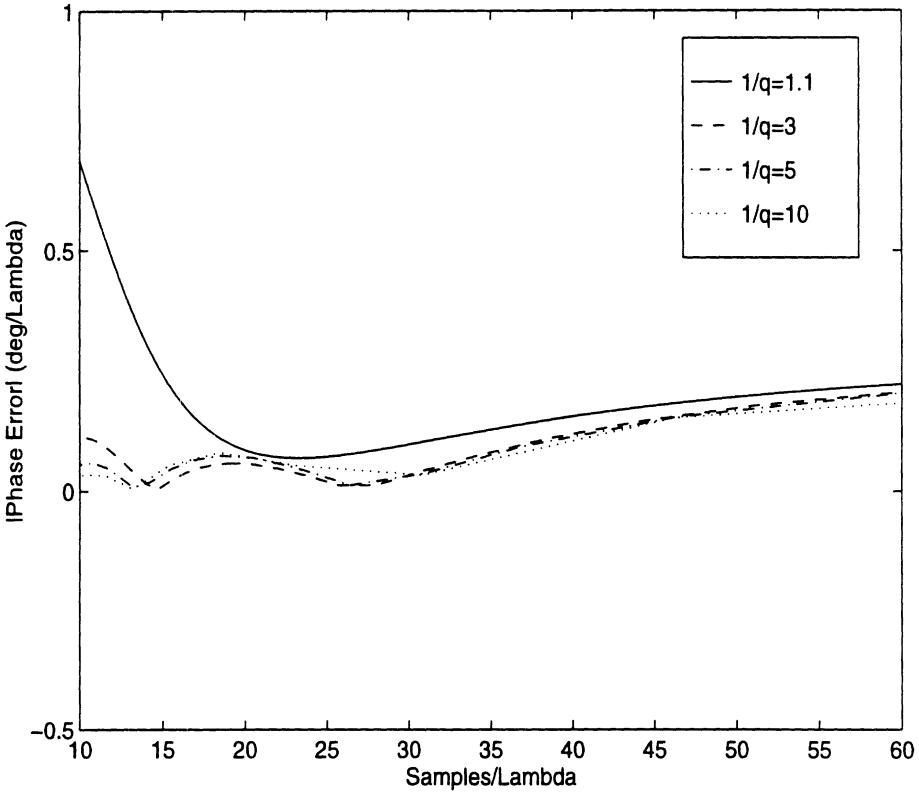

Figure 17: Effect of the Courant Number on the Dispersion Characteristics of $W_0 - MRTD$ for $n_a = n_b = n_c$=12 (Denser Grid).

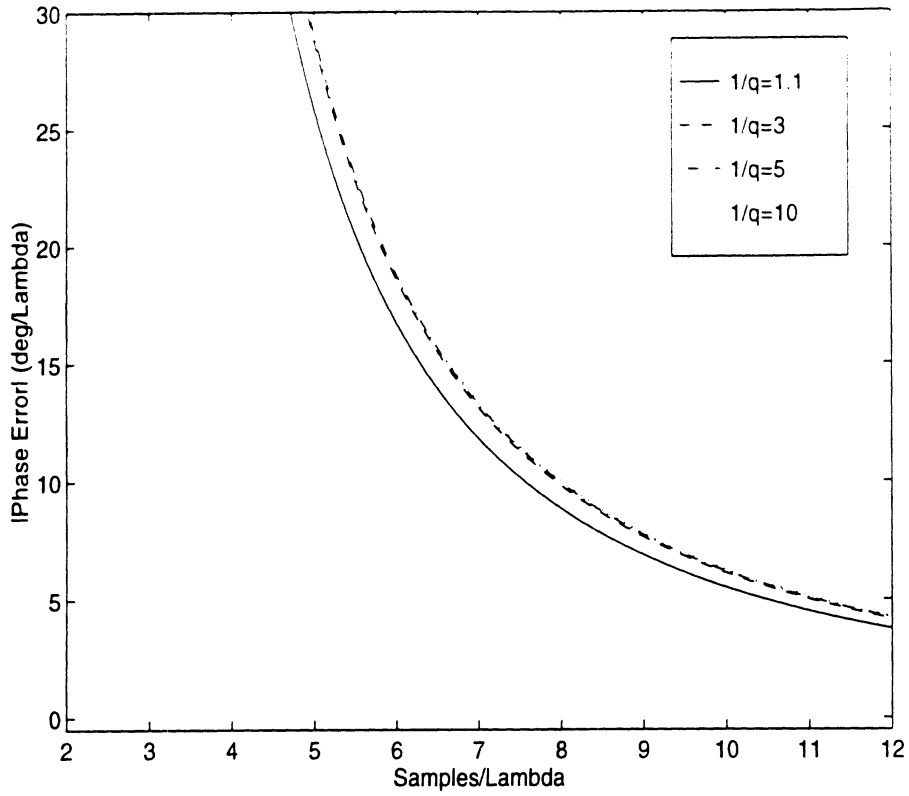

Figure 18: Effect of the Courant Number on the Dispersion Characteristics of FDTD (Coarse Grid).

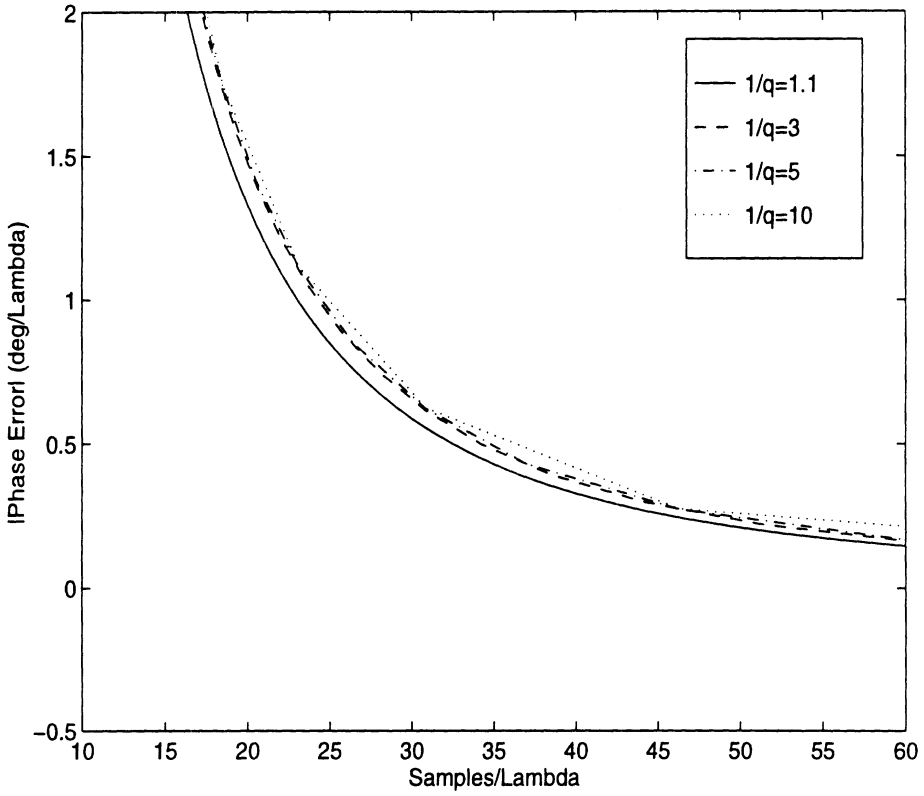

Figure 19: Effect of the Courant Number on the Dispersion Characteristics of FDTD (Denser Grid).

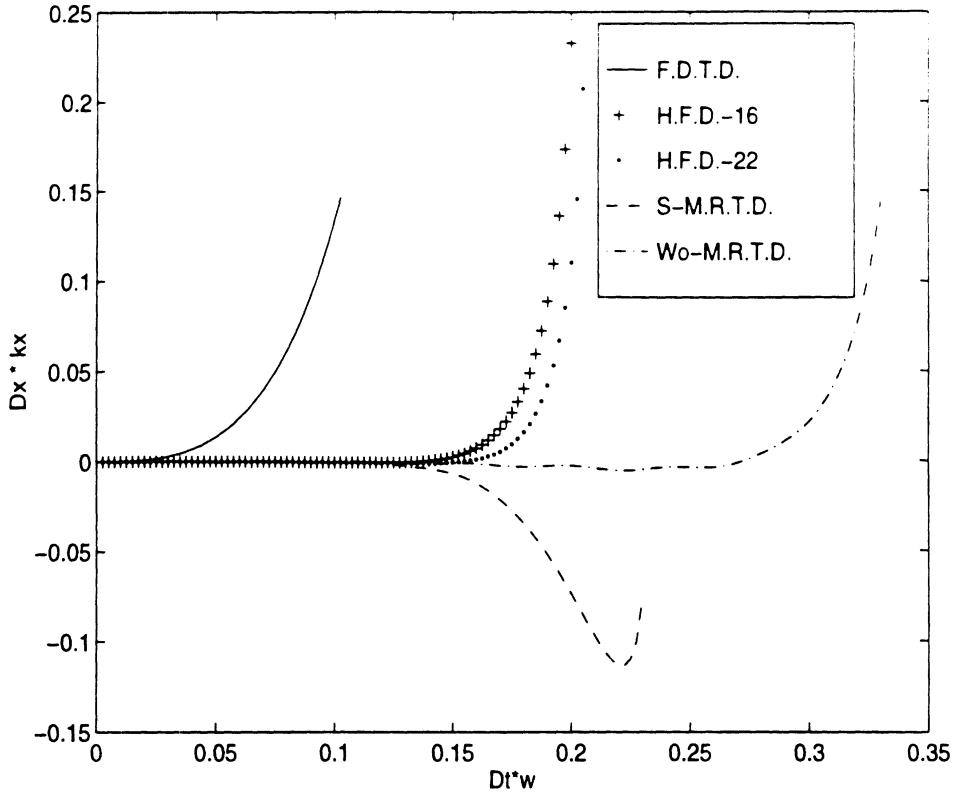

Figure 20: Comparison of the Dispersion Performance of S-MRTD and Wo-MRTD with Different Higher Order Yee's Schemes.

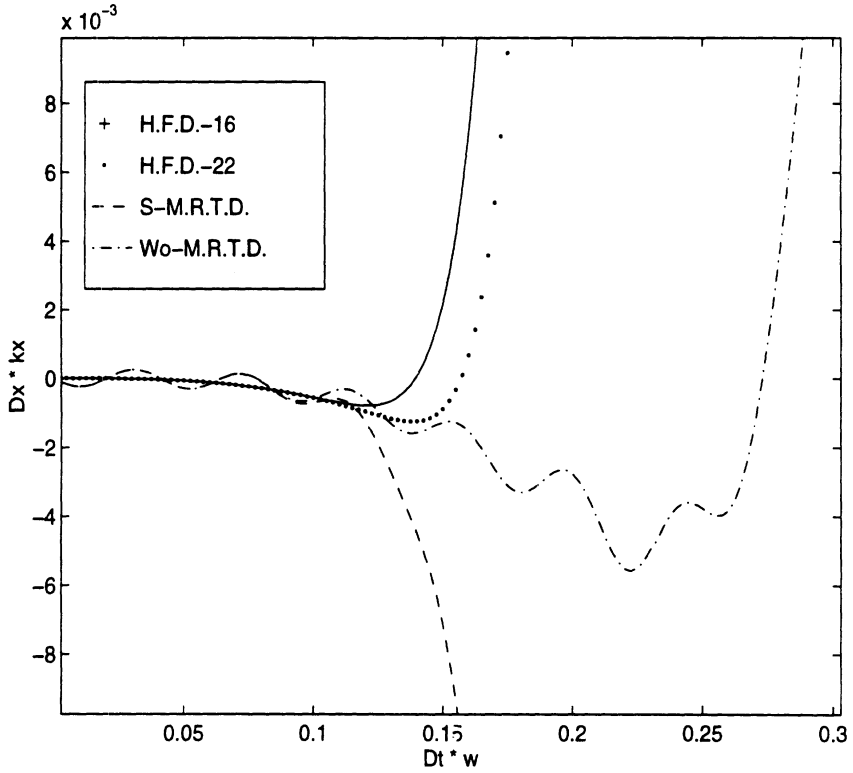

Figure 21: Details of Fig.(20).

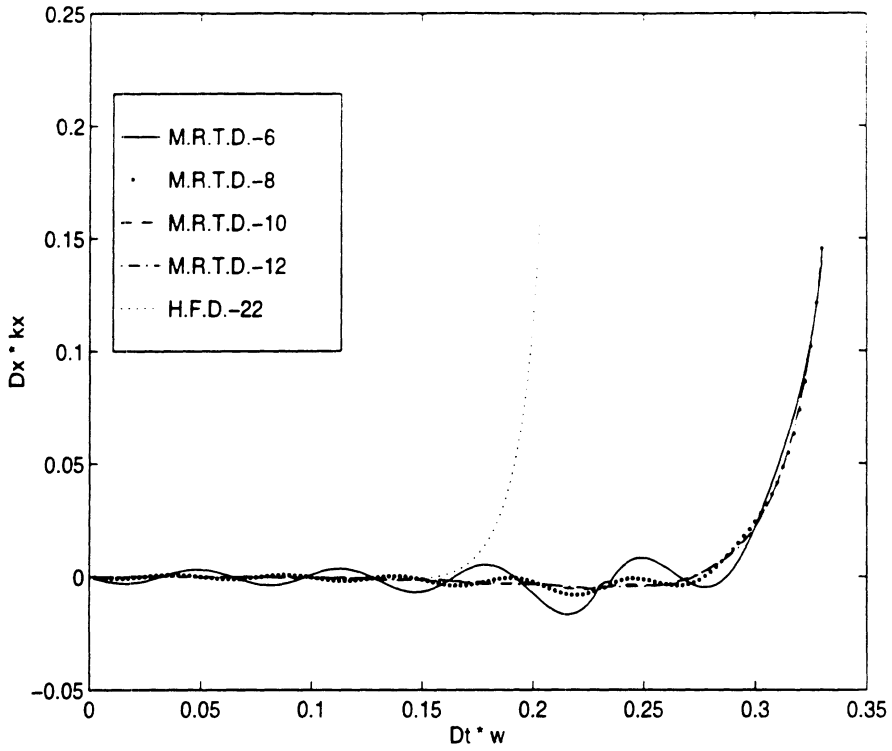

Figure 22: Comparison of the Oscillations of Wo-MRTD Scheme for Different Stencil Size.

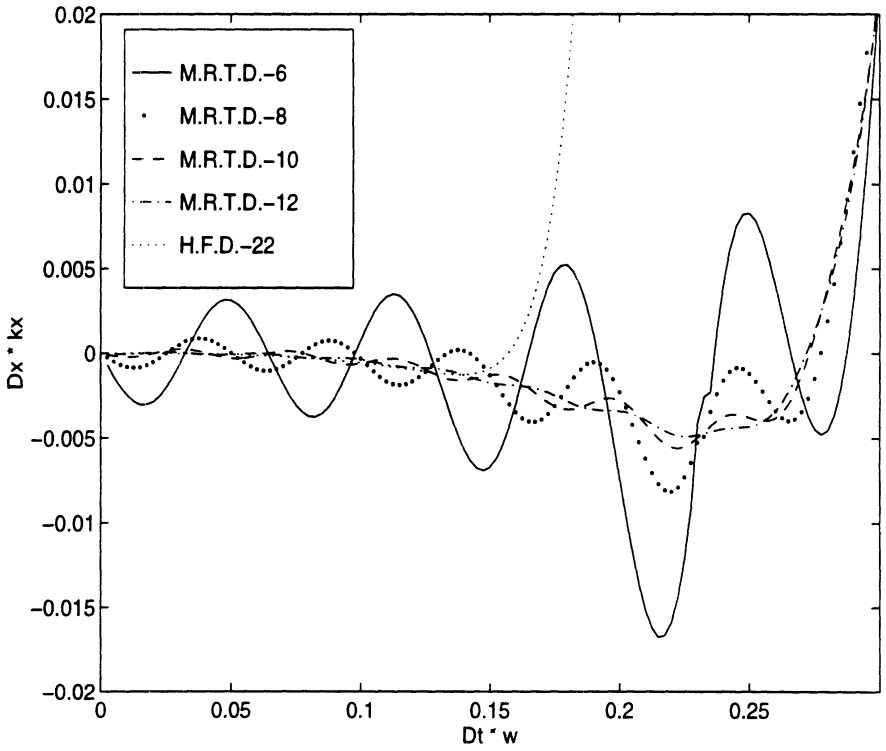

Figure 23: Details of Fig.(22).

Characterization of a CPW–MS Transition for Antenna Applications

R. Robertson, E.M. Tentzeris, T.J. Ellis, L.P.B. Katehi

Radiation Laboratory, Department of Electrical Engineering and Computer Science

University of Michigan, Ann Arbor, MI 48109-2122

Abstract

A full-wave analysis of a Coplanar Waveguide (CPW) to Microstrip (MS) Transition is performed using Finite Difference Time Domain (FDTD) and the High Frequency Structure Simulator (HFSS). The effects from truncating the dielectric substrate around the CPW and microstrip are characterized. Results indicate that decreasing the size of the dielectric substrate does not significantly affect performance.

I Introduction

The general CPW–MS Transition is well covered in the literature [1, 2] and is currently being applied to antenna structures. The antenna structure of interest is a dual–polarized slot–dipole antenna [3]. In this antenna, a coplanar waveguide fed slot antenna is etched into the top of a microstrip fed dipole antenna. In order to feed the antenna from the same side of the substrate, an interconnect which can communicate thru the substrate via electromagnetic coupling is needed. Additionally, the final version of the antenna will operate at high frequencies. Thus, it is necessary that the antenna interconnects have small volume and negligible electrical interference with the rest of the circuit. A transition which satisfies these requirements is a proximity coupled overlay transition [1] between a microstrip and a coplanar waveguide. In this case the electromagnetic coupling occurs in the overlap region between the coplanar waveguide and the microstrip.

As mentioned previously, the volume of the total antenna package at high frequencies is critical. It is necessary to examine the effects of a truncated dielectric on the performance of this transition. Results calculated using FDTD and HFSS are compared for different values of dielectric truncation.

II FDTD Setup

FDTD is a widely–used time–domain full–wave scheme for the characterization of microstrip and coplanar waveguide lines and discontinuities [4, 5]. In FDTD, the propagation of a specific time–dependent function is followed through the structure under test. For the cases discussed below, a Gaussian pulse is chosen as an excitation function due to the fact that it has smooth variation in time. Additionally its Fourier Transform is also a Gaussian function centered at zero frequency. The pulse width of the Gaussian is calculated based on the distance between the excitation and the closest discontinuity [6]. In order to excite the microstrip the vertical electric field under the microstrip is excited. PML absorbing boundary conditions are used in the x–, y– and z–directions as detailed in [7].

Frequency dependent scattering parameters S_{ij} are obtained by probing the vertical electric field [4, 6] at a point between the excitation and the first discontinuity. It should be noted that the FDTD simulation calculates the total field which is the sum of the incident and reflected waveforms along the microstrip. The incident field is obtained by simulating an "infinite" microstrip. By infinite, it is meant that the structure under simulation

is replaced by a microstrip thru-line terminated on both ends with absorber. In the case studied in this paper, careful attention is paid to the width of the truncated dielectric for the infinite microstrip simulations. To obtain the reflected field the incident field data is subtracted from the total field.

III Results

In this section, results generated using FDTD and HFSS are presented for the frequency range from 5 GHz to 35 GHz. The design frequency of this transition is at f = 20 GHz. HFSS is a commercial microwave CAD package that is used to calculate S-parameters and fields of passive high-frequency structures. The setup of the transition in HFSS is straightforward and more information can be found in [8].

Line widths and lengths for the transition structure are shown in Figure 1. Input impedances at the coplanar waveguide and microstrip are 55 Ω. Note that the length of the microstrip is approximately one-quarter of a guided wavelength ($\lambda_{MSguide}/4$) at the design frequency. The parameter D represents the amount that the dielectric is truncated around the coplanar waveguide. In the first case, D is set at 24.5 mils, significantly larger than the $\lambda_{CPWguide}/8$ condition [5]. In the FDTD codes, a mesh of 92 × 153 × 54 is used. This mesh includes the 6 cells of PML added in the x- and z- directions and the 10 cells of PML added in the y- directions, with σ_{max}^{Ex} = 167.0, σ_{max}^{Ey} = 276.0, and σ_{max}^{Ez} = 216.0. These values allow a numerical coefficient of reflection below -50 dB. A Gaussian pulse is applied to excite the microstrip with f_{max} = 410 GHz and is placed 40 mils from the discontinuity created by the overlap. S-parameter results are shown in Figure 2. Overall FDTD and HFSS agree well over a large 3 dB bandwidth, which is on the order of 35 percent. Additionally radiation losses are on the order of 2-3 percent over the entire bandwidth. In the next case, the dielectric distance D is truncated to 7 mils around the CPW region. The FDTD setup is identical to that described above. S-parameter results show nearly the same values as those in Figure 1. Finally, the dielectric distance D is truncated to 3.5 mils around the CPW. Referring to Figure 3, we see a 4 dB improvement in S_{11} at the design frequency of 20 GHz. However 3 dB bandwidth is slightly lower and the radiation losses increase to 4-5 percent over the bandwidth.

IV Conclusion

A full-wave analysis of CPW-to-MS transition is performed. The dielectric layer is truncated in order to observe the effect of performance on the transition. It is found that when the dielectric is truncated from 24 mils to 3.5 mils on either side of the coplanar waveguide, S-parameters do not change significantly. Additionally, bandwidth is preserved and radiation losses increase only slightly. It can be concluded that decreasing the size of the transition package will not significantly affect performance.

V Acknowledgments

This work is made possible by ARL contract QJ8820 and ARO contract DAAH04-95-1-0321.

References

[1] H. Jin, R. Vahldieck, J. Huang and P. Russer, "Rigorous Analysis of Mixed Transmission Line Interconnects Using the Frequency-Domain TLM Method",*IEEE Trans. Microwave Theory and Techniques*, vol. 41, no. 12,pp. 2248-2255.

[2] J.G. Yook, N.I. Dib, and L.P.B. Katehi, "Characterization of High Frequency Interconnects Using Finite Difference Time Domain and Finite Element Methods", *IEEE Trans. Microwave Theory and Techniques*, vol. 42, no. 9, pp. 1727-1736.

[3] T.J. Ellis, R.L. Robertson, L.P.B. Katehi and G.M. Rebeiz, "A Dual Polarized Planar Antenna for Phased Array Applications", accepted to the *Advanced Sensors Consortium* second annual conference, Feb. 2-3, 1997.

[4] D. Sheen, S. Ali, M. Abouzahra and J. Kong, "Application of the Three-Dimensional Finite-Difference Time-Domain Method to the Analysis of Planar Microstrip Circuits",*IEEE Trans. Microwave Theory and Techniques*, vol. 38, no. 7, pp. 849-856.

[5] G. Liang, Y. Liu and K. Mei,"Full-Wave analysis of coplanar waveguide and slotline using the time-domain finite-difference method",*IEEE Trans. Microwave Theory and Techniques*, vol. 37, no. 12, pp. 1949-1957.

[6] X. Zhang and K.K. Mei, "Time-Domain Finite Difference Approach to the Calculation of the Frequency-Dependent Characteristics of Microstrip Discontinuities",*IEEE Trans. Microwave Theory and Techniques*, vol. 36, no. 12, pp. 1775-1787.

[7] J.P. Berenger, "A Perfectly Matched Layer for the Absorption of Electromagnetic Waves", *J.Comput. Physics*, vol. 114, pp. 185-200, 1994.

[8] HP 851080A High-Frequency Structure Simulator User's Reference, Release 3.0, December 1994.

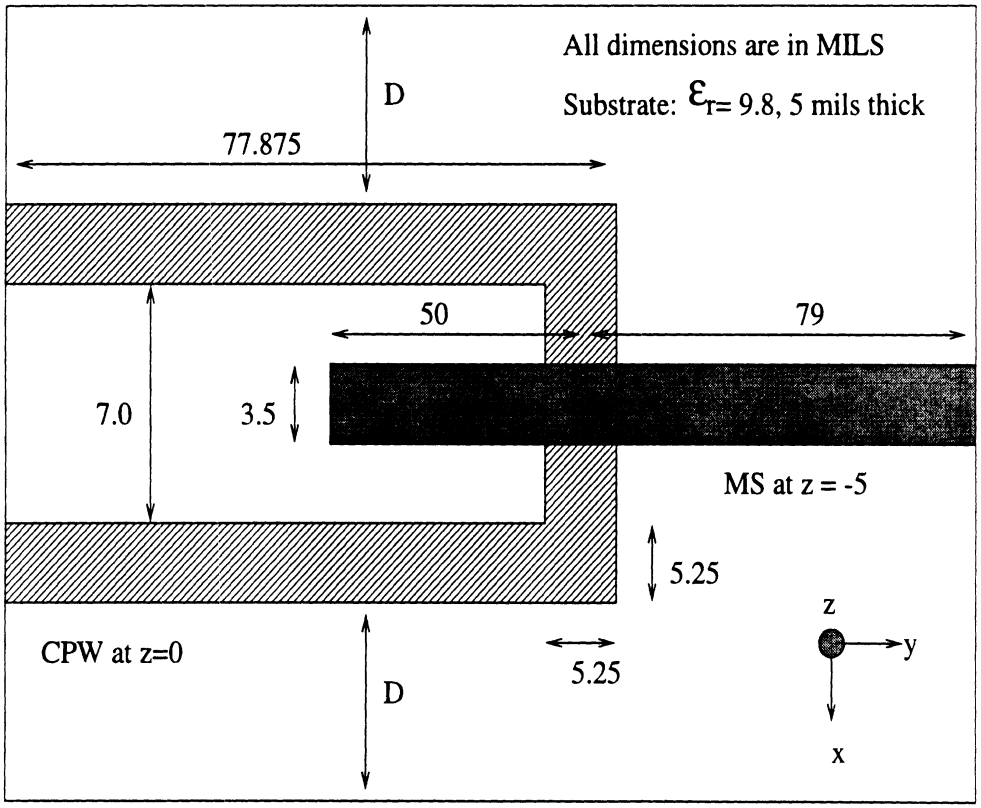

Figure 1: CPW–MS Transition

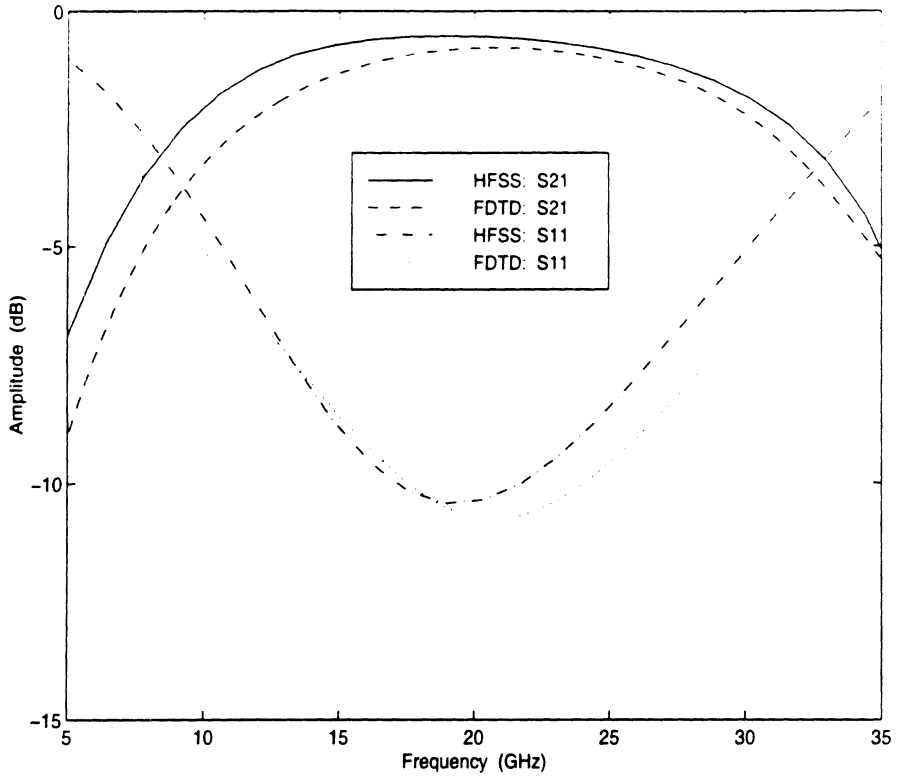

Figure 2: Transition S–parameters for D = 24.5 mils

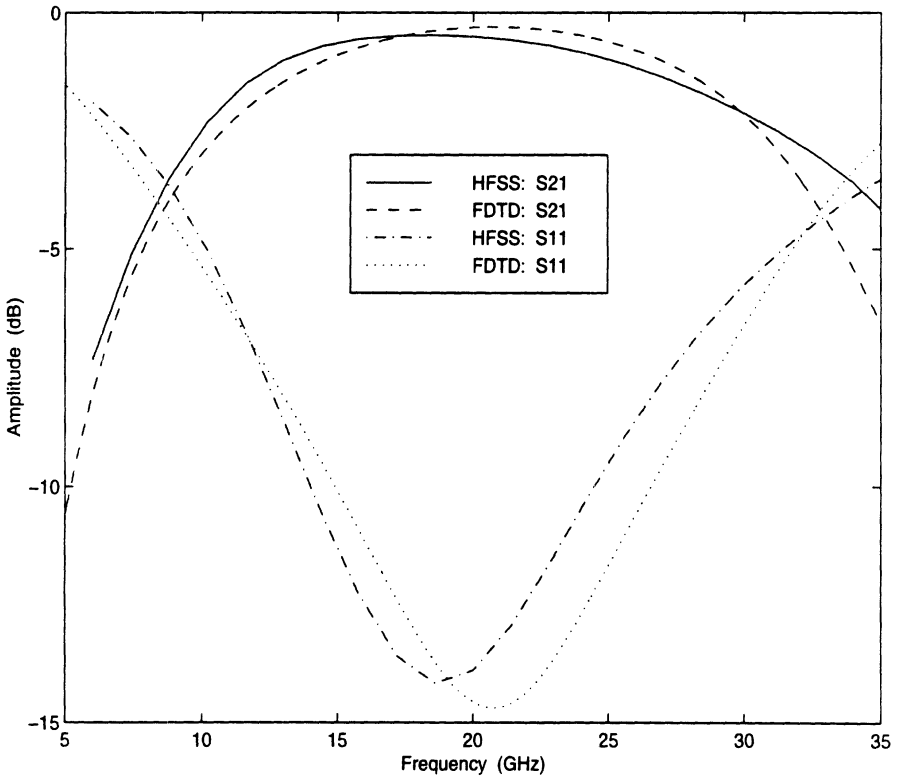

Figure 3: Transition S–parameters for D=3.5 mils

Modelling of Membrane Patch Antennas Using MRTD Analysis

R. Robertson, E.M. Tentzeris, Linda P.B. Katehi

Radiation Laboratory, Department of Electrical Engineering and Computer Science
University of Michigan, Ann Arbor, MI 48109-2122

Abstract

The Multiresolution Time-Domain (MRTD) scheme with perfectly matched layer (PML) absorbing boundaries is applied to the analysis of a membrane patch antenna. The results are compared to those obtained by use of the conventional FDTD technique and substantial reductions in memory requirements are observed.

I Introduction

Recently Multiresolution Time-Domain Analysis has been successfully applied to simulate a variety of microwave structures [1]. MRTD has performed complete analysis of both planar circuits [2] and resonating structures [3]. Additionally conventional FDTD absorbers, such as PML [4] have been generalized in order to analyze open planar structures [5]. In all cases, MRTD has demonstrated a high degree of savings in execution time and memory requirements with respect to FDTD.

In this paper the techniques described are applied to the simulation of a membrane patch antenna with a center frequency of 9 GHz. Full 3D MRTD analysis with PML along three coordinate directions is used to simulate the antenna. The MRTD scheme is applied to the calculation of S-parameters for the membrane antenna and is compared to conventional FDTD.

II Application of PML to the 3D MRTD scheme

To derive the 3D MRTD scheme, the field components in Maxwell's E-curl and H-curl equations are represented by a series of cubic spline Battle-Lemarie scaling functions in space and pulse functions in time. These equations are sampled with pulse functions in time- and scaling functions in space-domain, as detailed in [1]. As an example, consider the discretization of:

$$\epsilon \frac{\partial E_x}{\partial t} = \frac{\partial H_z}{\partial y} - \frac{\partial H_y}{\partial z}. \tag{1}$$

For a homogeneous medium with the permittivity ϵ, expanding and sampling $\partial E_x/\partial t$, $\partial H_z/\partial y$ and $\partial H_y/\partial z$ with scaling and pulse functions in space and time gives

$$\frac{\epsilon}{\Delta t}\left({}_{k+1}E^{\phi x}_{l+1/2,m,n} - {}_{k}E^{\phi x}_{l+1/2,m,n}\right) = \frac{1}{\Delta y}\sum_{i=m-9}^{m+8} a(i)\ {}_{k+1/2}H^{\phi z}_{l+1/2,i+1/2,n} - \frac{1}{\Delta z}\sum_{i=n-9}^{n+8} a(i)\ {}_{k+1/2}H^{\phi y}_{l+1/2,m,i+1/2}\ , \tag{2}$$

where ${}_{k}E^{\phi x}_{l,m,n}$, ${}_{k}H^{\phi z}_{l,m,n}$ and ${}_{k}H^{\phi y}_{l,m,n}$ are the coefficients for the electric and magnetic field expansions. The indices l, m, n and k are the discrete space and time indices related to the space and time coordinates via $x = l\Delta x$, $y = m\Delta y$, $z = n\Delta z$ and $t = k\Delta t$, where Δx, Δy, Δz are the space discretization intervals in x-, y- and z-directions and Δt is the time discretization interval. The coefficients $a(i)$ are given in [1].

To derive the perfectly matched layer (PML) technique [4] along one coordinate direction it is assumed that the conductivity is given in terms of scaling functions with respect to space. The spatial distribution of the

conductivity for the absorbing layers is simulated by assuming that the amplitudes of the scaling functions have a parabolic distribution [5]. For the PML absorbing material in the y-direction with ϵ, μ and conductivity σ^E, the term $\sigma^E_{(y)}E_x$ must be added to the left side of eq.(1). Then, substituting the following into eq.(1):

$$E_i(x,y,z,t) = \tilde{E}_i(x,y,z,t)e^{-\sigma^E_{(y)}t/\epsilon} \tag{3}$$

$$H_i(x,y,z,t) = \tilde{H}_i(x,y,z,t)e^{-\sigma^H_{(y)}t/\mu}, \tag{4}$$

and assuming that the PML is only along the y-direction leads to the following equation:

$$\begin{aligned} {}_{k+1}E^{\phi x}_{l+1/2,m,n} &= e^{-\sigma^E_{(m\Delta y)}\Delta t/\epsilon}\,{}_kE^{\phi x}_{l+1/2,m,n} + \frac{\Delta t}{\epsilon}e^{-\sigma^E_{(m\Delta y)}(\Delta t/2)/\epsilon}\Big(\frac{1}{\Delta y}\sum_{i=m-9}^{m+8} a(i)_{k+1/2}H^{\phi z}_{l+1/2,i+1/2,n} + \\ &+ \frac{1}{\Delta z}\sum_{i=m-9}^{m+8} a(i)_{k+1/2}H^{\phi y}_{l+1/2,m,i+1/2}\Big) \end{aligned} \tag{5}$$

For all simulations, a parabolic distribution of the conductivity σ is used in the PML region (N cells):

$$\sigma^{E,H}_{(m\Delta y)} = \sigma^{E,H}_{max}\Big(\frac{m}{N}\Big)^2 \qquad \text{for m=0,1,..,N,} \tag{6}$$

where $\sigma^{E,H}_{max}$ is the maximum conductivity at the end of the absorbing layer. As in [4], the magnetic conductivity σ^H has to be chosen as:

$$\frac{\sigma^E_{(m\Delta y)}}{\epsilon} = \frac{\sigma^H_{(m\Delta y)}}{\mu} \qquad \text{for m=0,1,..,N,} \tag{7}$$

for a perfect absorption of the outgoing waves. The MRTD mesh is terminated by a perfect electric conductor (PEC) at the end of the PML region, modelled by applying the image theory.

While the above derivation is adequate for a structure which only needs to be terminated with PML along one direction, such as a shielded thru-line, structures such as patch antennas need PML termination in all three coordinate directions. In this case, the derivation discussed above needs to be extended to three dimensions. The procedure is straightforward and results in the following equation:

$$\begin{aligned} {}_{k+1}E^{\phi x}_{l+1/2,m,n} &= e^{-\sigma^E_{(l\Delta x)}\Delta t/\epsilon}e^{-\sigma^E_{(m\Delta y)}\Delta t/\epsilon}e^{-\sigma^E_{(n\Delta z)}\Delta t/\epsilon}\,{}_kE^{\phi x}_{l+1/2,m,n} + \\ &+ \frac{\Delta t}{\epsilon}e^{-\sigma^E_{(l\Delta x)}(\Delta t/2)/\epsilon}e^{-\sigma^E_{(m\Delta y)}(\Delta t/2)/\epsilon}e^{-\sigma^E_{(n\Delta z)}(\Delta t/2)/\epsilon}\Big(\frac{1}{\Delta y}\sum_{i=m-9}^{m+8} a(i)_{k+1/2}H^{\phi z}_{l+1/2,i+1/2,n} + \\ &+ \frac{1}{\Delta z}\sum_{i=m-9}^{m+8} a(i)_{k+1/2}H^{\phi y}_{l+1/2,m,i+1/2}\Big) \end{aligned} \tag{8}$$

As in eq.(6) a parabolic distribution for the conductivity is applied in the x-, y- and z-directions.

III Applications of the 3D-MRTD scheme

The object of this paper is to apply the 3D MRTD scheme to the analysis of membrane patch antennas. However, in order to test the application of PML to the 3D MRTD scheme, a microwave thru-line is analyzed using MRTD and FDTD. The thru-line has a width of 0.4 mm and length of 10.0 cm and is placed in the center of a cavity with dimensions $1.6mm \times 10.0cm \times 1.6mm$. A Gaussian pulse is used to excite the thru-line

with $f_{max} = 50GHz$ [6] and is placed in the middle of the center conductor 9 mm from the PML layer along the y-axis. The FDTD analysis uses 16 x 100 x 16 mesh while the MRTD analysis uses a 8 x 20 x 8 mesh. Additionally six cells of PML are used along the y-direction at either end of the thru-line with a $\sigma^{Ey}_{max} = 3.0$. Therefore the total discretization of the thru line is 16 x 112 x 16 for FDTD and 8 x 32 x 8 for the MRTD scheme, resulting in a factor of 14.0 savings in memory. The time discretization interval for the MRTD scheme is $\Delta t = 3.92 \cdot 10^{-14}s$, while the FDTD scheme has $\Delta t = 6.335 \cdot 10^{-14}s$. In both cases, the simulation is performed for 6000 time steps. A comparison plot of time vs. Ez-field amplitude is shown in Figure 1. Note that the amplitude of the Gaussian has been normalized and the time-steps multiplied by a constant factor in order to compare the two plots more easily. The initial Gaussian pulse has been completely absorbed by the PML layer along the y-direction.

The membrane patch antenna shown in Figure 2 is simulated using 3D MRTD and FDTD. A full description of the parameters of the antenna can be found in [7]. A PML layer of six cells is used along the $\pm x$, $\pm y$ and $+z$ directions, resulting in an FDTD mesh of 72 x 112 x 28 and a MRTD mesh of 42 x 62 x 12, a factor of 7.22 savings in memory. In the PML layers $\sigma^{Ex}_{max} = \sigma^{Ey}_{max} = \sigma^{Ez}_{max} = 3.0$ for FDTD and MRTD. The time discretization interval used for the MRTD scheme is $\Delta t = 1.6008 \cdot 10^{-13}s$ while the FDTD time discretization interval is $\Delta t = 1.3297 \cdot 10^{-13}s$. In both cases the simulation is performed for 7000 time steps. The antenna feed line is 20 mm long and the Gaussian pulse is sent from a point y=4 mm from the edge of the PML layer in the FDTD and MRTD simulations. Figure 3 shows a plot of Ez field values vs. time for MRTD and FDTD. Measurement of the intial and reflected normalized Gaussian pulses occurred at y = 14 mm from the edge of the PML layer. Figure 4 shows a plot of the calculated S_{11} [7] for the membrane patch antenna. Note that excellent correlation is achieved between FDTD and MRTD results.

IV Conclusion

A membrane patch antenna is successfully simulated using the 3D MRTD scheme with PML absorber along the x-, y- and z-directions. With respect to calculated S_{11} results MRTD shows excellent correlation with FDTD while exhibiting a memory savings with a factor of 7.22.

References

[1] M. Krumpholz and L.P.B. Katehi, "MRTD: New Time Domain Schemes Based on Multiresolution Analysis", IEEE Trans. Microwave Theory and Techniques, vol. 44,no. 4,pp. 555-561.

[2] E. Tentzeris, M. Krumpholz and L.P.B. Katehi, "Application of MRTD to Printed Transmission Lines", Proc. MTT-S 1996, pp. 573-576.

[3] R. Robertson, E. Tentzeris, M. Krumpholz and L.P.B. Katehi, "Application of MRTD Analysis to Dielectric Cavity Structures",Proc. MTT-S 1996, pp. 1840-1843.

[4] J.P. Berenger, "A Perfectly Matched Layer for the Absorption of Elecromagnetic Waves", J.Comput. Physics, vol. 114, pp. 185-200, 1994.

[5] E. Tentzeris, R. Robertson, M. Krumpholz and L.P.B. Katehi, "Application of the PML Absorber to the MRTD Technique", Proc. AP-S 1996, pp. 634-637.

[6] X. Zhang and K.K. Mei, "Time-Domain Finite Difference Approach to the Calculation of the Frequency-Dependent Characteristics of Microstrip Discontinuities", IEEE Trans. Microwave Theory and Techniques, vol. 36, no. 12, pp. 1775-1787.

[7] D. Sheen, S. Ali, M. Abouzahra and J. Kong, "Application of the Three-Dimensional Finite-Difference Time-Domain Method to the Analysis of Planar Microstrip Circuits", IEEE Trans. Microwave Theory and Techniques, vol. 38, no. 7, pp. 849-856.

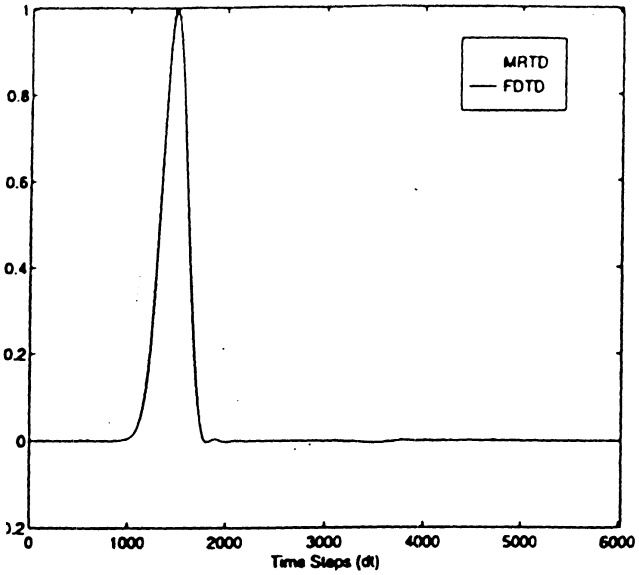

Figure 1: Time-Domain Analysis of a Microstrip Thru-Line.

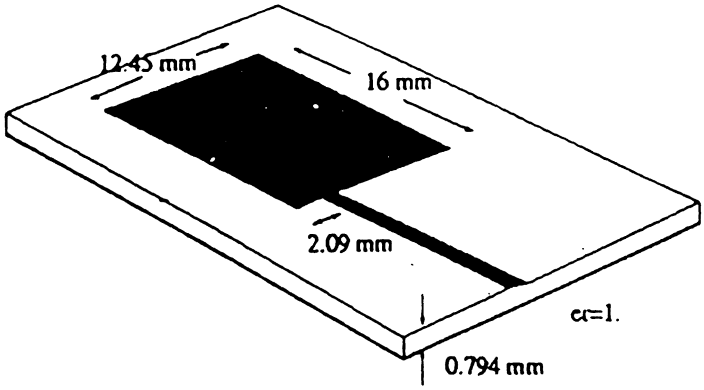

Figure 2: Membrane Patch Antenna.

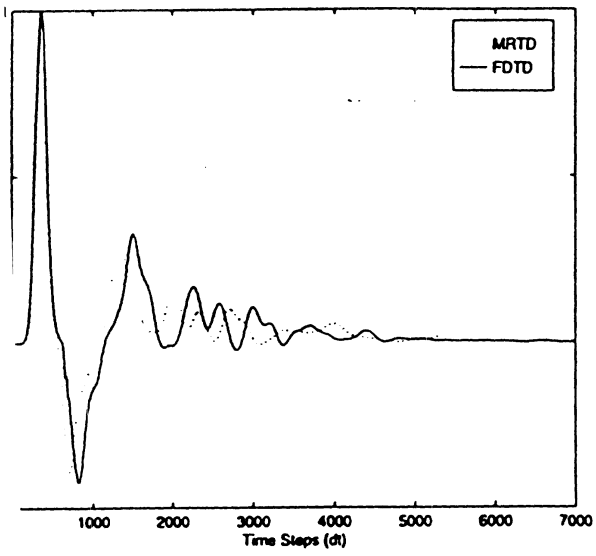

ure 3: Time Domain Analysis of a Membrane Patch Antenna.

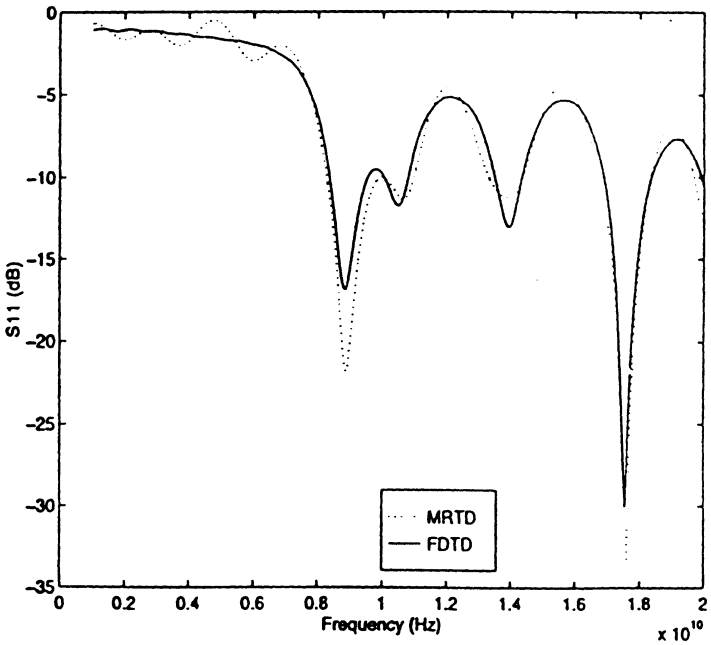

Figure 4: Simulated S11 results for the Patch Antenna.

SPACE- AND TIME- ADAPTIVE GRIDDING USING MRTD TECHNIQUE

Emmanouil M. Tentzeris, Robert L. Robertson, Linda P.B. Katehi
Radiation Laboratory, Department of Electrical Engineering and Computer Science
University of Michigan, Ann Arbor, MI 48109-2122

Andreas Cangellaris
Department of Electrical and Computer Engineering
University of Arizona, Tucson, AZ

Abstract- The MRTD scheme is applied to the analysis of waveguide problems. Specifically, the field pattern and the S-parameters of a dielectric-loaded parallel-plate waveguide are calculated. The use of wavelets enables the implementation of a space- and time-adaptive gridding technique. The results are compared to those obtained by use of the conventional FDTD scheme to indicate considerable savings in memory and computational time.

I Introduction

Recently a new technique has been successfully applied [1-4] to a variety of microwave problems and has demonstrated unparalleled properties. This technique is derived by the use of multiresolution analysis for the discretization of the time-domain Maxwell's equations. The multiresolution time domain technique (MRTD) based on Battle Lemarie functions has been applied to linear as well as nonlinear propagation problems. The PML absorbing boundary condition has been generalized in order to analyze open planar structures. MRTD has demonstrated savings in time and memory of two orders of magnitude. In addition, the most important advantage of this new technique is its capability to provide space and time adaptive gridding without the problems that the conventional FDTD is encountering. This is due to the use of two separate sets of basis functions, the scaling and wavelets and the capability to threshold the field coefficients due to the excellent conditioning of the formulated mathematical problem.

In this paper, a space/time adaptive gridding algorithm based on the MRTD scheme is proposed and applied to the waveguide problems. As an example, the propagation of a Gabor pulse in a partially-filled parallel-plate waveguide is simulated and the S-parameters are evaluated. Wavelets are placed only at locations where the EM fields have significant values, creating a space- and time- adaptive dense mesh in regions of strong field variations, while maintaining a much coarser mesh elsewhere.

II The 2D-MRTD scheme

For simplicity the 2D-MRTD scheme for the TM_z modes will be used herein. To derive the 2D-MRTD scheme, the field components are represented by a series of cubic spline Battle-Lemarie [?] scaling and wavelet functions to the longitudinal direction in space and pulse functions in time. After inserting the field expansions in Maxwell's equations, we sample them using pulse functions in time and scaling/wavelet functions in space domain.

As an example, sampling $\partial D_x/\partial t, = -\partial H_y/\partial z$ in space and time, the following difference equation is obtained

$$\frac{1}{\Delta t}({}_{k+1}D^{\phi x}_{l+1/2,m} - {}_{k}D^{\phi x}_{l+1/2,m}) =$$

$$-\frac{1}{\Delta y}\Big(\sum_{i=m-m_2}^{m+m_2} a(i)_{k+1/2}\, H^{cy}_{l+1/2,i+1/2}$$

$$+\sum_{i=m-m_4}^{m+m_3} b(i)_{k+1/2}\, H^{\psi y}_{l+1/2,i+1/2}\Big) \quad , \qquad (1)$$

$$\frac{1}{\Delta t}\left({}_{k+1}D^{\psi x}_{l+1/2,m} - {}_{k}D^{\psi x}_{l+1/2,m}\right) =$$

$$-\frac{1}{\Delta y}\Big(\sum_{i=m-m_4}^{m+m_3} b(i)_{k+1/2}\, H^{\phi y}_{l+1/2,i+1/2}$$

$$+\sum_{i=m-m_6}^{m+m_5} c(i)_{k+1/2}\, H^{\psi y}_{l+1/2,i+1/2}\Big) \quad , \qquad (2)$$

where ${}_{k}D^{\xi x}_{l,m}$ and ${}_{k}H^{\xi y}_{l,m}$ with ξ=ϕ (scaling),ψ (wavelets) are the coefficients for the electric and magnetic field expansions. The indices l, m and k are the discrete space and time indices, which are related to the space and time coordinates via $x = l\Delta x$,$z = m\Delta z$ and $t = k\Delta t$, where Δx,Δz are the space discretization intervals in x- and z-direction and Δt is the time discretization interval. The coefficients $a(i), b(i), c(i)$ are derived and given in [?]. For an accuracy of 0.1% the values $m_1 = m_5 = 8$,$m_2 = m_3 = m_4 = m_6 = 9$ have been used.

For open structures, the perfectly matched layer (PML) technique can be applied by assuming that the conductivity is given in terms of scaling and wavelet functions instead of pulse functions with respect to space [?]. The spatial distribution of the conductivity for the absorbing layers is modelled by assuming that the amplitudes of the scaling functions have a parabolic distribution. The MRTD mesh is terminated by a perfect electric conductor (PEC) at the end of the PML region. Usually, 8-16 cells of PML medium with σ^E_{max}=0.4S/m provide reflection coefficients smaller than -90 dB.

In order to use a pulse excitation at $z = m\Delta z$ with respect to space and to obtain an excitation identical to an FDTD excitation, we decompose the pulse in terms of scaling and wavelet functions

$${}_{k}E^{pulse}_{m} \approx E_F(0, k\Delta t)$$

$$\Big(\sum_{i=-4}^{+4} c_\phi(i)\phi_{m+i} + \sum_{i=-4}^{+4} c_\psi(i)\psi_{m+i}\Big) \qquad (3)$$

where the coefficients $c_\phi(i), c_\psi(i)$ are given in Table 1 for $i \geq 0$. For $i < 0$ it is $c_\phi(-i) = c_\phi(i)$ and $c_\psi(i) = c_\psi(1-i)$. $E_F(0, k\Delta t)$ is the time dependence of the excitation. For $|i| \leq 4$, the above excitation components are superimposed to the field values obtained by the MRTD algorithm. For example, the total $E^o_{k,m+i}$ will be given by

$$E^o_{k,m+i}\Big|_{total} = E_F(0, k\Delta t)\, c_\phi(i) + E^o_{k,m+i}$$

Due to the nature of the Battle-Lemarie expansion functions, the total field is a summation of the contributions from the non-localized scaling and wavelet functions. For example, the total electric field $E_x(x_o, z_o, t_o)$ with $(k-1/2)\Delta t < t_o < (k+1/2)\Delta t$ is calculated in the same way with [?, ?] by

$$E_x(x_o, z_o, t_o) = \sum_{l',m'=-l_1}^{l_1} {}_{k}E^{\phi x}_{l'+1/2,m'}\, \phi_{l'+1/2}(x_o)\, \phi_{m'}(z_o)$$

$$+\sum_i \sum_{l',m'=-l_{2,i}}^{l_{2,i}} {}_{k}E^{\psi_i x}_{l'+1/2,m'}\, \phi_{l'+1/2}(x_o)\, \psi_{i,m'}(z_o)$$

where $\phi_m(x) = \phi(\frac{x}{\Delta x} - m)$ and $\psi_{i,m}(x) = \psi_i(\frac{x}{\Delta x} - m)$ represent the Battle-Lemarie scaling and i-resolution wavelet function respectively. For an accuracy of 0.1% the values $l_1 = l_{2,i} = 4$ have been used.

There are many different ways to take advantage of the capability of the MRTD technique to provide space and time adaptive gridding. In DSP, thresholding of the wavelet coefficients over a specific time- and space- window (5-10 points) contribute significant memory economy, but increase the implementation complexity and the execution time. The simplest way is to threshold the wavelet components to a fraction (usually $\leq$ 0.1%) of the scaling function at the same cell for each time-step. All components below this threshold are eliminated from the subsequent calculations. This is the simplest thresholding algorithm. It doesn't add any significant overhead in execution time, but it offers only a moderate (pessimistic) economy in memory (factor close to 2). Also, this algorithm allows for the dynamic memory allocation in its programming implementation.

III Applications of 2D-MRTD

The 2D-MRTD scheme is applied to the analysis of the partially-loaded parallel-plate waveguide of (Fig.1) for the frequency range 0-30GHz. For the

analysis based on Yee's FDTD scheme, a 16×800 mesh is used resulting in a total number of 14400 grid points. When the structure is analyzed with the 2D-MRTD scheme, a mesh 2×100 (200 grid points) is chosen ($dx = 0.24\lambda_o$, $dz = 0.4\lambda_o$ for $f = 30GHz$). This size is based on the number of the scaling functions, since the wavelets are used only when and where necessary. The time discretization interval is selected to be identical for both schemes and equal to the 1/10 of the 2D-MRTD maximum Δt. For the analysis we use 8,000 time-steps. The waveguide is excited with a Gabor function 0-30GHz along a vertical line for the FDTD simulation and for a rectangular region for the MRTD simulations. In all cases, the front and back open planes are terminated with a PML region of 16 cells and σ^E_{max}=0.4S/m. The longitudinal distance between the excitation and the dielectric interface is chosen such that no reflections would appear before the Gabor function is complete.

The capability of the MRTD technique to provide space and time adaptive gridding is verified by thresholding the wavelet components to the 0.1% of the value of the scaling function at the same cell for each time-step. It has been observed that the accuracy by using only a small number of wavelets is equal to what would be achieved if wavelets were used everywhere. Though this number is varying in time, its maximum value is 22 out of a total of 100 to the z-direction (economy in memory by a factor of 28-30). In addition, execution time is reduced by a factor 4-5. For larger thresholds, the ringing effect due to the elimination of the wavelets deteriorates the performance of the algorithm. For example, using a threshold of 1% (6 out of a 100 wavelets to the z-direction) increases the error by a factor of 2.5.

The normal electric field is probed at a distance 10 cells away from the source and is plotted in (Fig.2) in time-domain. Comparable accuracy can be observed for the FDTD and the MRTD meshes. In addition, the reflection coefficient S_{11} is calculated by separating the incident and the reflected part of the probed field and taking the Fourier transform of their ratio (Fig.3). The results for 5 GHz (TEM propagation) are validated by comparison to the theoretical value obtained applying ideal transmission line theory [?] and are plotted at Table 2. The time- and space-adaptive character of the gridding is exploited in (Figs.4,5) which show that the wavelets follow the propagating pulses before and after the incidence to the dielectric interfaces and have negligible values elsewhere. The location and the number of the wavelet coefficients with significant values are different for each time-step, something that creates a dense mesh in regions of strong field variations, while maintaining a much coarser mesh for the other cells.

IV Conclusion

A space- and time- adaptive gridding algorithm based on a multiresolution time-domain scheme in two dimensions has been proposed and has been applied to the numerical analysis of a waveguide problem. The field pattern and the reflection coefficient have been calculated and verified by comparison to reference data. In comparison to Yee's conventional FDTD scheme, the proposed scheme offers memory savings by a factor of 5-6 per dimension maintaining a similar accuracy. The above algorithm can be effectively extended to three-dimension problems.

V Acknowledgments

This work has been funded by NSF and ARO.

References

[1] M.Krumpholz, L.P.B.Katehi, "New Prospects for Time Domain Analysis", IEEE Microwave and Guided Wave Letters, pp. 382-384, November 1995.

[2] M.Krumpholz, L.P.B.Katehi, "MRTD: New Time Domain Schemes Based on Multiresolution Analysis", IEEE Transactions on Microwave Theory and Techniques, pp. 555-572, April 1996.

[3] E.Tentzeris, M.Krumpholz and L.P.B. Katehi, "Application of MRTD to Printed Transmission Lines", Proc. MTT-S 1996, pp. 573-576.

[4] E.Tentzeris, R.Robertson, M.Krumpholz and L.P.B. Katehi, "Application of the PML Absorber to the MRTD Technique", Proc. AP-S 1996, pp. 634-637.

[5] I.Daubechies, "Ten Lectures on Wavelets", Philadelphia, PA: Society for Ind. and App. Math., 1992.

[6] D.M.Pozar, "Microwave Engineering", pp. 94-96, Addison-Wesley, 1990.

Table 1: Excitation Decomposition Coeffs

i	0	1	2	3	4
$c_e(i)$	0.915	0.038	0.010	-0.009	0.005
$c_t(i)$	-0.103	-0.103	0.121	-0.030	0.015

Table 2: S_{11} calculated by 2D-MRTD

	S_{11} (Ω)	Relative error
Analyt. Value [?]	0.4298	0.0%
16x800 FDTD	0.4283	-0.3%
2x100 MRTD	0.4360	+1.4%

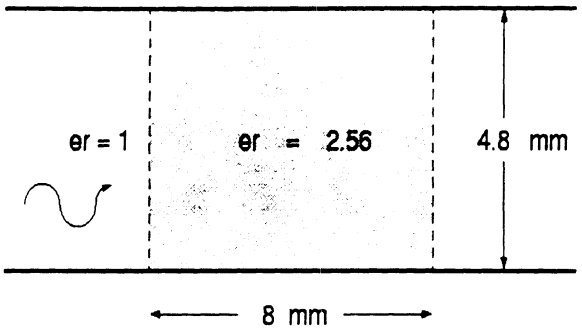

Figure 1: Dielectric-loaded Waveguide.

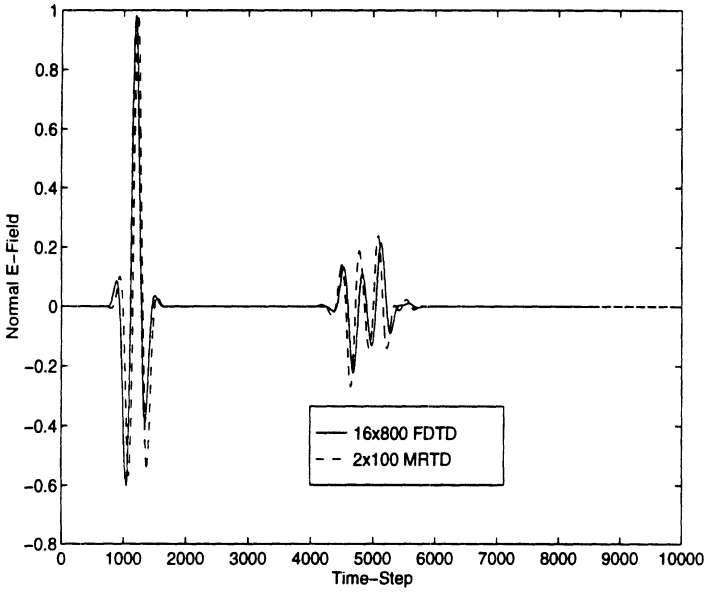

Figure 2: Normal E-field (Time-Domain).

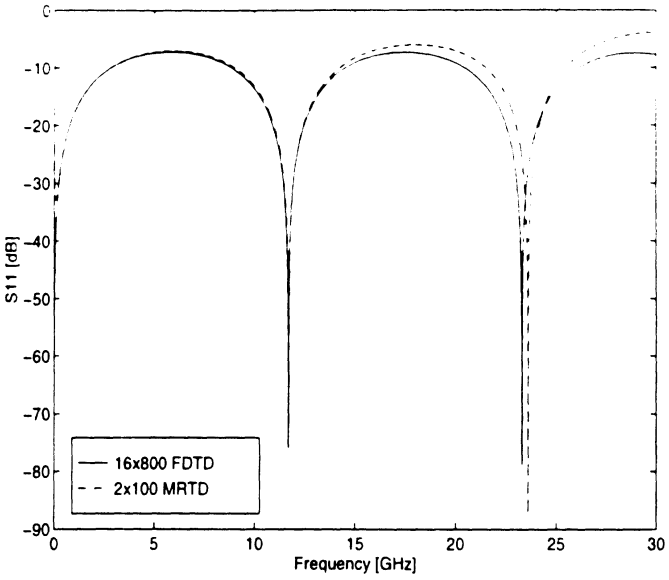

Figure 3: S_{11} values (Frequency-Domain).

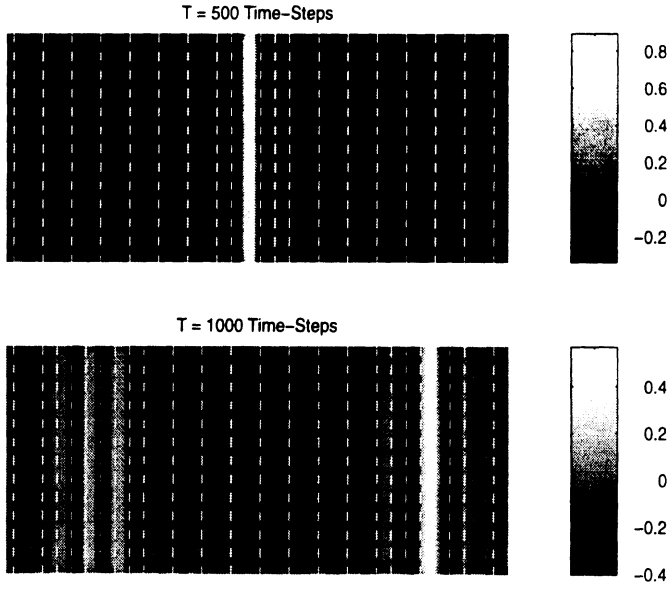

Figure 4: Adaptive Grid Demonstration.

Invited Paper for the Session Organized by Professor Petropoulos

PML Implementation for the Battle-Lemarie Multiresolution Time–Domain Schemes

Emmanouil Tentzeris, Rob Robertson, Linda P.B. Katehi
Radiation Laboratory, EECS Department, University of Michigan,
Ann Arbor, MI 48109-2122, USA

I Introduction

The Multiresolution Time Domain (MRTD) Technique based on cubic-spline Battle Lemarie scaling and wavelet functions has shown successful application to a variety of microwave problems and has demonstrated unparalleled properties in terms of memory and execution time by one and two orders of magnitude respectively. This technique is used to model open and shielded propagation problems [1, 3] and non-linear optical applications [2]. In addition to time and memory, the most important advantage of this new technique is its capability to provide space and time adaptive meshing without the problems encountered by the conventional Finite Difference Time Domain(FDTD) [4] method. In this paper, an efficient non-split formulation of the PML absorber [5] for the Battle-Lemarie based MRTD scheme is presented. This formulation is validated and applied in the analysis of a two–dimensional parallel–plate waveguide geometry offering a numerical coefficient of reflection below -90dB. Additionally, examples for a three–dimensional patch antenna geometry are given.

II Derivation of the MRTD equations for the PML layer

Without loss of generality, the PML Absorber equations will be presented for a homogeneous medium for TM propagation in 2D. The Absorber formulation for TE propagation is straightforward. Assuming that the PML area is characterized by (ϵ_o, μ_o) and electric and magnetic conductivities (σ_E, σ_H), the TM equations can be written

$$\epsilon_o \frac{\partial E_x}{\partial t} + \sigma_E E_x = -\frac{\partial H_y}{\partial z} \tag{1}$$

$$\epsilon_o \frac{\partial E_z}{\partial t} + \sigma_E E_z = \frac{\partial H_y}{\partial x} \tag{2}$$

$$\mu_o \frac{\partial H_y}{\partial t} + \sigma_H H_y = \frac{\partial E_z}{\partial x} - \frac{\partial E_x}{\partial z} \quad . \tag{3}$$

PML cells only to the z-direction are considered. Equations for PML cells in the x- and y-directions can be derived in a similar way. For each point z of the PML area, the magnetic conductivity σ^H needs to be chosen as [5]:

$$\frac{\sigma_E(z)}{\epsilon_o} = \frac{\sigma_H(z)}{\mu_o} \tag{4}$$

for a perfect absorption of the outgoing waves. A parabolic spatial distribution of $\sigma_{E,H}$,

$$\sigma_{E,H}(z) = \sigma_{E,H}^{max}(1 - \frac{z}{\delta})^p \quad \text{, with p=2} \qquad \text{for } 0 \leq z \leq \delta = \text{PML thickness} \tag{5}$$

is used in the simulations, though higher order distributions (e.g.Cubic p=3) can give similar results. The PML area is terminated with a PEC and usually has a thickness varying between 4-16 cells. The maximum value σ_E^{max} is determined by the designated reflection coefficient R at normal incidence, which is given by the relationship

$$R = e^{-\frac{2}{\epsilon_o c}\int_o^\delta \sigma_E(z)dz} = e^{-\frac{2\sigma_E^{max}\delta}{\epsilon_o c(p+1)}} \quad . \tag{6}$$

The electric and magnetic field components incorporated in these equations are expanded in a series of Battle-Lemarie scaling and wavelet functions in both x- and z-directions. For example, E_x can be represented as:

$$\begin{aligned} E_x(x,z,t) &= \sum_{k,l,m=-\infty}^{+\infty} {}_kE_{l+1/2,m}^{x,\phi\phi} h_k(t)\phi_{l+1/2}(x)\phi_m(z) \\ &+ \sum_i \sum_{k,l,m=-\infty}^{+\infty} {}_kE_{l+1/2,m}^{x,\phi\psi_i} h_k(t)\,\phi_{l+1/2}(x)\,\psi_{i,m}(z) \\ &+ \sum_i \sum_{k,l,m=-\infty}^{+\infty} {}_kE_{l+1/2,m}^{x,\psi_i\phi} h_k(t)\,\psi_{i,l+1/2}(x)\,\phi_m(z) \\ &+ \sum_{i,j} \sum_{k,l,m=-\infty}^{+\infty} {}_kE_{l+1/2,m}^{x,\psi_i\psi_j} h_k(t)\,\psi_{i,l+1/2}(x)\,\psi_{j,m}(z) \end{aligned} \tag{7}$$

where $\phi_m(x) = \phi(\frac{x}{\Delta x} - m)$ and $\psi_{i,m}(x) = \psi_i(\frac{x}{\Delta x} - m)$ represent the Battle-Lemarie scaling and i-th order resolution wavelet function respectively in space and $h_k(t)$ represent rectangular pulses in time. ${}_kE_{l,m}^{\kappa,\mu\nu}$ and ${}_{k+1/2}H_{l,m}^{\kappa,\mu\nu}$ with $\kappa = x,y,z$ and $\mu,\nu = \phi,\psi$ are the coefficients for the field expansions in terms of scaling and wavelet functions. The indices l,m and k are the discrete space and time indices related to the space and time coordinates via $x = l\Delta x$,$z = m\Delta z$ and $t = k\Delta t$, where Δx,Δz are the space discretization intervals in x- and z-direction and Δt is the time discretization interval. For an accuracy of 0.1% the above summations are truncated to 16-24 terms. For simplicity, expansion only in scaling functions will be considered. Wavelets are implemented in a similar way. Upon inserting the field expansions, Maxwell's equations

are sampled [3] using pulse functions as time-domain test functions and scaling functions as space-domain test-functions and the following non-split formulation of the fields for the PML region is derived:

$$
\begin{aligned}
{}_{k+1}E^{x,\phi\phi}_{l+1/2,m} &= e^{-\sigma_E^m \Delta t/\epsilon_o}\, {}_kE^{x,\phi\phi}_{l+1/2,m} \\
&- e^{-0.5\sigma_E^m \Delta t/\epsilon_o}\Big(\frac{1}{\Delta z}\sum_{i'=m-9}^{m+8} a(i')_{k+1/2} H^{y,\phi\phi}_{l+1/2,i'+1/2}\Big) \\
{}_{k+1}E^{z,\phi\phi}_{l,m+1/2} &= e^{-\sigma_E^{m+1/2} \Delta t/\epsilon_o}\, {}_kE^{z,\phi\phi}_{l,m+1/2} \\
&+ e^{-0.5\sigma_E^{m+1/2} \Delta t/\epsilon_o}\Big(\frac{1}{\Delta x}\sum_{i'=l-9}^{l+8} a(i')_{k+1/2} H^{y,\phi\phi}_{i'+1/2,m+1/2}\Big) \\
{}_{k+1/2}H^{y,\phi\phi}_{l+1/2,m+1/2} &= e^{-\sigma_H^m \Delta t/\mu_o}\, {}_{k-1/2}H^{y,\phi\phi}_{l+1/2,m+1/2} \\
&+ e^{-0.5\sigma_H^m \Delta t/\mu_o}\Big(\frac{1}{\Delta x}\sum_{i'=l-9}^{l+8} a(i')_k E^{z,\phi\phi}_{i',m+1/2} - \frac{1}{\Delta z}\sum_{i'=m-9}^{m+8} a(i')_k E^{x,\phi\phi}_{l,i'}\Big) \qquad (8)
\end{aligned}
$$

where the terms $\sigma^m_{E,H}$ are given by Eq.(12).

A parallel-plate waveguide of width d=48 mm, terminated at both ends by PML, is used to validate the proposed algorithm. A TM source with a Gabor time variation is excited close to one side of the waveguide. The benchmark MRTD solution with no reflections is obtained by simulating the case of a much longer parallel-plate waveguide of the same width to provide a reflection-free observation area for the time interval of interest. A quadratic variation in PML conductivity is assumed for all cases, with maximum theoretical reflection coefficient of 10^{-5} at normal incidence. Numerical reflection is observed for the frequency range $[0, 0.9 f_c^{TM_1}]$ (TEM propagation) where $f_c^{TM_1} = \frac{c}{2d} = 3.125\ (GHz)$ is the cutoff frequency of the TM_1 mode. It can be seen from Figs.(1)-(2) that for 8 PML cells and σ_E^{max}=0.4 S/m it is S_{11} $\leq$-65 dB and for 16 PML cells and σ_E^{max}=0.2 S/m the reflection is smaller than -91 dB. Thus, the non-split PML absorber can be used effectively in the simulation of antennas and active elements using MRTD.

III Application of PML to the Analysis of Antenna Geometries

MRTD can successfully model both planar circuits [6] and resonating structures [7]. Recently the techniques developed for the simulation of both structures are combined to model a three-dimensional patch antenna geometry [8]. Full three–dimensional MRTD analysis is used, with PML expanded through three coordinate directions. The procedure to derive an equation for the

	Δt	PML cells along z	σ_{max}^{Ex}	σ_{max}^{Ey}	σ_{max}^{Ez}
FDTD ($60 \times 100 \times 16$)	$1.3297 \cdot 10^{-13}s$	6	3.0	3.0	3.0
MRTD($30 \times 50 \times 9$)	$1.6008 \cdot 10^{-13}s$	2-6	3.0	3.0	11.53
MRTD ($20 \times 20 \times 9$)	$1.3297 \cdot 10^{-13}s$	6-10	3.0	3.0	11.53

Table 1: Computational Parameters.

three-dimensional MRTD scheme, with PML along all three coordinate directions is presented in [8].

The patch antenna used in our simulations has the dimensions $12.45mm \times 16mm$, with a microstrip line 20 mm long used as a feed. A Gaussian pulse 4 mm from the PML layer is used to excite the microstrip. The substrate has a thickness of 0.794 mm and a relative dielectric constant equal to 1. An FDTD mesh of $60 \times 100 \times 16$ is compared to MRTD grids of $30 \times 50 \times 9$ and $20 \times 20 \times 9$, which exhibit savings of memory over FDTD on the order of 7.22 and 33 respectively. Note that these values do not include the PML layers. Figure 3 shows a comparison plot of calculated S_{11} data for the three cases listed above. Six cells of PML are added along the $\pm x$, $\pm y$ and $+z$ directions with $\sigma_{max}^{Ex} = \sigma_{max}^{Ey} = 3.0$ and $\sigma_{max}^{Ez} = 11.53$ for all cases. The time discretization interval used for the MRTD $30 \times 50 \times 9$ scheme is $\Delta t = 1.6008 \cdot 10^{-13}s$ while the MRTD $20 \times 20 \times 9$ scheme uses a time discretization interval of $\Delta t = 1.42384 \cdot 10^{-13}s$. FDTD uses a time discretization interval of $\Delta t = 1.3297 \cdot 10^{-13}s$. In all three cases the simulation is performed for 10000 time steps. This information is summarized in Table 1.

Figure 4 shows a comparison of S_{11} data for different numbers of z–directed PML layers for an MRTD discretization of $30 \times 50 \times 9$. Note that the S_{11} values correlate very well even for only 2 PML layers in the z–direction. Figure 4 shows a comparison of S_{11} data for different numbers of z–directed PML layers for an MRTD discretization of $20 \times 20 \times 9$. Once again the values of S_{11} show good correlation.

IV Conclusion

An efficient PML absorber in non-split formulation is presented for the MRTD Scheme based on cubic spline Battle-Lemarie scaling functions. This absorber is used effectively to model an antenna geometry providing extremely small numerical reflections. In comparison to Yee's conventional FDTD scheme, the proposed MRTD scheme coupled with the PML absorber offer memory savings by a factor of 12-30 and execution time savings by a factor of about 3-5 maintaining a better accuracy for S-parameter calculations. For structures where the edge effect is prominent, additional wavelets can be used to improve the accuracy when using a

coarse MRTD mesh.

V Acknowledgments

This work was made possible by ONR contract N00014-95-1-1299 and ARO contract DAAH04-95-1-0321.

References

[1] M.Krumpholz, L.P.B.Katehi, "MRTD: New Time Domain Schemes Based on Multiresolution Analysis", *IEEE Trans. Microwave Theory and Techniques*, vol. 44, no. 4, pp. 555-561, April 1996.

[2] M.Krumpholz, L.P.B.Katehi, "MRTD Modeling of Nonlinear Pulse Propagation", to be published at the *IEEE Trans. Microwave Theory and Techniques.*

[3] E.M.Tentzeris, R.Robertson, M.Krumpholz, L.P.B.Katehi, "Application of the PML Absorber to the MRTD Technique", *Proc. AP-S 1996*, pp. 634-637.

[4] K.S.Yee, "Numerical solution of initial boundary value problems involving Maxwell's equations in isotropic media", *IEEE Trans. Antennas Propagation*, pp.302-307, May 1966.

[5] J.-P. Berenger, "A Perfectly Matched Layer for the Absorption of Electromagnetic Waves", *J.Comput. Physics*, vol. 114, pp. 185-200, 1994.

[6] E. Tentzeris, M. Krumpholz and L.P.B. Katehi, "Application of MRTD to Printed Transmission Lines", *Proc. MTT-S 1996*, pp. 573-576.

[7] R. Robertson, E. Tentzeris, M. Krumpholz and L.P.B. Katehi, "Application of MRTD Analysis to Dielectric Cavity Structures",*Proc. MTT-S 1996*, pp. 1840-1843.

[8] R. Robertson, E. Tentzeris, and L.P.B. Katehi, "Modeling of Membrane Patch Antennas using MRTD Analysis", *Proc. AP-S 1997*, pp. 126-129.

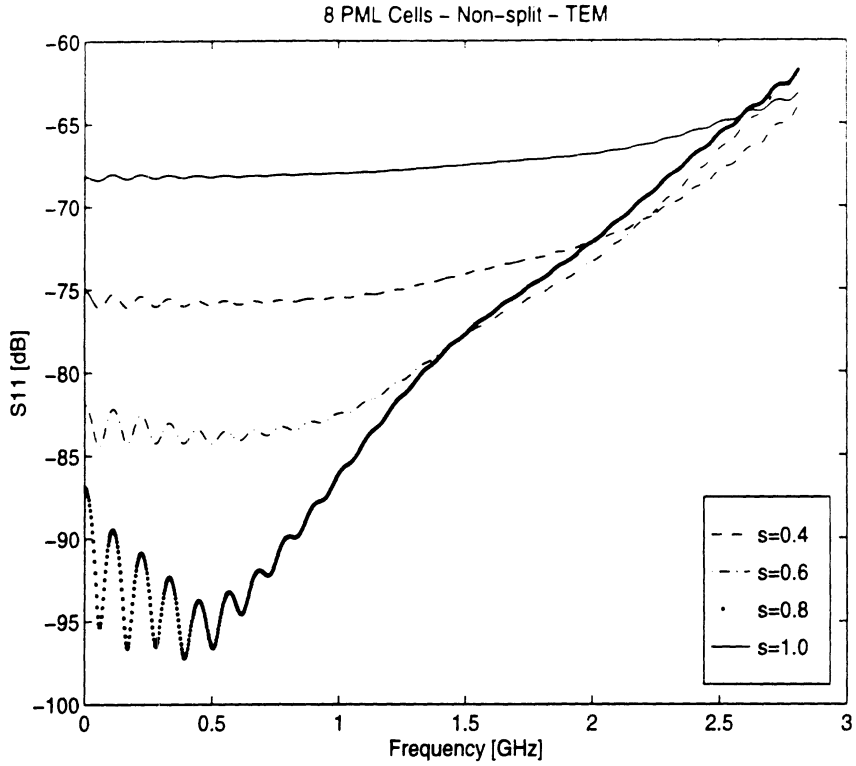

Figure 1: 8 PML cells.

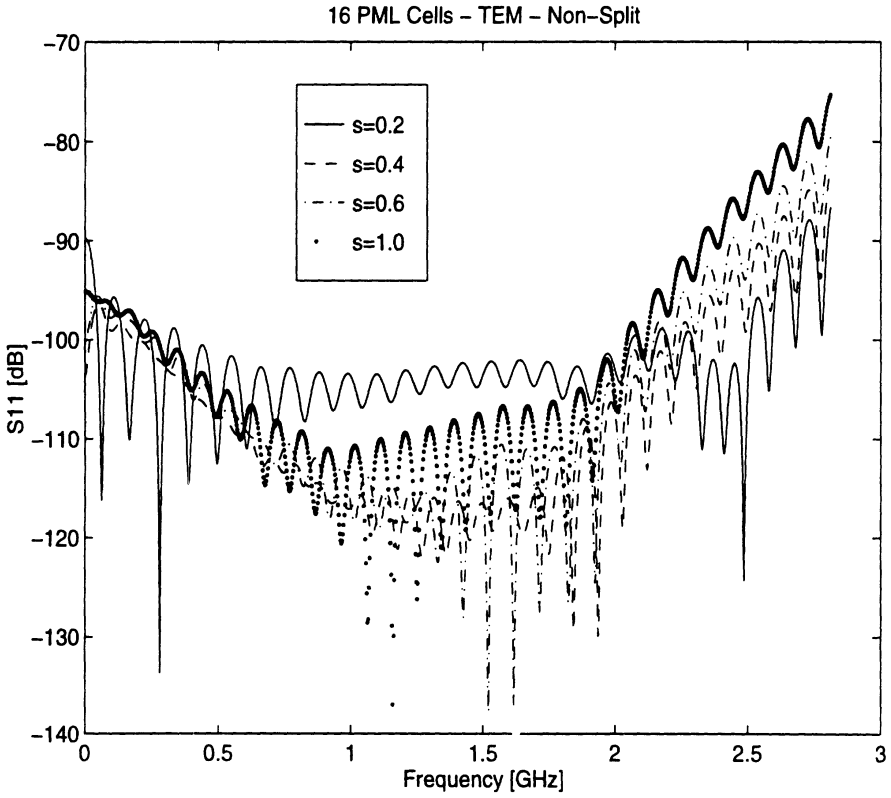

Figure 2: 16 PML cells.

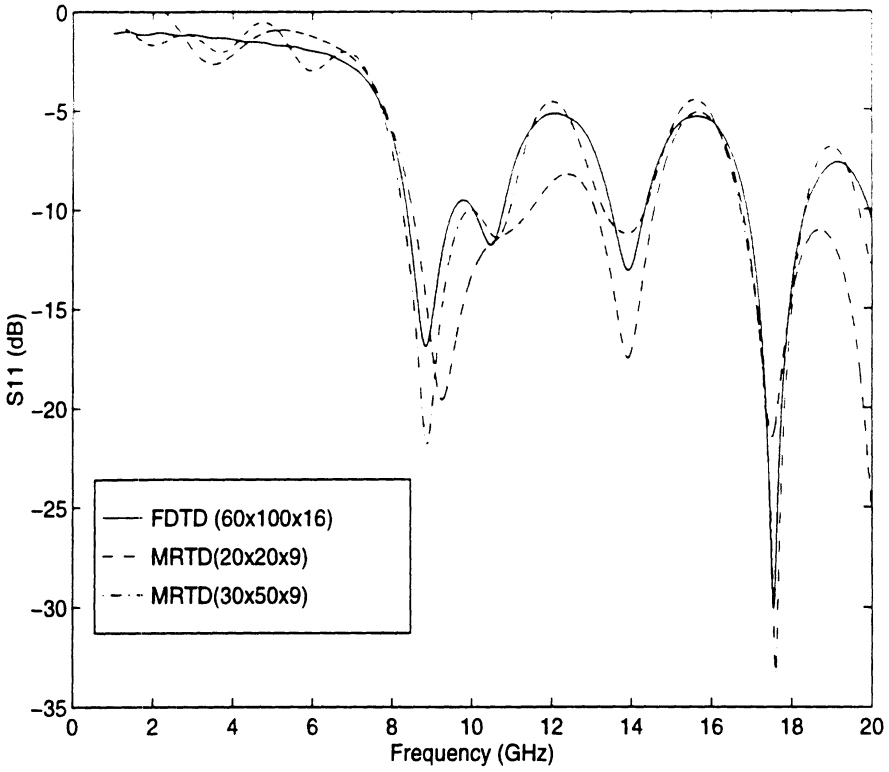

Figure 3: S_{11} comparison plots for a patch antenna

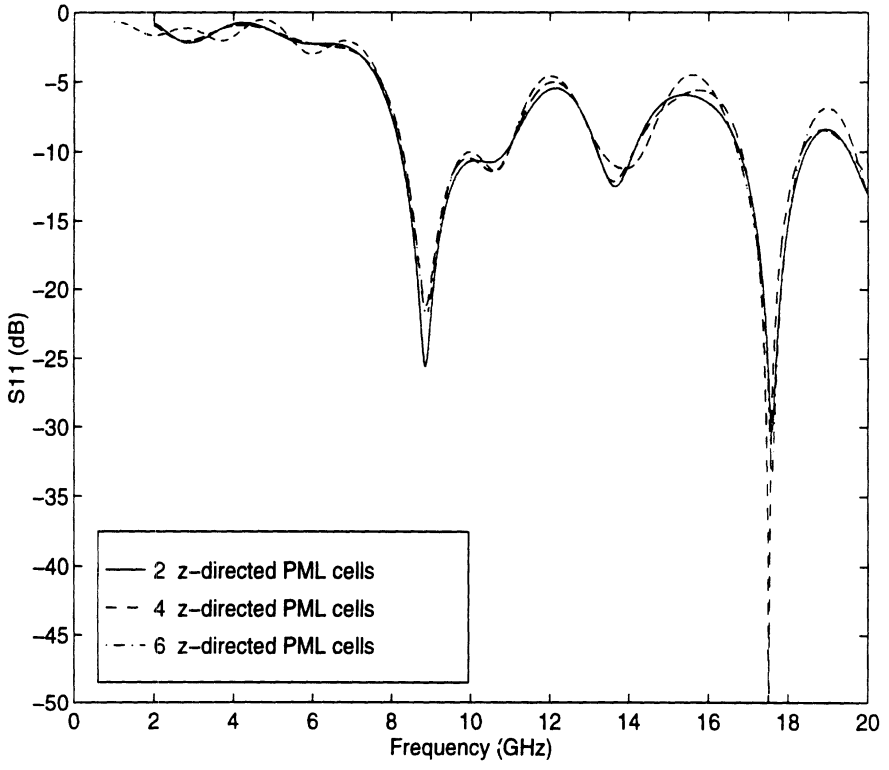

Figure 4: MRTD($30 \times 50 \times 9$) S_{11} plot for varying PML layers in the z–direction

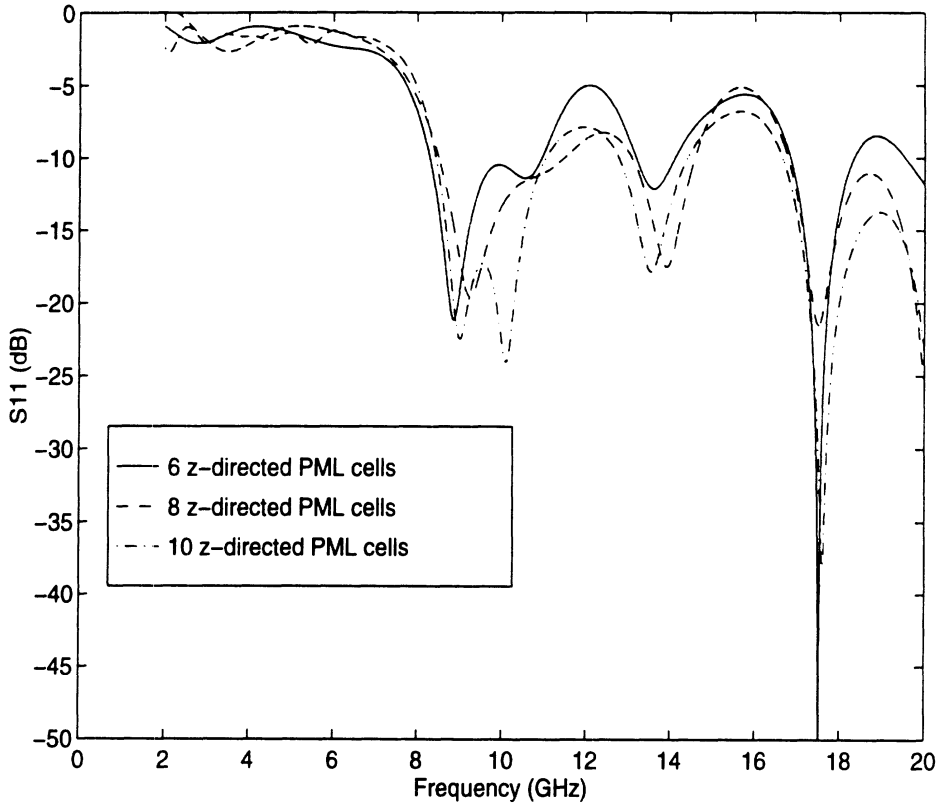

Figure 5: MRTD($20 \times 20 \times 9$) S_{11} plot for varying PML layers in the z–direction